INVESTIGATIONS IN BLUE PHOSPHOR MATERIALS FOR USE IN FULL COLOR THIN FILM ELECTROLUMINESCENT DISPLAYS

John Gavin Ferguson
B.S., McGill University, 1991
M.S. University of Massachusetts, 1993

A thesis submitted to the faculty of the
Oregon Graduate Institute of Science and Technology
in partial fulfillment of the
requirements for the degree
Doctor of Philosophy
in
Electrical Engineering

January 2000

The dissertation "Investigations in Blue Phosphor Materials for Use in Full Color Thin Film Electroluminescent Displays" by John Ferguson has been examined and approved by the following examination committee:

Raj Solanki, Dissertation Adviser
Associate Professor

Reinhart Engelmann
Adjunct Professor

Anthony E. Bell
Associate Professor

Dr. Sey-Shing Sun
Planar America, Inc.

Dedicated with love to Cheryl, Megan and Lindsey.

Sincerest gratitude is extended to Raj Solanki and Reinhart Engelmann as well as the other members of the dissertation committee for their patience, insight and guidance during the course of this work. I'd also like to recognize DARPA for providing the necessary funding for the research presented. I'd also like to thank Richard Teunge, Sey-Shing Sun and Stephanie Moehnke of Planar America, Inc. for supplying materials, analysis, and guidance in this endeavor. I'd also like to thank many of my colleagues who have provided insights contained in this work, including Weiran Kong, John Fogarty, Shafqat Ahmed, Chris Barbero, Cangsang Zhao, Yijun Cai, Srikanth Ranjarajan, and Aaron Marmorstein. I'd also like to extend my thanks to Alison Roache and Julianne Williams of the Oregon Graduate Institute. Finally, I'd like to thank my wife and children, my parents, Duncan and Gail Ferguson, and Buck and Laurie Armstrong for their support.

TABLE OF CONTENTS

DEDICATION iii
ACKNOWLEDGEMENTS iv
LIST OF TABLES vii
LIST OF FIGURES viii
LIST OF ACRONYMS xi
LIST OF SYMBOLS xii
ABSTRACT xiv

1 INTRODUCTION 1
- 1.1 COLOR TFEL DISPLAYS 3
- 1.2 RED PHOSPHOR MATERIALS 5
- 1.3 GREEN PHOSPHOR MATERIALS 5
- 1.4 BLUE PHOSPHOR MATERIALS 6
- 1.5 WHITE PHOSPHOR MATERIALS 7
- 1.6 THESIS OBJECTIVES 7

2 ATOMIC LAYER EPITAXY 9
- 2.1 HISTORY 9
- 2.2 ALE OPERATING MECHANISMS 10
- 2.3 MODIFIED F-120 REACTOR WITH SATELLITE CONFIGURATION 14
- 2.4 CHARACTERIZATION OF FILM GROWTH 21

3 ELECTROLUMINESCENT DISPLAYS 22
- 3.1 HISTORY OF ELECTROLUMINESCENCE 22
- 3.2 ACTFEL DEVICE STRUCTURE 23
- 3.3 DEVICE PHYSICS 26
  - 3.3.1 CARRIER INJECTION 27
  - 3.3.2 ELECTRON IMPACT AND EXCITATION MECHANISMS 27
  - 3.3.3 EXCITATION FROM RARE EARTH ACTIVATORS 29
  - 3.3.4 RECOMBINATION AND EFFECTS OF SPACE CHARGE 30
- 3.4 ACTFEL DEVICE CHARACTERISTICS 32

4 BLUE EMISSION FROM SrS HOSTS 33
- 4.1 SrS:Ce PHOSPHORS 34
  - 4.1.1 BRIGHTNESS VS. THICKNESS MEASUREMENTS 35
  - 4.1.2 EFFECTS OF DRIVE FREQUENCY AND WAVEFORM ON EMISSION PROPERTIES 37
- 4.2 CODOPING IN SrS:Ce 47
  - 4.2.1 SrS:Ce WITH NITROGEN AND BISMUTH CODOPING 48
  - 4.2.2 SrS:Ce WITH OXYGEN CODOPING 58

4.2.3 SrS:Ce WITH SINGLE LAYER ZnS INCORPORATION.....60
4.3 BLUE EMISSION FROM OTHER ACTIVATORS IN SrS HOSTS.....62
4.4 TFEL EMISSION FROM $SrCl_2$ FORMED IN ZnS/SrS STACK.....66
4.5 CONCLUSION.....69

5 QUANTUM WELL ACTIVATED PHOSPHORS.....71
5.1 THEORY OF MQW DEVICE EMISSION.....72
5.2 MODELING OF EMISSION FROM DEEP MQW.....73

6 EMISSION FROM MULTI-QUANTUM WELL DEVICES.....79
6.1 CdSe WELLS IN AN SrS HOSTS.....80
6.1.1 GROWTH OF SrS/CdSe MQW DEVICES.....81
6.1.2 OBSERVED EMISSION FROM SrS/CdSe MQW DEVICES.....84
6.1.3 COMPARISON TO MODEL.....90
6.2 ZnSe WELLS IN CaS HOSTS.....97
6.2.1 GROWTH OF CaS/ZnSe MQW DEVICES.....98
6.2.2 EMISSION FROM CaS/ZnSe AND COMPARISON TO MODEL.....101
6.3 SUMMARY.....103

7 CONCLUSIONS AND FUTURE.....104

A SrS GROWTH VIA ALE.....108
A.1 OPTICAL PERFORMANCE.....111

B LOW TEMPERATURE GROWTH OF ZnS:Mn PHOSPHORS FROM DIKETONATE PRECURSOR.....115
B.1 ALE GROWTH OF ZnS FROM $Zn(thd)_2$.....116
B.2 EL EMISSION.....119

C TFEL OXIDE LAYER GROWTH BY ATOMIC LAYER EPITAXY.....121
C.1 ALE GROWTH OF Al_2O_3.....122
C.1.1 Al_2O_3 GROWTH FROM ALUMINUM ISOPROPOXIDE.....123
C.1.2 Al_2O_3 GROWTH FROM $Al(C_2H_5)$ AND $Al(CH_3)_3$ WITH WATER.....127
C.1.3 ATTEMPTED Al_2O_3 GROWTH FROM $Al(thd)_2$ AND H_2O....129
C.2 ALE GROWTH OF Ta_2O_5.....129

D MATLAB PROGRAM FOR DETERMINING MQW EMISSION.....131

REFERENCES.....143

LIST OF TABLES

6.1 OBSERVED AND PREDICTED EMISSION FOR THE 15 nm DEVICE WITH VARYING APPLIED FREQUENCY AT 250 V. 93
6.2 OBSERVED AND PREDICTED EMISSION FOR THE 15 nm DEVICE WITH VARYING APPLIED VOLTAGE AT 1 kHz. 94
6.3 OBSERVED AND PREDICTED EMISSION FROM SrS/CdSe MQW DEVICES AT 1 kHz and 200 V. 95
6.4 OBSERVED AND PREDICTED EMISSION FROM THE 8 nm CaS/ZnSe MQW DEVICE. 102

A.1 CHARACTERISTICS OF SrS FILMS GROWN VIA ALE FROM $Sr(thd)_2$ FROM VARYING SOURCES. 110
A.2 OPTICAL CHARACTERISTICS OF SrS:Ce GROWN VIA ALE WITH VARYING $Sr(thd)_2$ SOURCES. 113

B.1 GROWTH RATE AND UNIFORMITY OF ZnS:Mn DEVICES AT VARIOUS DOPING LEVELS. 118

C.1 PROPERTIES OF Al_2O_3 GROWN FROM VARIOUS PRECURSOR MATERIALS. 123
C.2 Al_2O_3 FILM CHARACTERISTICS WITH ANNEAL. 126
C.3 GROWTH RATE OF Ta_2O_5 FROM $Ta(OC_2H_5)_5$ AT VARYING TEMPERATURE. 130

LIST OF FIGURES

1.1 CIE POSITION OF COMMON TFEL PHOSPHOR MATERIALS. 4

2.1 CHEMICAL ADSORPTION VS. PHYSICAL ADSORPTION. 11
2.2 "DIGITAL EPITAXY" PULSING IN ALE TECHNIQUE 11
2.3 ALE PROCESS TEMPERATURE WINDOW 13
2.4 OLD F-120 SUBSTRATE HOLDER 15
2.5 NEW F-120 SUBSTRATE HOLDER (SATELLITE CONFIGURATION) REAR VIEW 16
2.6 NEW F-120 SUBSTRATE HOLDER (SATELLITE CONFIGURATION) SIDE VIEW. 17

3.1 ACTFEL DEVICE STRUCTURE. 24
3.2 ACTFEL BAND MODEL. 26
3.3 TYPICAL BRIGHTNESS VS. VOLTAGE CHARACTERISTICS FOR ACTFEL PHOSPHORS. 32

4.1 BRIGHTNESS VS. VOLTAGE FOR SrS:Ce WITH VARYING DOPING LEVELS. 35
4.2 BRIGHTNESS VS. VOLTAGE FOR SrS:Ce WITH VARYING PHOSPHOR THICKNESS. 36
4.3 DRIVING VOLTAGE WAVEFORMS. 38
4.4 BRIGHTNESS VS. FREQUENCY FOR SrS:Ce DEVICES WITH BIPOLAR, SAWTOOTH AND SINEWAVE DRIVING WAVEFORMS AT 200 HZ. 39
4.5 BRIGHTNESS VS. VOLTAGE FOR SrS:Ce AT 60 Hz FOR BIPOLAR AND SINE WAVEFORMS AT 200 HZ. 39
4.6 BRIGHTNESS VS. FREQUENCY FOR ZnS:Mn DOPED 1:40 WITH BIPOLAR SAWTOOTH AND SINE WAVE DRIVING WAVEFORMS. 40
4.7 MAXIMUM CURRENT VS. FREQUENCY FOR SrS:Ce WITH DOPING LEVELS OF 1:80 AT 200 V FOR THE SINE AND BIPOLAR DRIVING WAVEFORM 42
4.8 MAXIMUM CURRENT VS. FREQUENCY FOR 2 nF CAPACITOR AT 200 V WITH THE BIPOLAR WAVEFORM 43
4.9 BRIGHTNESS VS. FREQUENCY FOR ZnS:Mn DOPED 1:40 AT 200 V WITH THE BIPOLAR WAVEFORM AT 25°C. 44
4.10 BRIGHTNESS VS. FREQUENCY FOR ZnS:Mn WITH VARYING DOPING LEVELS. 46

4.11 EMISSION OF SrS:Ce WITH VARYING CONCENTRATIONS OF N CODOPING. 50
4.12 BRIGHTNESS VS. VOLTAGE FOR SrS:Ce WITH VARYING CONCENTRATIONS OF N CODOPING. 50
4.13 CIE COORDINATES FOR SrS:Ce WITH VARYING CONCENTRATIONS OF N CODOPING. 51
4.14 X-RAY DIFFRACTION FROM (a) SrS:CeS (b) SrS:3N,CeS,3N WITHOUT RTA AND (c) SrS:3N,CeS,3N WITH RTA. 53
4.15 EMISSION SPECTRA OF SrS:3N,CeS,3N WITH AND WITHOUT RTA. 54
4.16 BRIGHTNESS VS. VOLTAGE FOR SrS:3N,CeS,3N DEVICES WITH AND WITHOUT RTA. 55
4.17 CIE COORDINATES FOR SrS:3N,CeS,3N DEVICES WITH AND WITHOUT RTA. 55
4.18 EMISSION SPECTRA FROM SrS:Ce CODOPED WITH Bi. 57
4.19 BRIGHTNESS VS. VOLTAGE FOR SrS:Ce WITH Bi CODOPING. 57
4.20 CIE COORDINATES FOR SrS:Ce WITH Bi CODOPING. 58
4.21 BRIGHTNESS VS. VOLTAGE FOR SrS:Ce WITH AND WITHOUT O CODOPING. 59
4.22 EMISSION OF SrS:Ce WITH SINGLE LAYER ZnS CODOPING. 61
4.23 CIE LOCATION OF SrS:Ce WITH SINGLE LAYER ZnS CODOPING. 61
4.24 EMISSION SPECTRA FROM ZnS:Te AND SrS:Te FROM TeCl PRECURSOR. 62
4.25 EMISSION FROM SrS:Te FROM ELEMENTAL Te PRECURSOR. 63
4.26 CIE LOCATION OF SrS:Te EL EMISSION. 65
4.27 BRIGHTNESS VS. VOLTAGE FOR SrS:Te FROM ELEMENTAL Te COMPARED WITH SrS:Ce. 65
4.28 EMISSION FROM STANDARD SrS TFEL PHOSPHORS WITH VARIOUS ACTIVATORS. 67
4.29 EMISSION FROM SrS WITH ZnS STACKING LAYERS WITH VARIOUS ACTIVATORS. 68

5.1 MQW DEVICE BAND MODEL. 72

6.1 BAND OFFSET OF CdSe WELLS IN SrS HOST. 80
6.2 X-RAY DIFFRACTION OF CdSe FILM GROWN ON a) BARE GLASS AND b) SrS SUBSTRATES. 82
6.3 X-RAY DIFFRACTION OF SrS/CdSe MQW DEVICE WITH 8 nm THICK WELLS. 83
6.4 EMISSION SPECTRA OF THE 10 nm AND 3 nm SrS/CdSe MQW DEVICES AT 500 Hz. 85
6.5 EMISSION SPECTRA FROM 15 nm DEVICE AT 500 Hz AND VARYING APPLIED VOLTAGE. 86

6.6 INTENSITY VS. VOLTAGE FOR THE 5 nm SrS/CdSe MQW DEVICE AT 60 Hz. 87
6.7 EMISSION SPECTRA OF THE 3 nm CdSe/SrS MQW DEVICE AT 500 AND 200 Hz. 88
6.8 CURRENT AND OPTICAL RESPONSE OF 1 nm SrS/CdSe MQW DEVICE TO A SINGLE APPLIED VOLTAGE PULSE. 89
6.9 BAND STRUCTURE OF SrS. 90
6.10 PHOTOLUMINESCENCE OF THE 8 nm SrS/CdSe MQW DEVICE. 96
6.11 BAND STRUCTURE OF THE CaS/ZnSe MQW DEVICES. 97
6.12 X-RAY DIFFRACTION OF CaS ON BARE GLASS. 98
6.13 X-RAY DIFFRACTION OF ZnSe ON BARE GLASS. 99
6.14 X-RAY DIFFRACTION OF 5 nm CaS/ZnSe MQW DEVICE. 100
6.15 EMISSION SPECTRA FROM 8 nm CaS/ZnSe STRUCTURE AT 200 V AND 200 Hz. 101

B.1 X-RAY DIFFRACTION SPECTRA FOR ZnS GROWN AT a) 450 °C b) 350 °C c) 300 °C d) 300 °C WITH Mn DOPING 80:1 AND e) 250 °C. 117
B.2 EMISSION SPECTRA OF ZnS:Mn GROWN FROM $Zn(thd)_2$ PRECURSOR. 119
B.3 BRIGHTNESS VS. VOLTAGE FOR ZnS:Mn DEVICES AT VARYING DOPING LEVELS. 120

C.1 GROWTH RATE VS. CYCLES FOR ALUMINUM ISOPROPOXIDE GROWN Al_2O_3 125

LIST OF ACRONYMS

ACTFEL	Alternating Current Thin Film Electroluminescence
AES	Alkaline Earth Sulfide
ALE	Atomic Layer Epitaxy
ATO	Aluminum Titanium Oxide
BTO	Barium Tantalum Oxide
CIE	Commission Internationale de l'Eclairage
CL	Cathodoluminescence
CVD	Chemical Vapor Deposition
EL	Electroluminescence
FED	Field Effect Display
FWHM	Full Width at Half Max
ITO	Indium Titanium Oxide
LED	Light Emitting Diode
MBE	Molecular Beam Epitaxy
MQW	Multi-Quantum Well
PL	Photoluminescence
QW	Quantum Well
RE	Rare Earth
RTA	Rapid Thermal Anneal
TEA	Triethyl Aluminum
TFEL	Thin Film Electroluminescence
TMA	Trimethyl Aluminum
TV	Television
VGA	Video Graphics Accelerator

LIST OF SYMBOLS

E_p	Physical Adsorption Activation Energy (eV)
E_c	Chemical Adsorption Activation Energy (eV)
η	Activation Energy Discrimination Factor for ALE Growth
k	Boltzman's constant = 8.62 x 10^{-5} (eV/K)
T	Temperature (K)
ϕ	Degrees
E_n	Quantum Energy Level in the n^{th} well (Joules)
h	Plank's constant 6.626 x 10^{-34} (Joules-sec)
L	Quantum well width (m)
m_A	Effective mass of particle in the well (kg)
m_B	Effective mass of particle in the host (kg)
V_o	Quantum well depth (Joules)
H	Perturbation term
e	Particle charge 1.60 x 10^{-19} (Coulombs)
V_{tot}	Total field applied to device (V)
V_{top}	Field across the top oxide layer (V)
V_{bot}	Field across bottom oxide layer (V)
V_{phos}	Field across the phosphor layer (V)
C_{top}	Capacitance of the top oxide layer (F)
C_{bot}	Capacitance of the bottom oxide layer (F)
C_{phos}	Capacitance of the phosphor layer (F)
t_{top}	Thickness of the top oxide layer (m)
t_{bot}	Thickness of the bottom oxide layer (m)
t_{phos}	Thickness of the total phosphor layer (m)
ε_{bot}	Dielectric constant of the top oxide layer
ε_{top}	Dielectric constant of the bottom oxide layer
ε_{phos}	Dielectric constant of the phosphor layer
W_h	Band-gap of the host material (Joules)
W_w	Band-gap of the well material (Joules)
V_{oc}	Host - well band off set in the conduction band (Joules)
V_{ov}	Host -well band off set in the valence band (Joules)

m_h	Hole mass
m_{hh}	Heavy hole mass
m_{hl}	Light hole mass
m_e	Electron mass
m_{per}	Electron mass in the perpendicular direction (X - K)
m_{par}	Electron mass in the parallel direction (X - Γ)

ABSTRACT

INVESTIGATIONS IN BLUE PHOSPHOR MATERIALS FOR USE IN FULL COLOR THIN FILM ELECTROLUMINESCENT DISPLAYS

John Gavin Ferguson

Ph.D., Oregon Graduate Institute of Science and Technology
January, 2000

Thesis Advisor: Raj Solanki

Historically, full color thin film electroluminescent displays have been hampered by the poor emission and difficulty of incorporation of the blue phosphor materials. This thesis presents research performed on blue emitting phosphor materials grown. A new class of phosphor was developed based on the emission from trapped electron - hole pairs in a deep quantum well system embedded into a traditional thin film electroluminescent stacking sandwich. Low intensity emission observed from CdSe/SrS and ZnSe/CaS quantum well phosphors presented.

Additionally, investigations into blue emission from traditional thin film electroluminescent devices are presented. The dependency of driving wave form and frequency on the emission from such phosphors is detailed, showing a surprising peak and corresponding decrease in brightness with increasing frequency.

Further, analyses on the effects of codoping in traditional blue emitting SrS:Ce devices, including an observed blue shift in emission spectra, from nitrogen and bismuth

are detailed. Also investigations into the effects on brightness of SrS:Ce devices with such codopants as zinc and oxygen are reported, again showing a shift toward the blue in emission spectra.

Characterization of blue emission from SrS:Te materials, and the emission from various rare earth dopants in $SrCl_2$ host materials (created from SrS with Cl impurities) showing, in some cases, violet and UV emission are also presented.

This thesis will prove that truer blue emission than previously reported in SrS:Ce phosphor devices is achievable. In none of the alternative cases was the phosphor brightness greater than those observed with the standard SrS:Ce, but each showed significant blue shift in emission spectra. It is also shown that in all standard ACTFEL device types, brightness can be greatly enhanced and optimized by proper selection of driving waveform and frequency. This in conjunction with the insights gained from the multi-quantum well devices shows great promise for greater progress in full color ACTFEL displays.

Chapter 1

Introduction

With the current drive towards smaller, light weight, and portable computer and communication products, the flat panel display market has found its way into the spot-light. Through years of research and development, a number of flat panel technologies have evolved. These include Liquid Crystal Displays (LCD), Plasma Displays, Field Emission Displays (FED), and Electroluminescent Displays (EL). Surprisingly, there is, however, currently no one technology which can meet all the needs of the flat panel display market.

Each of the flat panel technologies currently on the market has a number of advantages and disadvantages associated with it. As a result, each flat panel type has developed its own market 'nitch' which can take advantage of a given technology's strengths. Because of the diversity of the flat panel application requirements, these technologies have so far all been able to co-exist in the market.

The Thin Film Electroluminescent Display (TFEL) technology is one of the most promising of the flat panel technologies currently in existence. The first high luminance, long lifetime TV quality AC driven TFEL was demonstrated by Sharp Electronics at the 1978 Consumer Electronics Show in Chicago[1]. A mature technology, EL devices have progressed from small, single color 'yellow-orange' displays, characterized by simplicity of construction, low cost, high luminous efficiency, environmental ruggedness, and aesthetic performance, to large, full color displays (9" full color displays have been produced by Planar International [2]) with a strong hold on the military, medical and instrumentation markets, and growing strengths in the computer and communication fields.

The term electroluminescence, defined as the emission of light from a crystalline or polycrystalline phosphor solely due to the application of an external field [1], in general refers to two mechanisms of light generation. The first, band to band recombination of electron-hole pairs at a p-n junction, is the mechanism by which light emitting diodes (LEDs) operate. The second, light generation from the collision of hot electrons, under the influence of a high electric field, with activator atoms doped in a high band gap semiconductor material, is the process which governs most current EL displays. This thesis will focus only on the latter technology.

High voltage EL display devices can be further divided into two types, powder and thin film. Each of these, in turn, may be classified as either AC or DC driven devices. Powder type EL devices, which consist of activated phosphor powder dispersed in a layer of insulating substance [3], have been studied since their initial report by Destriau in 1936 [4]. DC powder type displays have even produced alpha-numeric displays [5] and devices capable of TV pictures. Unfortunately these are characterized by low brightness. Thin film electroluminescence (TFEL), which consist of a thin, polycrystalline, phosphor film deposited on a transparent substrate, have been able to overcome many of the problems associated with the powder devices. In particular, the AC thin film electroluminescent devices (ACTFEL), made from the thin film phosphor in a 'double insulating sandwich' configuration originally proposed by Inoguchi et. al. [6] possess high luminous intensity and long lifetimes.

The first efficient ACTFEL devices studied by Inoguchi et. al. consisted of a ZnS semiconductor layer doped with Mn activators as the phosphor. Since this time ZnS:Mn has been the most highly investigated EL phosphor material. Emitting a bright yellow orange light with a main spectrum peak around 580 nm with CIE coordinates of x=0.50 and y=0.50 [2], the ZnS:Mn phosphor remains to this day the standard by which all other EL phosphor materials are compared. This bright and efficient phosphor served as the

basis for the original line of monochrome TFEL displays. Since this time there has been a continuous push by manufacturers of ACTFEL displays to produce a full color ACTFEL display.

1.1 Color TFEL Displays

The first simple multicolor displays can be achieved by taking advantage of the broad emission spectra of the ZnS:Mn phosphor. By incorporating red and green filters with the standard ZnS:Mn phosphor [7] a display capable of producing both green and red light can be produced using the same processing equipment needed for simple monochrome displays. Unfortunately the emission of ZnS:Mn does not extend into the blue region of the spectrum. As a result to obtain a full color display new or additional phosphor materials are required.

There are essentially two methods which can be used to create a full color TFEL display [2]. One method is to produce a phosphor which emits a broad white light and combine it with the necessary red, green and blue filters. The second method consists of producing three separate phosphor materials which emit in the red, green and blue ranges of the spectra respectively. A brief discussion of some of the phosphor research done on each of these methods is presented below. A CIE plot of the common TFEL phosphors appears in Fig. 1.1.

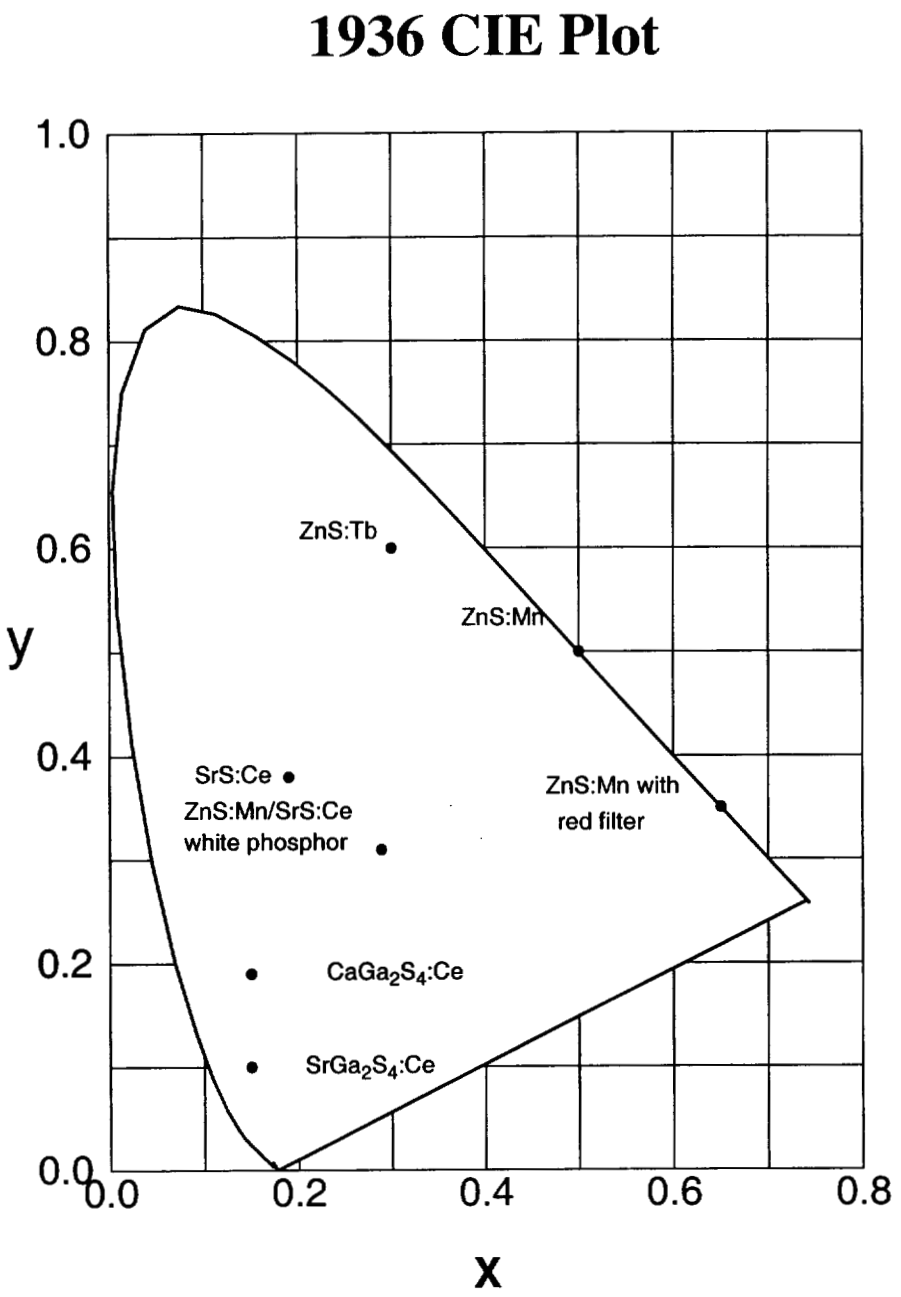

Fig. 1.1 CIE coordinates of common TFEL phosphor materials.

1.2 Red Phosphor Materials

The most commonly used phosphor for red emission is still a filtered ZnS:Mn. This phosphor, under filtering, yields red light with CIE coordinates of x=0.65 and y=0.35 and a luminous efficacy of 1 lm/W [2]. Both SrS:Eu and CaS:Eu, which emits red light with CIE coordinates of x = 0.68 and y = 0.31, have been extensively studied in recent years [8]. Unfortunately low efficiencies (0.2 lm/W) [9] have kept them from achieving the success presently enjoyed by ZnS:Mn. Other red phosphors which have been investigated include: ZnS:SmF_3, ZnS:YbF_3 [10], $ZnGa_2O_4$:Eu [11], and $ZnGa_2O_4$:Cr [12]. Still, the high efficiency and ease of manufacturing of the ZnS:Mn phosphor have kept it the dominant red phosphor in most ACTFEL displays.

1.3 Green Phosphor Materials

The first phosphor to achieve efficiency close to that of ZnS:Mn was the green light emitting ZnS:Tb phosphor. Although this phosphor is ideal due to its high luminous efficiency (near 1 lm/W) and its similar structure to the ZnS:Mn material, there are still some problems. The ZnS:Tb actually emits a broad 'greenish-yellow' light with CIE coordinates at x=0.30 and y=0.60 [2] as can be seen in Fig. 1.1. This means that the use of ZnS:Tb phosphors in full color TFEL displays would limit the range of colors to exclude a large portion of the green spectra or require filters hampering emission intensity. Despite these problems, the high efficiency of ZnS:Tb phosphors have propelled it as the green phosphor of choice in most full and multi colored EL displays today. Other green EL phosphor materials which have been studied include: ZnS:Cu [13], SrS:Mn [14], $ZnGa_2O_4$:Mn, $ZnGa_2O_4$:Tb, and $ZnGa_2O_4$:Tm [11], $ZnAl_2O_4$:Mn, Zn_2SiO_4:Mn and $MgGa_2O_4$:Mn [12]. None, however, have been shown as promising as ZnS:Tb.

1.4 Blue Phosphor Materials

The more difficult problem has been the development of an adequate blue phosphor material. Presently, most full color TFEL displays use one of two possible blue phosphor types, both of which use Ce as the activator ion. The first, observed originally in 1984 [15], is the blue green emission from Ce doped in alkaline earth sulfides (SrS, CaS). The second is the emission of Ce in thiogallate materials ($CaGa_2S_4$, $SrGa_2S_4$, or $BaGa_2S_4$). Although full color displays have been made using both technologies, there are still a number of problems associated with each.

Of the two, the alkaline earth sulfides, particularly SrS phosphors have a higher luminous efficiency [2]. The emission, however, is actually a broad blue green color with a main peak at 480 nm. As a result a blue filter is required for this phosphor which reduces its blue emission by a factor of 6 in luminance [2]. This broad blue green emission, however, may be incorporated into white SrS devices by incorporating red emitting Eu activators [16]. The thiogallates, on the other hand, produce a 'deeper' blue than the SrS devices. Unlike the ZnS and SrS materials, which are fabricated using the atomic layer epitaxy (ALE) technique the thiogallate phosphors require sputter deposition. This translates into further processing time. In addition, neither phosphor has the efficiency or adequate color hue needed for bright blue display performance. These problems, combined with the fact that the human eye is less sensitive to blue light than to red and green, make finding a suitable blue phosphor material a top priority for the TFEL display industry.

1.5 White Phosphor Materials

There are a number of approaches which have been taken to achieve a white TFEL phosphor material suitable for full color applications under filtering. SrS:Pr is a single activator phosphor which emits a white light [17]. The emission from this phosphor is actually comprised of several narrow emission lines which the eye integrates. Because the spectral lines are narrow, it is not a good candidate for filtering. The most common white phosphors investigated typically consist of two or more color phosphors combined in either a layered form or in a doubly activated form. Most incorporate SrS:Ce with either SrS:Eu, CaS:Eu, or ZnS:Mn [16, 18, 19, 20, 21].

1.6 Thesis Objectives

The purpose of the research presented in this thesis is to investigate overall improvements in ALE grown ACTFEL devices and in particular to explore alternatives and improvements to blue TFEL device phosphors and their incorporation into full color TFEL displays. Chapter 2 provides a review of the ALE technique, including a description of the modified F120 ALE reactor from Microchemistry LTD. A review of the structure and physics of EL display materials is presented in Chapter 3. All the phosphors discussed in this work were fabricated using the ALE technique. Chapter 4 reports the results of research done on the characterization and optimization of blue emission from SrS based devices. This includes a detailed study of the effects of film thickness and applied frequency on the emission of SrS:Ce devices, showing increased brightness for ACTFEL devices with proper choice of waveform and drive frequency. Additionally, the observed effects of codoping of materials including N, Bi, and O with the Ce activator in a SrS hosts, showing a shift toward the blue emission spectra are detailed. Blue emission from

tellurium activators in SrS, with brightness close to that of SrS:Ce phosphors will also be presented. This chapter also presents the growth of $SrCl_2$ using ALE and results of blue and violet emission from doping this host with various rare earth activators. This is followed by the presentation of the theory behind a new class of TFEL phosphor material based on multi-quantum wells (MQWs) embedded in a high band gap host in Chapter 5. Characterization of observed emission from this new class of phosphors is presented in Chapter 6 including film growth and comparison to the models presented in Chapter 5.

Appendices are also included detailing the growth of SrS devices using source materials from various vendors and providers in Appendix A; growth of ZnS devices from $Zn(thd)_3$ source material in Appendix B; and growth of various oxides using a variety of source components and methods in Appendix C. All of these appendices focus on the growth of such layers using the ALE technique for incoporation into TFEL devices. Finally, Appendix D includes the source code used in Chapter 6 to compare the observed results in the MQW phosphor materials to the model prediction.

Chapter 2

Atomic Layer Epitaxy

2.1 History

With the development of the efficient insulator stack sandwich structure for AC-TFEL display devices, came the need for a deposition method to meet the requirements dictated by the technology. In particular TFEL displays require the ability to deposit high bandgap (usually II - VI) materials with suitable activator dopants as well as pin-hole free insulators (usually oxides). The oxide materials should be pin-hole free to prevent electric breakdown. Additionally, the phosphor material growth thickness requires good uniformity and controlled thickness to assure uniform field distribution in all pixels. Finally, films should be processed at low temperature (suitable for glass substrates) and have few defects.

To meet these needs the Atomic Layer Epitaxy (ALE) procedure was established in the early 70's by Suntola and Antson [23]. The technique was developed specifically for the deposition of ZnS:Mn phosphor and Al_2O_3 films for use in TFEL devices. Original ZnS growth was accomplished using elemental Zn and S source materials. Later $ZnCl_2$ and H_2S source materials were incorporated.

This work lead to the first US patent on the ALE technique which was submitted from the Lohja Corporation out of Finland in 1975 and granted in 1977 [24]. By 1980 Lohja was commercially producing ALE reactors for the TFEL display industry for use in commercial manufacturing. In 1982, Lohja was awarded the SID prize for greatest

advance in the display field. Since this time the ALE technique has been extended to a number of other TFEL materials. Current commercial grade reactors produced by Microchemistry LTD of Finland have the ability to handle ten 8'x8' glass wafers per run.

2.2 ALE Operating Mechanisms

The major operating principals behind the successful growth via ALE is based upon the differences between chemical adsorption and physical adsorption. Chemical adsorption indicates a molecular bond between two atoms, which are very difficult to break. Physical adsorption, on the other hand, is only an attraction due to the Van der Waals forces between charges. These properties are illustrated in Fig 2.1. If appropriate conditions exist, reactants introduced to the substrate surface may be chemically adsorbed (i.e. chemically bonded to the surface). Any excess reactant, or by-product of a decomposed molecular reactant, will lie above the first layer and only be physically adsorbed. Because physical adsorption is a weaker bond, if the substrate is heated slightly, it is possible to produce enough thermal energy to break the physical adsorption bonds without breaking the chemically adsorption bonds of the first monolayer. This excess material can then be easily removed by an inert gas purge across the substrate leaving only a single monolayer growth. This monolayer now takes the place of the original substrate and the process can be repeated using the next reactant. With this method by alternately pulsing metallic and nonmetallic source materials the film growth of a required compound, such as Al_2O_3 or SrS, can be controlled to a single monolayer accuracy. Fig. 2.2 shows typical source pulsing and inert gas purging sequence used in such a procedure.

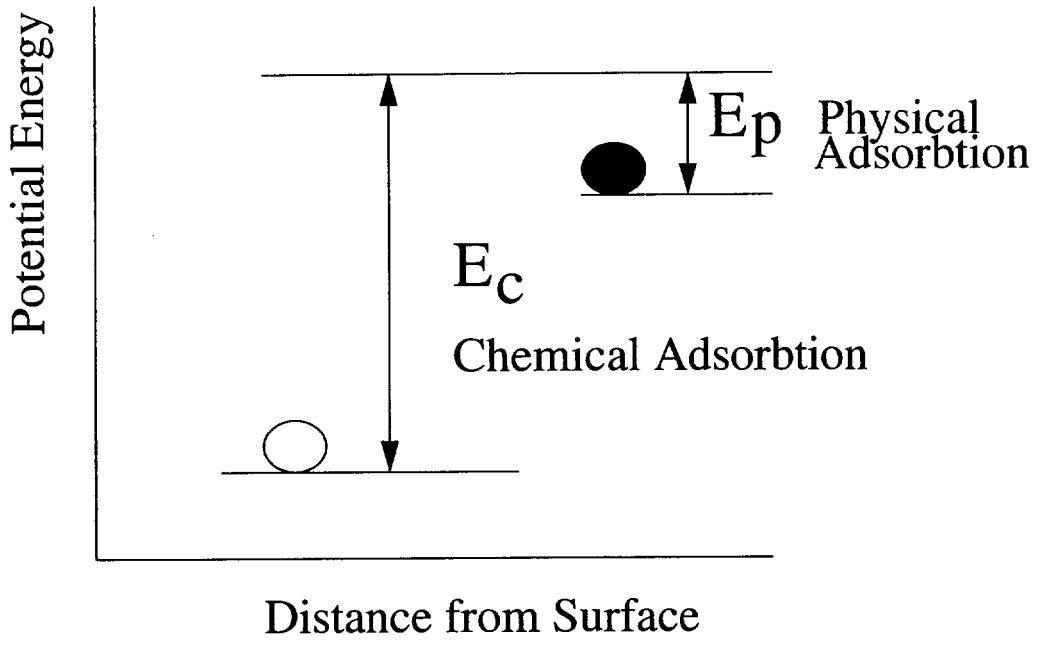

Fig. 2.1 Chemical Adsorption vs. Physical Adsorption

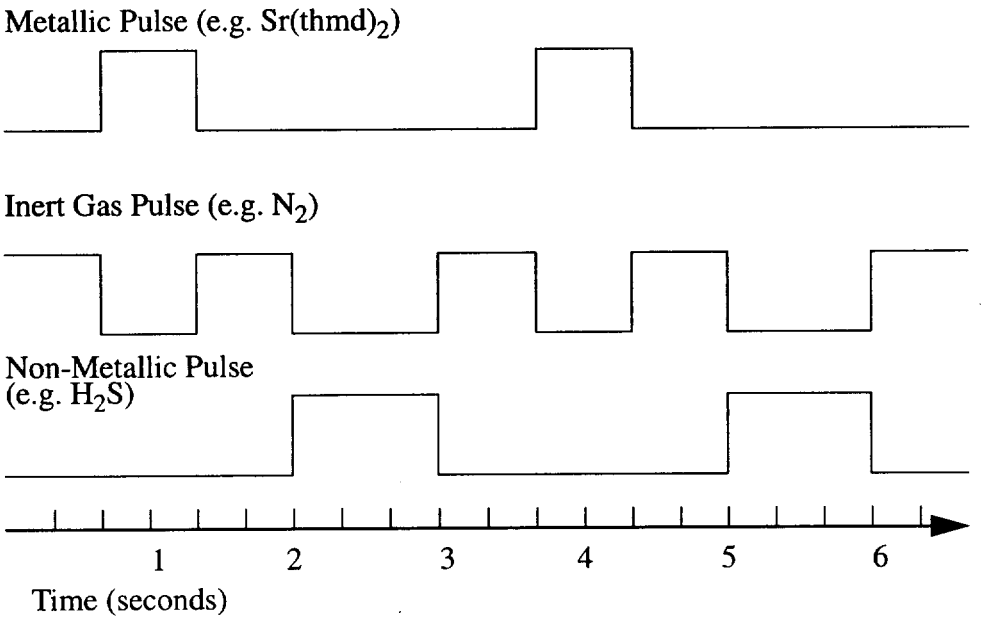

Fig. 2.2 "Digital Epitaxy" Pulsing in ALE Technique

The main factor in the ability to grow a given film using the ALE technique is the availability of suitable source components. In order for a material to function properly as a source for ALE, the material must be volatile at reasonable temperatures, have the ability to be chemically reactive with the substrate (no decomposition), and have the ability to react with complementary reactants to form a solid film of desired composition with by-products remaining in gaseous or vapor stage. Of the elements, only the group II and VI compounds, with a few exceptions such as phosphorous and arsenic, can serve as good source materials because these are the only elements which have shown to have adequate volatility under the necessary conditions. Of the binary compounds, the metal halides, especially the chlorides ($ZnCl_2$, $AlCl_3$, $TaCl_5$, etc.) have shown to work extremely well, though some evidence has shown that not all Cl is properly removed in many instances [25]. Another good candidate for metallic sources are the organometallics, in particular, the beta-diketonate complexes have been successfully used in many instances. The problems associated with these include lack of availability of thermal data, and low growth rate (due to large molecules). So far, few alternative metallic sources have been reported.

Suitable source materials should exhibit a high chemical adsorption energy for desired material growth and a low physical adsorption energy for undesired by-products and additional layers. The discrimination factor, η, can be defined as follows:

$$\eta = \exp\left(\frac{E_c}{E_p}\right)$$

Where E_c is the activation energy for chemical adsorption and E_p is the activation energy for physical adsorption [23]. When η is large there exists an adequate temperature range such that $E_p < kT << E_c$, where T is temperature in Kelvin and k is the Boltzman constant. Within in this temperature range, the film growth will produce one monolayer per cycle

and the growth rate should remain constant regardless of fluctuations in the temperature within the allowed range. This is more clearly indicated in Fig 2.3 [26].

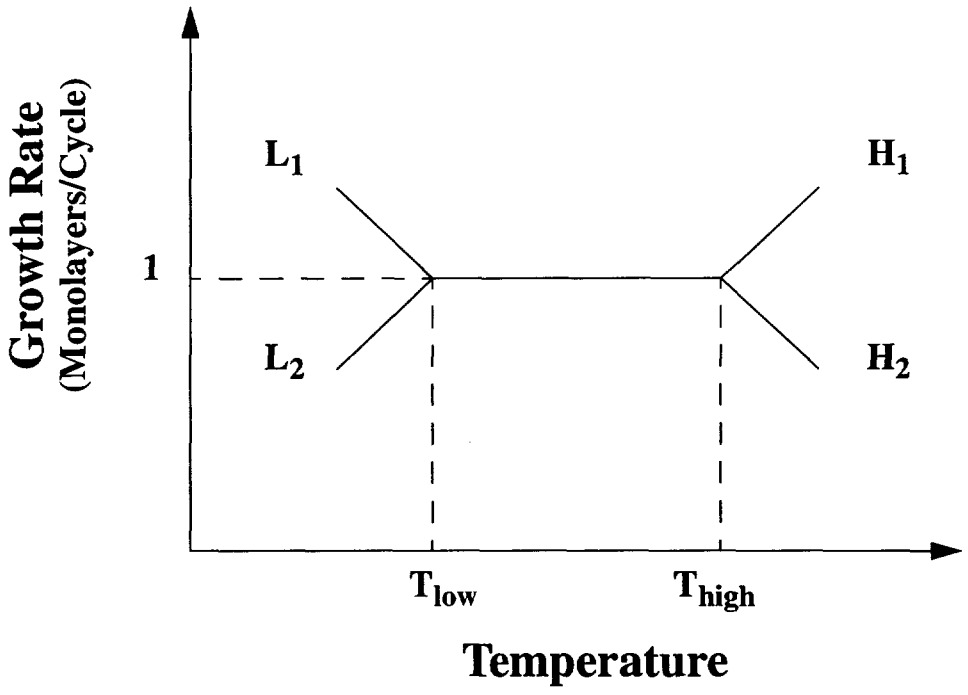

Fig. 2.3 ALE Process Temperature Window

In Fig 2.3, the operating range between T_{low} and T_{high} indicates the traditional ALE operating window. It is within this range that monolayer ALE growth can take place. Outside of this range there are four possible situations resulting in undesired growth characteristics. At temperatures below the ALE operating range, represented by L_1, condensation may occur where deposition of all materials including unwanted by-products and additional layers forms on the cold substrate. L_2 represents incomplete reaction where the substrate is not hot enough to support the necessary chemical adsorption. Above the ALE temperature window, represented by H_1, undesirable decomposition (CVD) can occur. This situation occurs when there is an undesirable deposition of the source material which

can chemically react with other materials. This is more common when large organometallic sources are used. It is also possible for a large substrate temperature to cause re-evaporation of the source, represented by H_2, resulting in low growth rate.

From the above discussion it is obvious that the substrate temperature is a very important parameter in the successful growth of thin films using the ALE technique. There are, however, a number of other variables which must also be considered. In order to produce a uniform monolayer growth on the substrate, the source material must flow sufficient material to the substrate to ensure enough reactant to cover the entire substrate. This indicates that attention must be paid to the reactor pressure, as well as the source temperatures. The reactants must also have adequate mobility across the substrate. This is defined by the choice of source material as well as the flow rate of inert purge material, as well as the time allotted for the pulse. The pulse time and flow rate of the inert purge between pulses is also critical to insure that all excess material is properly removed from the substrate prior to the next monolayer's growth cycle. Finally, reactor cleanliness must be insured to prevent film contamination.

2.3 Modified F-120 Reactor with Satellite Configuration

The original F-120 ALE reactor and its operating mechanisms have been previously described in detail [27]. Since this time, however, the reactor has undergone a major modification by Microchemistry designed to improve growth of alkaline earth sulfide (AES) based films for TFEL phosphor devices. Although the modification required fairly dramatic changes in the internal configuration of the system, the main changes can be seen in the substrate holder and gas valving of the system.

Much of the inner workings of the F-120 ALE reactor have remained unchanged. As seen in Figures 2.4, 2.5 and 2.6, there are still six source ports. Four (ports 1,2,4 and 5)

can be used for solid source materials. The remaining two (ports 3 and 6) are available for use with gas or liquid sources. The length of the reactor is still broken down into eight temperature zones, which increase in temperature from zone one to zone eight. Solid sources are placed in glass or titanium source boats within an appropriate temperature zone. The source boats are attached to thermocouples which are monitored by a 386 Compaq computer to determine the proper temperatures.

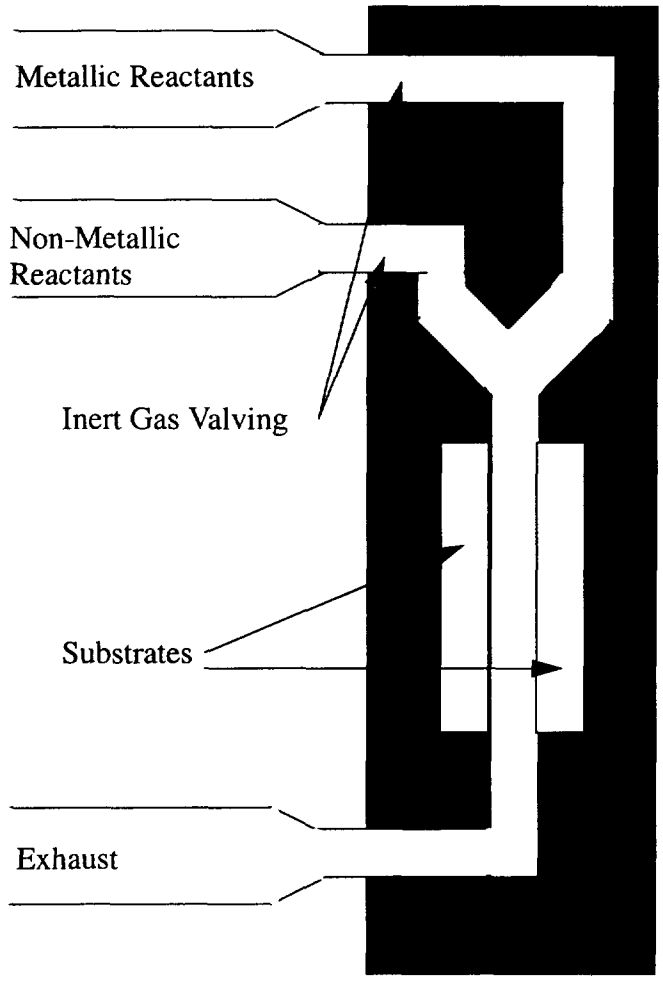

Fig. 2.4 Old F-120 Substrate Holder

Fig. 2.4 is a schematic representation of the old F-120 substrate quartz holder configuration. As can be seen in the figure, for this configuration the substrates actually lie perpendicularly to the direction of gas flow. In addition, the inlet lines leading to the substrate are very narrow. As a result, good film uniformity was difficult to achieve because the source vapors are often unable to expand fast enough to allow for complete coverage of the surface. A final problem associated with the original substrate holder configuration was the narrow size and large number of turns in the inlet gas lines. These corners acted not only as a place for moisture to collect (which has been shown to be detrimental to EL performance [28] and an obvious inhibitor to good vacuum pressure) but they also were difficult to properly clean, acting as a source of possible contamination into the films.

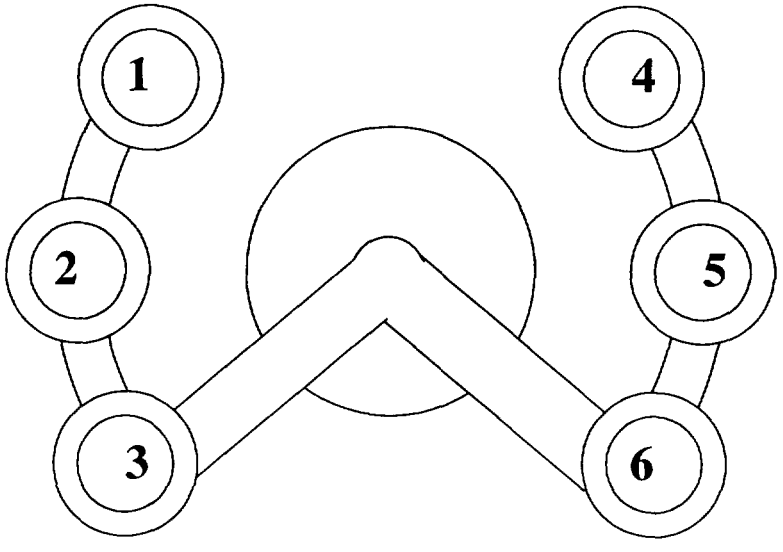

Fig. 2.5 New F-120 Substrate Holder (Satellite Configuration) Rear View

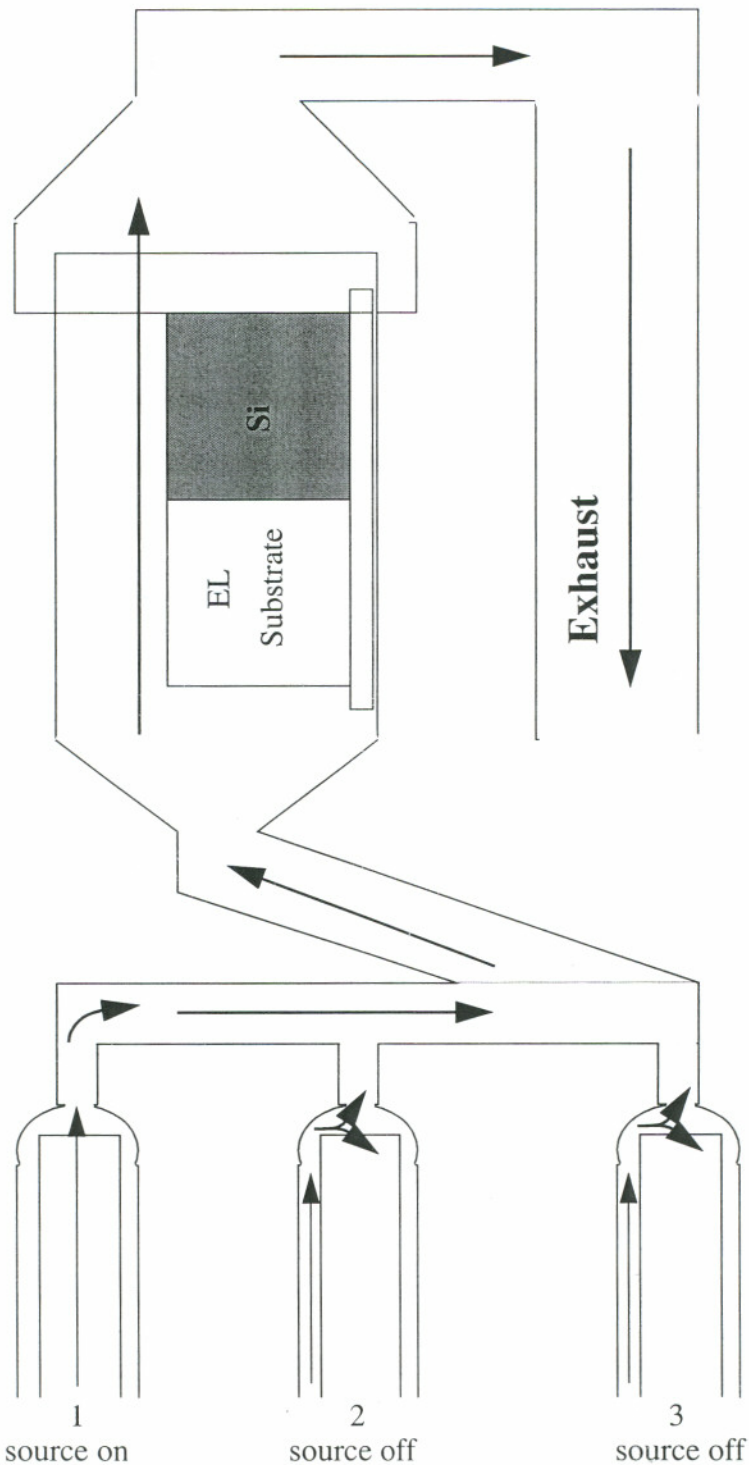

Fig. 2.6 New F-120 Substrate Holder (Satellite Configuration) Side View

The new configuration, which is depicted from a rear view in Fig 2.5 and from the side, showing valving, in Fig. 2.6, has been designed to allow for improved gas flow to the substrates. From Fig 2.6 it is clear that the substrates (which are now placed back to back, rather than face to face with a separator as in the old configuration) are now in a larger environment, allowing for improved gas flow across the surface. In addition added length in the substrate holder now allows for an increase in the number of substrates accessed per run from two 2"x2" substrates with the old configuration to four with the new configuration. This feature has allowed for the incorporation of Si substrates with each run as a means for improved film growth characterization using ellipsometry. In addition to these enhancements, the new substrate holder, though still somewhat less than optimum in the path that source vapors must flow to reach the substrate, has been created with larger flow lines for improved source flow. Also there are now very few narrow (below 90^{o}) turns in the path of the source flow.

The other major change in the F-120 reactor configuration involves the valving of the sources. In particular, the situation in which a given source is not being valved to the substrate has been altered. Now, as was the same with the original system, when a source is pulsed to the substrate it is done with a pulse of dry nitrogen through the inner source tube of the reactor. In the old configuration, when the source pulse for the reactant had ended, nitrogen was then flowed between the inner and outer source tubes. Part of this nitrogen flow traveled to the substrate and was used as a purge pulse to remove excess material from the substrate. The other part was used as a bypass for any continually flowing source material to exhaust, resulting in wasted source material.

Fig 2.6 clearly illustrates the new flow directionality during source pulsing. In the new configuration when a source is not being flowed to the surface the secondary nitrogen flow (which runs between the inner and outer source tubes) is now split with part going to

the substrate to be used as a purge, and the other part flowing back through the inner source tube in the direction of the source boat (away from the substrate). This design is intended to reduce the creation of unnecessary waste of source material. The portion of secondary nitrogen flow which does not flow back towards the source material is intended to act as a good barrier, preventing one source material in its pulse period from entering the inner source tube of another source material; although it should be noted that this is not ideal.

In general the new configuration has enhanced film growth. As expected, film uniformity has improved. In addition, the larger flow lines and decreased number of bends have allowed for decreased primary and secondary nitrogen flow rates, resulting in an overall reduction in reactor pressure. Further, films generally appear less cloudy and seem to have a longer shelf life, most likely attributable to a decrease in moisture and contamination during film growth.

There are still some problems associated with the new configuration. Contamination is still a large problem with the new configuration. The substrate holder with its six input valves is now more difficult to keep clean, unlike the older configuration which could be dismantled to smaller pieces which were then easier to clean. As source materials build up in the lines between runs, the chances of undesired contamination increase dramatically. Washing the substrate holder using an ultrasonic bath has been found to be a good tool in alleviating this problem.

Another problem is in cross contamination of the sources. Although the flow of secondary nitrogen has been designed to help prevent one source from contaminating another source line, this has been found to often be inadequate. Keeping metallic and non-metallic source materials separated during growth (i.e. non-metallics in ports 1, 2 or 3 and metallics in 4, 5 or 6) can help reduce this problem. Increasing the secondary flow rate may also help, but will again increase the overall reactor pressure. Possible design

improvements which could help in this aspect might include creating separate flow paths for each source material (instead of the present case where source coming in from port 1 must pass by ports 2 and 3 before reaching the substrate) or incorporating some type of mechanical valve at the end of each source tube which could completely close, and completely eliminate any cross contamination.

In order to make room for the substrates to sit parallel to the flow direction, the new substrate holder is now considerably longer than the old configuration. As a result, the substrate holder now takes two temperature zones as opposed to one in the old configuration. In the old configuration the substrate holders fit entirely into temperature zone 6. This leaves zones 7 and zone 8 for buffers. The new reactor now requires zone six for the connecting area between the substrate holder and source tubes. Zone 7 then becomes the substrate temperature zone, leaving only zone 8 as a buffer. The problem associated with this is the fact that because there are only six ports, and because the source tubes only extend to temperature zone 5, it is impossible to have a thermocouple accurately control the inside temperature in all the zones up to and including the substrate zone. At present, one thermocouple is used in the exhaust tube to accurately measure the temperature in the substrate zone, which can leave undesired build up on the thermocouple. Temperature zones 1 through 5 are monitored with thermocouples through five of the source ports. Because the flow path turns by 90^{o} in the substrate holder at zone 6, it is impossible to have a thermocouple monitor this region precisely. By carefully monitoring the actual heater temperature in zone 6, compared with the heater temperatures and inside thermocouple temperatures of neighboring zones 5 and 7, one can help to assure that the inside temperature of zone 6 is hotter than zone 5 and cooler than zone 7, preventing any deposition on the glassware prior to the substrates. This is a fairly tricky art. In addition the temperatures of the hottest source material and of the substrate may on occasion be very close.

(See for example details on the growth of CdSe quantum wells in SrS in Chapter 6.) This allows only a very small window of accuracy for properly programming zone 6. This problem only adds to the problems of contamination and cleaning in the source flow region between the source tubes and the actual substrates.

The last problem associated with the new design involves the complexity and fragility of the glass substrate holder. Because glass is so fragile it is very easy to break, particularly during the difficult cleaning process. The fact that the piece is fairly complex means that if the substrate holder should be broken it is very difficult and costly to have replaced. This might be alleviated by partitioning the substrate holder into smaller pieces, for example separating the satellite arms which connect to the source tubes from the substrate chamber. This could help ease the cleaning process and reduce any amount of replacement work. The obvious problem for this comes in the creation of proper seals to adequately contain all the pieces.

2.4 Characterization of Film Growth

To analyze film thicknesses and uniformity on glass and standard ATO/ITO substrates a DekTak IIA profilometer was used. For Si or GaAs substrates, a Gaertner Scientific ellipsometer with a standard HeNe laser was used. These measurements have proven extremely useful for optimizing ALE growth conditions. X-ray analysis was also performed on select samples to determine crystalline quality, using the Siemens Grazing Incident Angle X-ray Diffractometer.

Chapter 3

Electroluminescent Displays

In order to give a better general understanding of the principles involved in alternating current thin film electroluminescent (ACTFEL) devices, some back ground information is presented below. A brief history of EL is presented for context, followed by a description of the ACTFEL device structure, operating mechanisms and device physics.

3.1 History of Electroluminescence

The first observation of electroluminescence came in 1936 when Destriau observed a green emission from ZnS:Cu powder submerged in oil due only to an electric field [4]. Emission from EL phosphors in a powder has been studied, for some time, as a possible cold luminaire to replace conventional tungsten light bulbs, with Sylvania producing EL lamps in the early 50's [29]. Though a number of flat panel displays were proposed for the powder technology [30, 31] its low intensity and short life span has reduced current research into its use in any common commercial devices.

With an advance in semiconductor technology and thin film processing in the 1960's, the second form of electroluminescence came into existence: thin film electroluminescence (TFEL). These devices consist of thin film semiconductor materials doped with a suitable activator and coated on a substrate. Considerable research into TFEL phosphors, consisting of various high band gap semiconductors hosts doped with a number of rare earth activators, was conducted at Bell Labs in the 70's [32]. Although the researchers did observe light from the devices, they were unable to overcome the limited life spans.

For this device structure (phosphor on substrate) the device life span is limited by the number of available electrons free to be accelerated across the phosphor.This problem was not solved until the early 70's when Inoguchi proposed the now common 'double insulating sandwich' structure [3, 6]. With this structure, considerable leakage current flowing through the device is prevented. Consequently the device can keep a sufficiently high electric field for EL operation across the active layer without breakdown. This was the breakthrough which was desperately needed to enhance life times for EL devices. Still, it was not until the late 70's when IBM published its findings on TFEL [33] that the scientific community realized the significance of ACTFEL technology.

In 1978 Sharp demonstrated the first experimental high luminance, long lifetime, matrix addressed flat-panel TV from TFEL at the 1978 Consumer Electronics Show in Chicago [1]. Commercial monochrome EL Displays became a reality. Today commercial ACTFEL displays are manufactured in Japan, Europe, and the US. Full-color VGA EL display is presently available through Planar America. The fact that TFEL displays are based on thin film technology and have very few free or loose components lends to its rugged characteristic, making it an ideal technology for extreme environments. In addition, TFEL displays are emissive type displays with high contrast and large viewing angle, making them an attractive alternative to other existing technologies.

3.2 ACTFEL Device Structure

The first efficient TFEL device was the AC structure reported on by Inoguchi [6] who proposed the double insulator stack structure as a means to increase device life spans. This basic device structure has remained for the most part unchanged since its original inception. Fig 3.1 illustrates a typical ACTFEL device structure.

The structure begins with a glass or other suitable, transparent substrate. The first film deposited on the substrate serves as one of the contacts. Because the light from this structure must pass out through the glass it is necessary that this electrode be transparent. The most common bottom electrode is ITO (Indium Titanium Oxide). Others which have been used include SnO_2 and In_2O_2 [3]. Typically this layer is deposited using thermal evaporation or sputtering techniques. The top electrodes are less critical. Al is considered a good material not only because it acts as a good conductor, but also because it is a near ideal reflector and thus helps to reflect the emitted light back in the direction of the substrate.

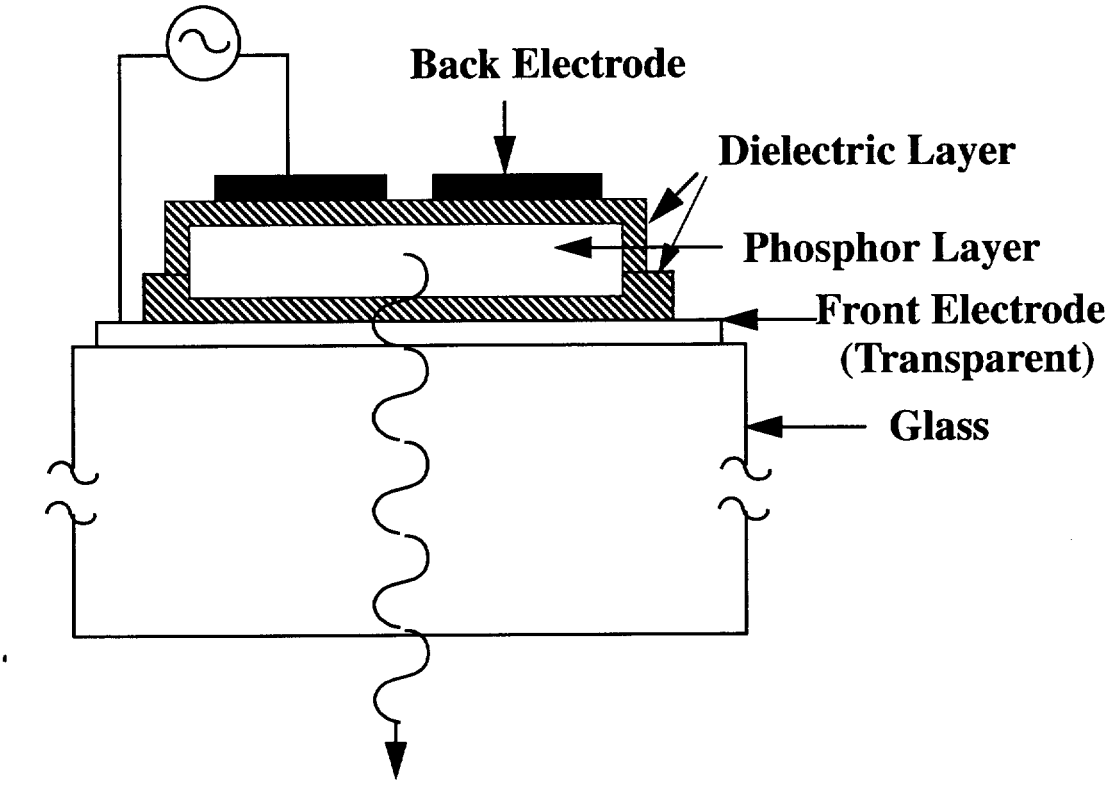

Fig. 3.1 ACTFEL Device Structure

In general the top and bottom insulating layers (which are not necessarily made from the same material) should have a high dielectric constant to concentrate the electric field across the phosphor region and be of high strength to prevent breakdown [1]. It is impossible, however, to completely eliminate pinhole electrical breakdown. In addition to serving as insulators, these layers can also act as protection layers for the phosphor materials, preventing unwanted oxidation or contamination from the air. Typical insulating layers include BTO (Barium Tantalum Oxide), ATO (Aluminum Titanium Oxide), and Al_2O_3. Others which have been used include SiON, Y_2O_3, and Si_3N_4 [3]. Amorphous films are generally considered superior in quality to crystalline layers because they tend to have fewer defects and are less susceptible to contamination. The choice of insulator can have an effect on the device efficiency, luminance, and voltage performance, and thus is an important factor.

Typical phosphor materials have been summarized previously in Chapt. 1. In general the phosphor host material must have the ability to withstand high fields, allow for the nearly loss-free acceleration of electrons, have a bandgap larger than the electron transition level of the activator ions, and have the ability to be evenly doped and deposited onto the substrates [34]. Activator atoms can vary widely and in general need only to be able to be easily incorporated into the host material and produce highly efficient emission in the visible spectrum upon impact excitation. Furthermore, to ease incorporation into the host, the ionicity of the activator should match that of the host ion which it replaces. The rare earth atoms act as good activators because they tend to remain ions under high fields and because they retain their spectral output and transition probabilities when incorporated into a crystalline environment. Typical processes for the deposition of both insulator films and phosphor layers are thermal evaporation, e-beam evaporation, sputtering, chemical vapor deposition (CVD) and atomic layer epitaxy (ALE).

3.3 Device Physics

The operating mechanisms for the sandwich stack ACTFEL phosphor devices are illustrated in Fig. 3.2 below. The five essential processes that each pulse of the applied bipolar voltage signal must achieve for efficient EL emission are: 1) carrier injection into the phosphor material (through tunneling), 2) high field acceleration of the electrons in the conduction band of the host material, creating 'hot' electrons, 3) impact of 'hot' electrons with activator ions, 4) characteristic luminescence and 5) trapping of electrons in the interface states of the anodic interface. The whole process can then be reversed with the opposite polarity, reducing accumulated polarization charge during the reverse pulse. This gives rise to the extended lifetimes of the sandwich structure ACTFEL devices. Each of the necessary components is described in greater detail below.

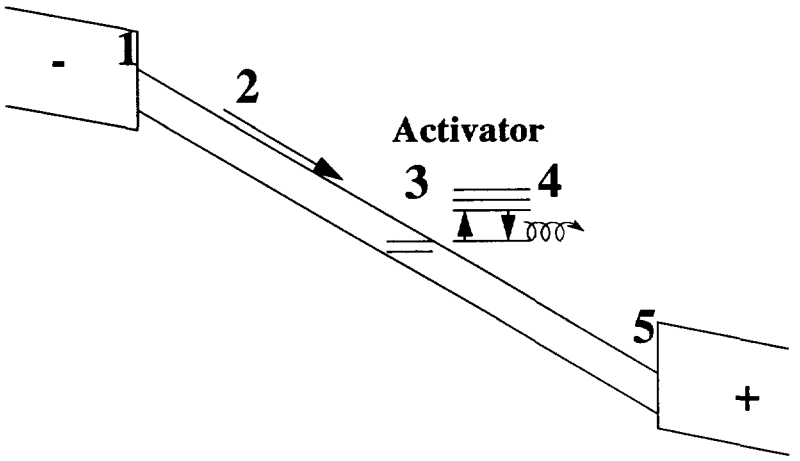

Fig. 3.2 ACTFEL Band Model

3.3.1 Carrier Injection

Experimental evidence has revealed that the electron is the primary conducting charge in ACTFEL devices [3]. For this reason the electron transport mechanisms are of vital importance in the understanding of ACTFEL displays. It should be noted, however, that the effect of holes cannot be completely discounted.

The most common theory for the incorporation of the electrons into the host material is tunneling [35]. When the applied field reaches a certain threshold level, V_{th}, electrons trapped at the oxide/phosphor interface begin to tunnel out of the interface states and enter into the conduction band of the phosphor host material, through the Poole-Frenkel effect [36]. The precise location and distribution of the interface states is still uncertain and may depend on both the oxide material and phosphor material.

In order for luminescence to occur, the electrons must excite the activator. This is done through impact excitation. In order for excitation in the visible range, the electron must impact the activator site with at least 2.0 eV [37]

3.3.2 Electron Impact and Excitation Mechanisms

Upon acceleration within the phosphor, some of the 'hot' electrons will collide with activator sites. This collision may result in impact excitation or may even be strong enough to remove an electron from the activator to the conduction band of the host, resulting in impact ionization. The consequent deexcitation of an excited activator electron or later recapture of an electron by an ionized activator produces the characteristic radiative emission.

Impact excitation is typically broken into two categories, direct and indirect. Direct impact excitation, first introduced by Krupka to explain the emission of Tb in ZnS [32], describes the intra-shell emission of the activator, typically rare earths, upon excitation by a direct impact from a hot electron under the influence of a high electric field. This can be considered an inelastic collision.

The amount of light produced, and hence the efficiency of the device, depends upon the number of collisions which occur within the phosphor at each pulse and the efficiency by which the collision energy is converted to light emission. The probability for an electron to impact an activator is directly proportional to the activator's cross section. This cross section is dependent upon three variables: host-lattice screening, excitonic energy, and relaxation rate. These criteria further reduce the choice of potential activator materials.

Indirect impact excitation involves excitation from complex activator sites (consisting of at least two atoms, activator and coactivator) one of which relaxes at a slower rate. In this multi-step process an excited atom within the complex site may transfer some of its energy to a closely lying neighbor within the site [38]. This results in excitation and eventual relaxation and emission. Although energy is lost upon transfer from one atom to its neighbor, indirect impact excitation can enhance efficiency because of the increase in total activator cross-section. Creation of complex centers, however, is not a simple task. Special care must be taken to optimize codoping concentrations and locations with respect to the traditional activators. In addition, the effects of charge compensation of the activator with respect to the host lattice must be considered. This topic will be discussed in more detail in Chapter 4 in the context of specific materials.

3.3.3 Excitation from Rare Earth Activators

The rare earth (RE) atoms are a very attractive choice of activator, specifically when incorporated in the alkaline earth sulfides (AES), due to a fairly good match in ion size. Another reason for the attractiveness of RE atoms can be seen in their atomic composition. The RE atoms occupy a special position among the elements because of their unique outer electron configurations which includes two unfilled orbitals. All have a partly filled 5d orbital with an electron configuration of $5d^1\ 6s^2$ surrounding the xenon core. Each additional electron then fills a position in the 4f orbital progressively filling up to 14 electrons. In traditional EL host materials such as ZnS or SrS the REs exist typically as either 2+ or 3+, with the 6s electrons being stripped first, followed by the 5d singlet.

What makes the REs unusual in these circumstances is the fact that the unfilled 4f orbitals extend to less than 50% of the RE^{3+} atomic radii which are mainly determined by the filled $5s^2$ and $5p^6$ shells. For this reason, the effects of the host lattice on the RE activator are seen mainly by the outer lying orbitals, leaving the unfilled 4f orbitals shielded. This allows for seemingly contradictory features like semiconductor-type devices with atomic-like emission. It should be noted that this peculiar set of circumstances does not eliminate other elements from producing efficient EL emission. The difference is that in cases where the unfilled orbital is not shielded from the host lattice the excited energy levels may be changed by the Coulombic attraction of the host ions. As a result it becomes very difficult to predict the emission from such centers.

Upon impact, an electron of the RE ion in the partially filled 4f ground state can be excited to the outer 5d orbital or within the 4f orbital. For divalent RE ions, the transition typically occurs with the 5d shell. For most trivalent RE ions the transition is within the 4f shell. One notable exception is Ce^{3+} which has only one 4f electron, resulting in transitions with the 5d shell, similar to the divalent RE ions.

4f-4f transitions are parity forbidden, except for the small electric dipole transition rate. Because of the small cross section involved in these transitions, the efficiencies for most trivalent RE ions are very small. The parity selection rule, may be softened in the case of indirect impact excitation where additional atoms help to increase the total cross section. In such instances the emission lifetimes are relatively large and emission spectra are typically wide.

4f-5d transitions, however, are parity allowed and are characterized by shorter lifetimes. The 5d orbitals, unlike the 4f orbitals are not shielded from the lattice material. In the case of the alkaline earth sulfides (AES) the d-like conduction band of the host material is relatively low lying and may actually result in the loss of the electron to the conduction band, creating a free electron. For this reason the emission due to impact excitation in the AES materials is typically small compared to materials like ZnS. In addition, because the 5d orbital strongly follows the conduction band minimum, the emission spectra of such ions is far more dependent upon the host material, whereas the emission spectrum from trivalent ions is affected little by the host material in which it is incorporated.

3.3.4 Recombination and the Effects of Space Charge

As has already been mentioned, it is possible, particularly in the case of the AES host materials, for the RE ion to lose an electron due to impact with hot electrons. Upon first thoughts this may seem detrimental to phosphor emission, under certain conditions, however, it may actually help to improve efficiency. Upon application of the field, electrons tunnel from the interface and are moved to the anode side of the film. In addition, electrons from ionized RE ions near the cathode of AES hosts will also move toward the anode. It also results in an accumulation of electrons at the anodic interface and the cre-

ation of polarization charge which acts in opposition to the applied field. This creates a space charge in the crystal. Because the number and position of the ionized REs will increase and change with the field, (the point representing charge neutrality along the line from the anode to cathode) the space charge 'moves'. This is coined as 'dynamic' space charge [39].

Upon removal of the external field the build up polarization field begins to move any untrapped accumulated electrons at the anodic interface in the direction of the cathode. In many cases the polarization field is strong enough to induce impact excitation. In addition, because of the low lying AES conduction band, some RE ions can actually capture a conduction electron in the 4f5d orbital, resulting in additional emission. This is known as recombination and as might be expected is characterized by low efficiency. The emission from recombination is typically associated with the falling edge of the voltage pulse, as opposed to impact excitation which can be associated with the leading edge. Because the AES host materials are more likely to result in ionization of the activator upon impact, recombination is more common in these materials. It is far less prevalent in ZnS or other similarly configured materials.

Upon completion of an initial voltage pulse the entire procedure is repeated with the polarity in the opposite direction. This will help to eliminate any additional polarization charge in the phosphor material. It should be noted that because the insulators on either side of the TFEL structure are typically not identical, that parameters such as V_{th} and the amount of polarization charge accumulated, may vary with the directionality of the pulse.

3.4 ACTFEL Device Characteristics

From a manufacturing or user point of view, the key to any display device is performance. In particular, the key parameters for any phosphor to be used in a display are available color or emission spectrum, total achievable brightness, and luminous efficiency. As has already been mentioned, the present limitation for full color ACTFEL displays is the development of a bright, efficient blue phosphor material. Measurements of a phosphor emission spectra and CIE coordinates are useful in determining the device color performance.

A typical plot of EL brightness vs. voltage is shown in fig 3.3. From this figure it can be seen that after the threshold voltage is met the brightness increases roughly linearly with voltage for sometime until it reaches a point where it begins to saturate. This is a useful characteristic which can be utilized to modulate on and off stages of any given pixel. These measurements also reveal information about the device's total brightness capabilities as well as efficiencies. Other variables such as frequency dependence and wave-form dependence have also been shown to have an effect on the brightness of a given pixel. More information on this will be presented in Chapter 4.

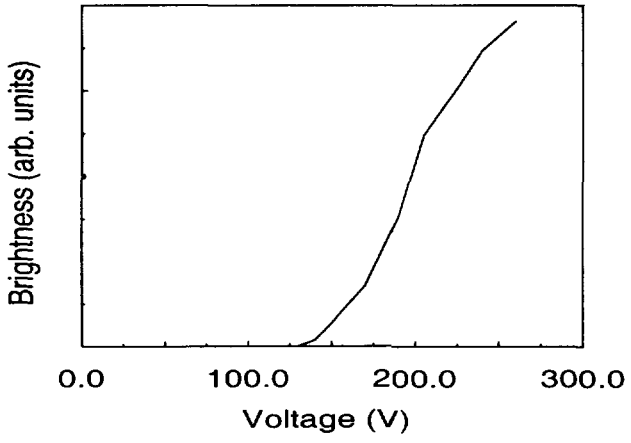

Fig. 3.3 Typical Brightness vs. Voltage Characteristics for ACTFEL Phosphors.

Chapter 4

Blue Emission from SrS Hosts

As has been mentioned previously, the alkaline earth sulfides with cerium activators are becoming among the most widely studied and potentially most promising of the blue TFEL phosphors. In particular SrS:Ce, which has a slightly blue shifted emission spectra from its BaS:Ce and CaS:Ce counterparts [40], has already found its way into commercial devices. Since its inception it has become one of the most commonly used phosphors for blue emission. There are, however, still a number of limitations associated with this phosphor. The operating principles of this type of phosphor are far less understood than they are for its ZnS counterparts. Additionally, the fairly low luminous efficiency and the wide blue-green emission spectrum from SrS:Ce devices are less than ideal for a true blue phosphor, though this second feature may be exploited with the additional use of Eu doping (which is a red emitter in SrS) to produce a 'white' emitting phosphor. In an attempt to address these limitations a great deal of research has been performed on the SrS family of phosphors. Though it is becoming one of the most widely studied II-VI materials, there is still relatively little information available on this material.

4.1 SrS:Ce Phosphors

Using the procedure optimized for SrS growth with $Sr(thd)_2$ organo-metallic source from Planar America (see Appendix A) a number of devices were created with varying levels of Ce doping. producing phosphors approximately 350 nm thick. The devices were grown on substrates consisting of glass with an ITO conducting layer and an ATO insulating layer provided from Planar America. The back oxide, 180 nm Al_2O_3, was grown using the F-120 ALE reactor with the Al-isopropoxide source, detailed in Appendix C. Fig 4.1 shows the Brightness vs. Voltage at 60 Hz for SrS:Ce devices doping ratios varying from 1:250 to 1:20. For historical reasons, all devices were pulsed with the standard bipolar waveform [27, 35]. It was found that as the doping level increased, the overall brightness initially increased. Additionally, an increase in the threshold voltage of the device was observed. This can be understood in the increase in the number of potentially activated ions. As the doping level continued to increase a saturation point was observed. Further doping beyond this point actually reduced the optical efficiency (see 1:20). This phenomenon may be related to a number of reasons, including an increase in charge build up from the Ce^{3+} ions, reduced crystalline quality, or an increase in non-radiative deactivation mechanisms from closely neighboring activators.

As can be seen in Fig. 4.1, a doping level of 1:40 produced the highest overall achievable brightness. Unfortunately, due to capacity limitations of the F-120 reactor, doping levels in this range required interrupting the run cycle to refill the $Ce(thd)_3$ source boat. This made the process much more time consuming than those with less activator doping. Because the films produced with a doping level of 1:80 were very close to the 1:40 levels in overall brightness, and did not require a time consuming interruption, this level was chosen as the standard for all SrS:Ce related work.

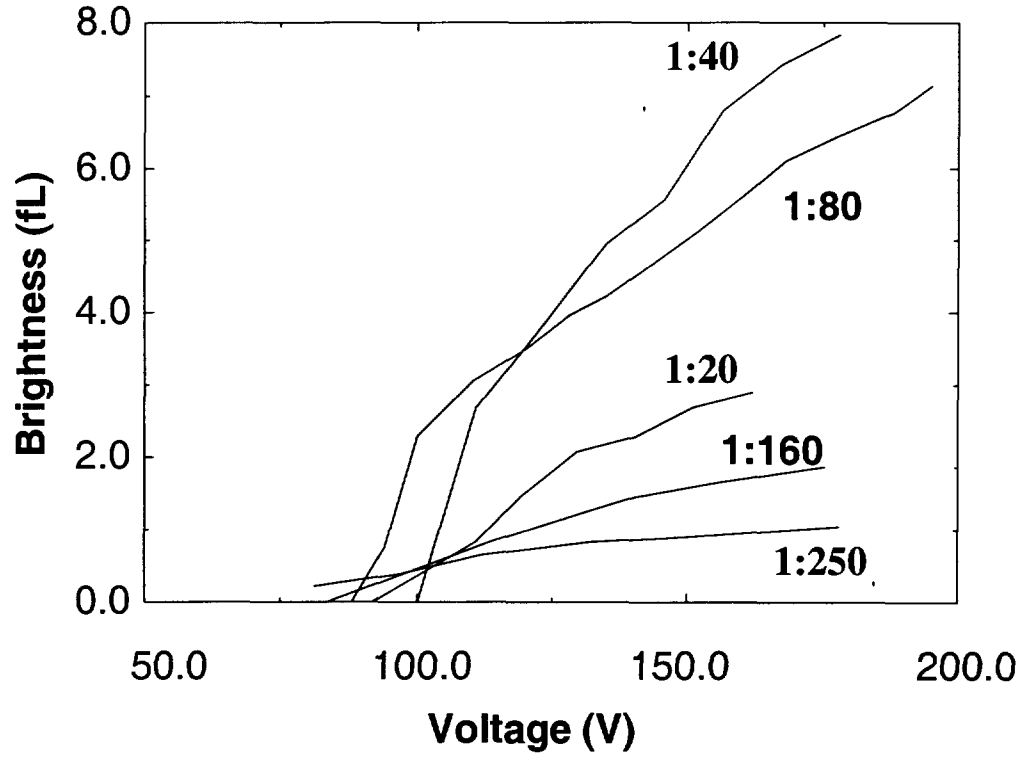

Fig. 4.1 Brightness vs. Voltage for SrS:Ce with varying doping levels.

4.1.1 Brightness vs. Thickness Measurements

After having resolved the maximum doping level for the SrS:Ce phosphors, it was observed that similar devices produced by Planar America showed significantly higher total brightness. The main difference between the devices fabricated in this process and those created by Planar America was the overall size of the phosphors. The average phosphor thickness for phosphors created in the F-120 environment was 350 nm, compared to 1200 nm for the standard devices received from Planar America. For this reason the standard SrS:Ce device was compared against a device grown under the same conditions of three times greater thick-

ness, each with the chosen 1:80 Ce doping level. The growth procedure for the thicker phosphor required interrupting the ALE run twice to refill the source boats. These growths resulted in film thicknesses of approximately 0.35 and 1.05 microns. As can be seen from the output in Fig 4.2 the increase in overall thickness did improve the total brightness achievable. This can again be attributed to an increase in the total number of activators which may be excited. In addition there is a dramatic increase in threshold voltage with the increase in overall thickness. This can be easily understood in terms of the increase voltage required to accelerate sufficient electrons across a larger phosphor layer.

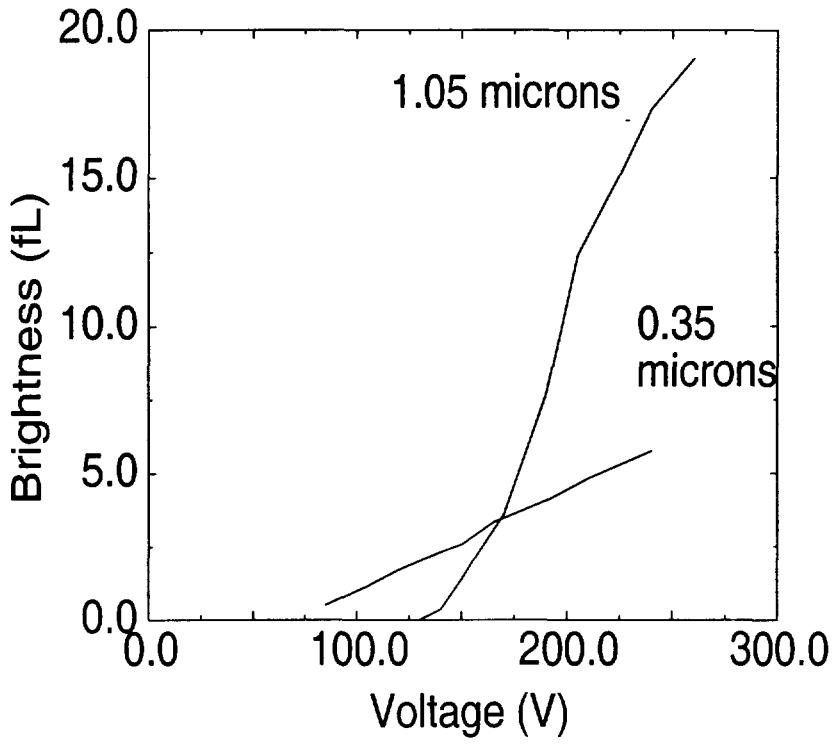

Fig. 4.2 Brightness vs. Voltage for SrS:Ce with varying phosphor thickness

4.1.2 Effects of Drive Frequency and Waveform on Emission Properties

Previous work on the effects that the driving frequency of a device play on its overall performance have shown an overall increase in brightness with increasing frequency [41]. In general, the increase was associated with an increased refresh rate. In an effort to gain more insight into this phenomena, measurements of the phosphor brightness vs. drive frequency were performed on the thicker (1.05 micron) SrS:Ce device at a constant voltage of about 200 V (approximately 40 V above threshold for these devices at 60 Hz driving frequency). Here the standard bipolar waveform, as shown in Fig 4.3, denoted as "bipolar", was used as the driving waveform. In addition a symmetrical triangular waveform centered at 0 V, denoted in Fig 4.3 as "sawtooth", and a symmetrical sinusoidal waveform centered at 0 V, denoted in Fig. 4.3 as "sine" were also used. In the latter two cases, the width of the pulse, and slope of the curves was determined by the applied frequency, unlike the bipolar which is a fixed waveform. In all cases the devices were driven with an amplitude of 200 V.

The results are shown in Fig. 4.4. In all cases, it was found that as the frequency increased there was an initial increase in observed brightness. This was followed by a saturation period where brightness leveled off. Finally, as frequency was increased further, brightness began to decrease. In fact by increasing the frequency far enough in all cases the device was turned "off". As can be seen from the figure, however, the exact frequency range over which the phosphor was operational and the total brightness observed, changed greatly depending on the applied waveform.

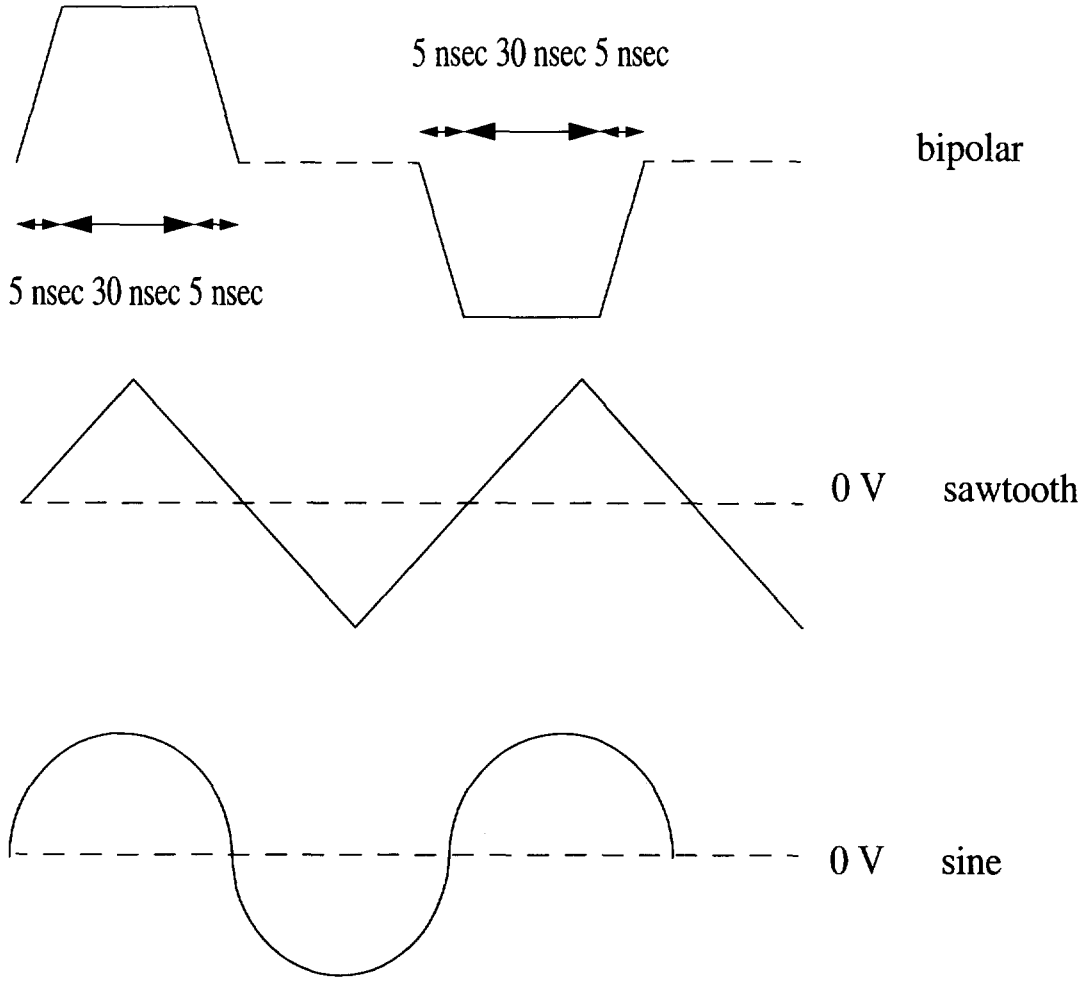

Fig. 4.3 Driving Voltage Waveforms

From Fig. 4.4, it is clear that the sine and sawtooth waveforms were operational over a significantly larger frequency range. Further, the sine and sawtooth waveforms were substantially brighter than the case of the bipolar wave. This is not true at all frequencies. At lower frequencies, it is actually the bipolar waveform which produced the brightest emission. Fig. 4.5 shows the brightness vs. voltage for this device at 60 Hz for both the bipolar and sine waveforms.

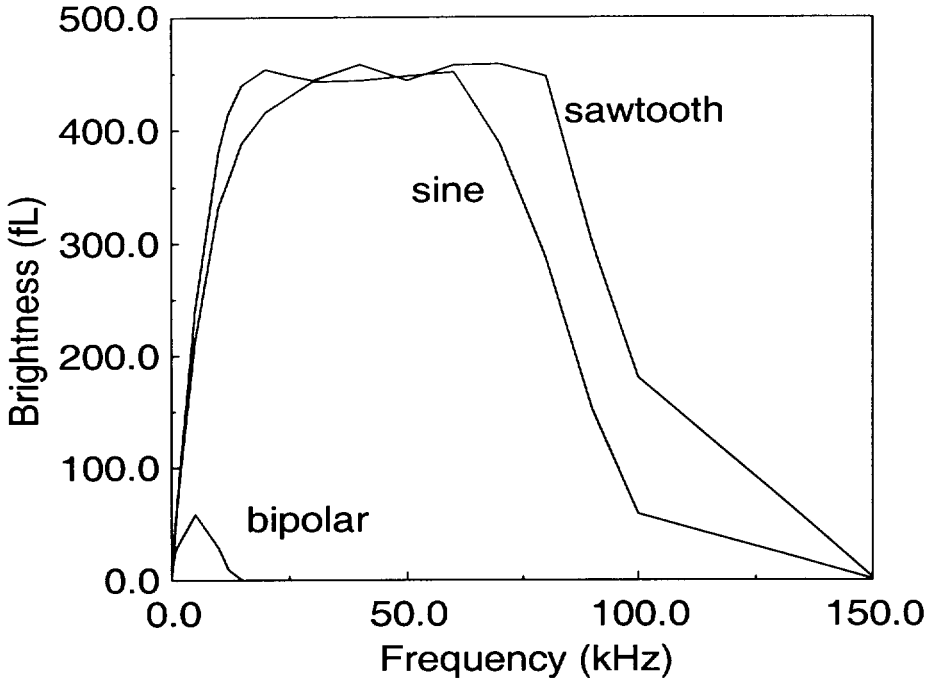

Fig. 4.4 Brightness vs. Frequency for SrS:Ce devices with bipolar, sawtooth and sine wave driving waveforms at 200 V.

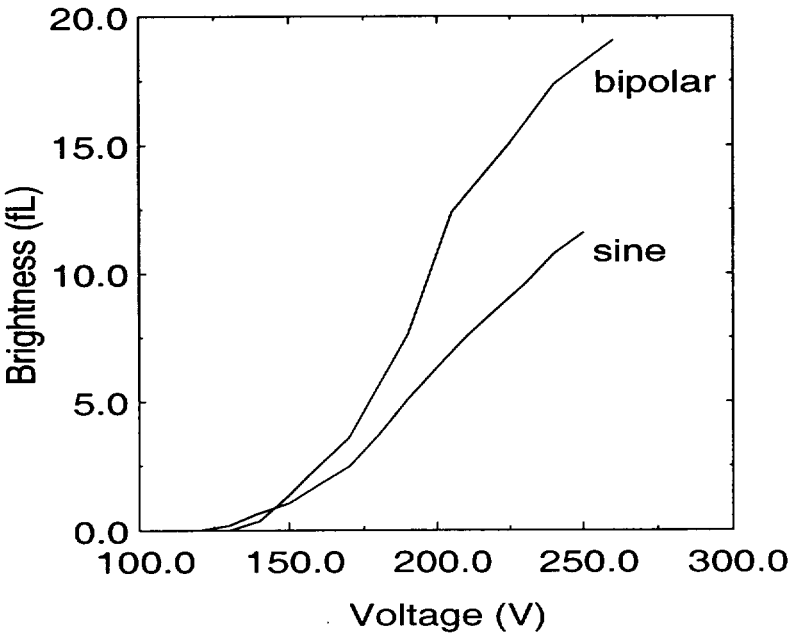

Fig. 4.5 Brightness vs. Voltage for SrS:Ce at 60 Hz for bipolar and sine waveforms at 200 V.

In an effort to determine whether this observed phenomenon is restricted only to the alkaline earth sulfide devices, and what role, if any, space charge plays on this phenomena, the same experiment was performed for ZnS:Mn devices with a doping level of 1:40 and driven at 200 V. These devices were grown using the $Zn(thd)_3$ precursor in a procedure which is detailed in Appendix B. The results are shown in Fig 4.6. From the figure it can be clearly seen that the ZnS:Mn devices exhibit a similar behavior seen for SrS:Ce devices. It is important to note, however, that the two different phosphors do not have the exact same operational range with frequency. This indicates that multi-colored phosphors produced using these phosphors may have very different performances for the same voltage at different frequencies.

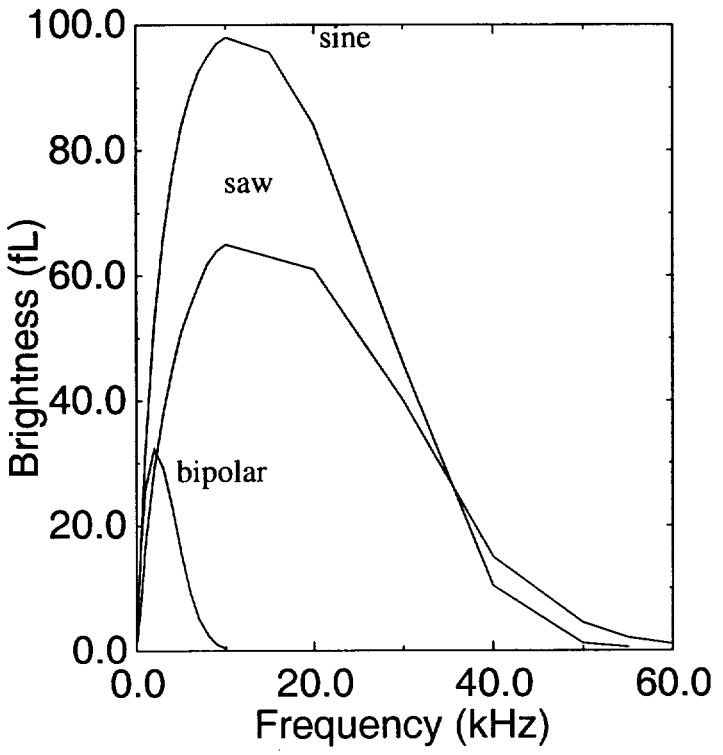

Fig. 4.6 Brightness vs. Frequency for ZnS:Mn devices doped 1:40 with bipolar, sawtooth, and sine wave driving waveforms at 200 V.

One possible reason for the increased brightness observed for the sine and sawtooth waveforms stems from the relation of the waveform shape to the frequency. For these waveforms, as the frequency is increased the magnitude of the slope of the voltage curve at the rise and falling edges increases. From Kirchoff's laws it is known that current is proportional to the slope of the voltage. As a result, for these waveforms, as the frequency is increased the current is also expected to increase. This can lead to an increase in the number of excited activators and hence an increased brightness. The bipolar waveform, unlike the sine and sawtooth has fixed rise and fall times. At low frequencies the slope of the voltage curve for the sine and sawtooth will be lower than that of the bipolar. This may help to explain why the bipolar waveform exhibited greater brightness at lower frequencies.

To verify the effects of frequency on current and to help identify what role it plays in the observed brightness effects, the maximum current across the thicker SrS:Ce phosphor was measured for varying frequency for both the bipolar and sine waveforms. Fig 4.7 shows the effect of frequency on maximum current across the phosphor. As anticipated, there is an increase in the current with frequency for the sine wave. Somewhat surprisingly, however, is the very similar situation for the bipolar waveform. In both cases the current maximum increases with current until it reaches a saturation point where it begins to level off. The frequency where the current saturates corresponds fairly close to the frequency where the maximum brightness occurs for both waveforms. It should be noted that the maximum currents observed for the sine were substantially greater than those of the bipolar. Unlike the brightness effect the max current remained saturated and did not decrease in both waveforms. This phenomena was observed for all the devices tested.

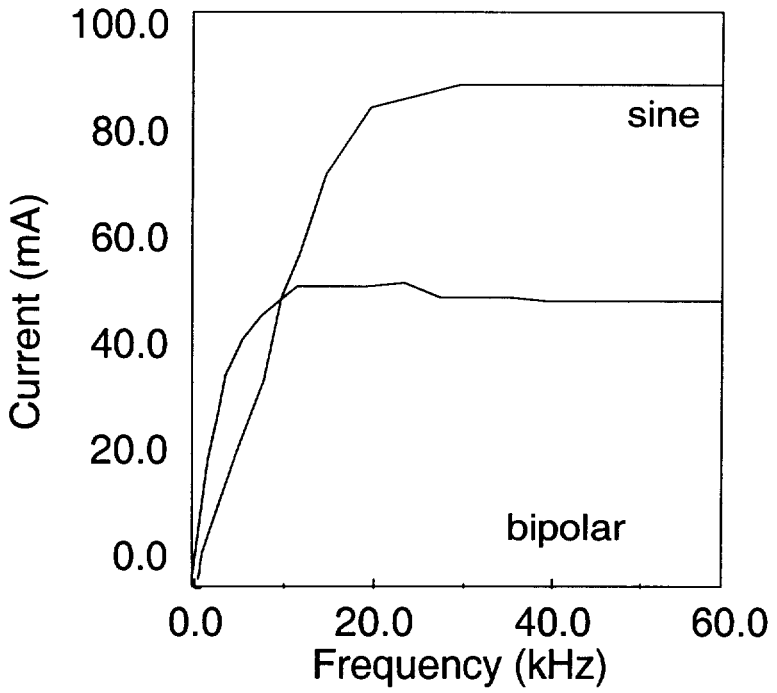

Fig. 4.7 Maximum Current vs. Frequency for SrS:Ce with doping levels of 1:80 at 200 V for the sine and bipolar driving waveforms.

In an effort to understand the observed increase in current maximum with increasing frequency observed for the bipolar driving waveform in Fig. 4.7, the same experiment was performed on a 2 nF capacitor. The results are shown in Fig. 4.8. From the figure it can be observed that although the frequency range is greatly increased, this increase in current is a standard response in any capacitive situation.

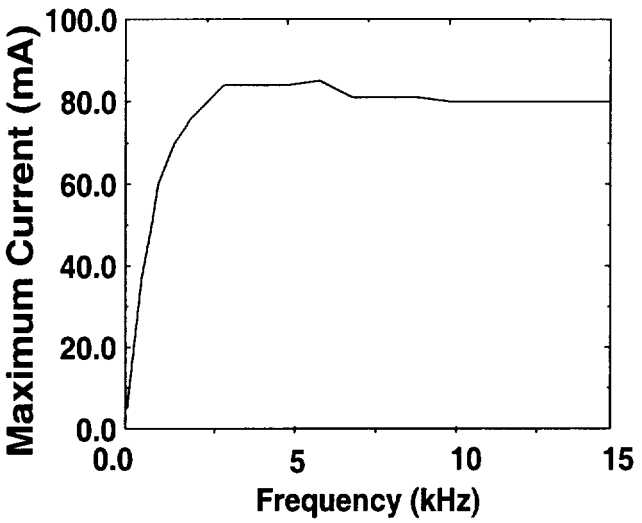

Fig. 4.8 Maximum Current vs. frequency for 2 nF capacitor at 200 V with the bipolar waveform.

Although it is clear that the increase and eventual saturation of the brightness with increasing frequency is at least partially related to the maximum current across the phosphor, it still does not help to explain the eventual decrease in brightness. To determine whether the observed effects with frequency is related to phonon coupling of the dopants or to heating effects at higher frequency, similar brightness and current vs. frequency measurements were performed at 25K with the ZnS:Mn device doped with a Zn/Mn ratio of 1:40. (Here the ZnS:Mn device was chosen for optimal brightness in the test apparatus.) These measurements were accomplished using the ADP Cryostat which allowed for electrical connectivity and visual inspection of the devices while at low temperature. The results are shown in fig 4.9. From the figure it can be seen that the same general effects of frequency still hold. The frequency at which the brightness saturates does not vary greatly with temperature. This implies that the heat generated at high frequency does not significantly affect the brightness and, in this ZnS:Mn case, Mn^{2+} to Mn^{2+} ions are not acoustically coupled.

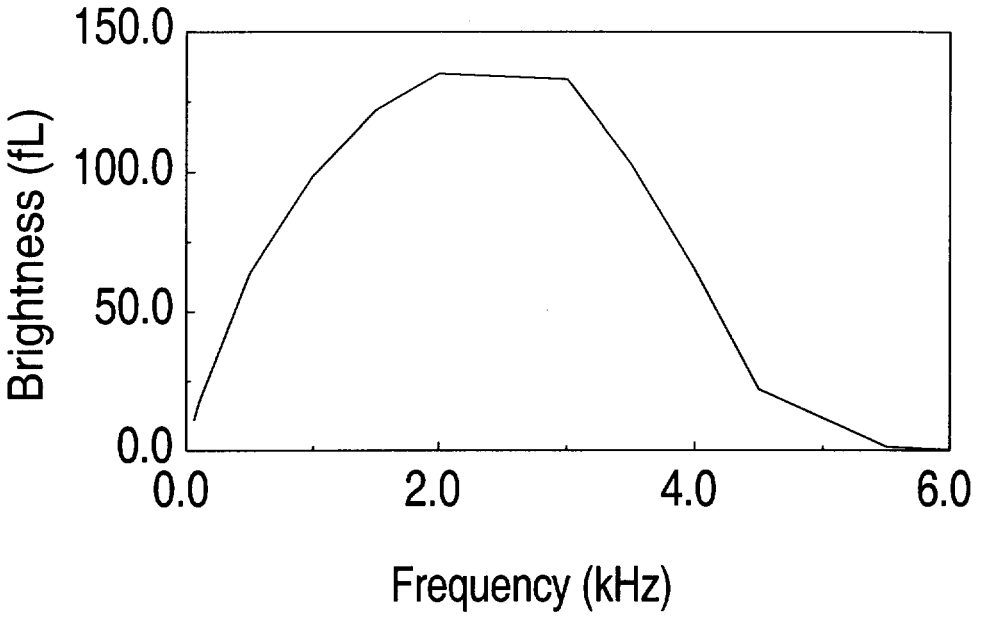

Fig. 4.9 Brightness vs. Frequency for ZnS:Mn doped 1:40 at 200 V with the bipolar driving waveform at 25 °C.

Another explanation for the decrease in brightness again lies in the waveforms themselves. A difference between the sine and sawtooth waveforms and the bipolar waveform is the number of transitions. For the bipolar waveform there are four transitions, one for the rising edge of the positive peak, one for the falling edge of the positive peak, a third for the falling edge of the negative peak, and a fourth for the rising edge of the negative peak. For the sine and sawtooth waveforms, there are only two transitions, one for the rising edge and one for the falling edge. For the latter case the two transitions are a combination of the four in the first case. This difference manifests itself in the amount of time over which a resulting current is observed. At lower frequencies the time over which current exists would be longer than that for the bipolar. As the frequency is increased, though the current magnitude is expected to increase, the time over which the current is present is expected to decrease. It is possible that for very high frequency, though the current magni-

tude for the sine and sawtooth waveforms would be high enough for emission, the time over which that current is available is too small. This may partially explain why the sine and sawtooth waveforms would eventually 'turn off'. It does not help to explain why the bipolar waveform would also 'turn off'. Currently no testing has been performed to verify the expected decrease in time the current is available.

Another possible explanation for the eventual decrease in brightness with increasing frequency may lie in relation to the emission life times. If the devices are driven at a frequency higher than the emission life times, decreased emission may result. In order to test this, the effects of doping level on brightness with changing frequency was analyzed. The brightness from ZnS:Mn devices with varying doping levels was measured over frequency at constant (200 V) voltage with the standard bipolar waveform. The results are show in Fig 4.10. It is clear that as the doping level is increased the frequency range over which it produces efficient emission is decreased. For these devices, the emission life times decreased as the doping levels decreased, ranging from 0.5 microseconds for the 1:40 device to 1.0 microseconds for the 1:200 device. This information tends to discredit the hypothesis. This behavior has also been verified in ZnS:Tb and SrS:Ce devices. Similarly, the emission life times for SrS:Ce devices are significantly larger (approximately 10x) than its ZnS:Mn counter part. This again seems to indicate that the point where brightness begins to decrease is lower for devices with smaller emission life times. It should be noted that in these cases the emission life times are measured as the full-width at half maximum of the observed emission peak. This may not be the measurement procedure as the curves tend to narrow with increased brightness. Although no measurements using the area of the brightness curve have been performed, these may help to shed more light. It is also important to note here that the threshold voltage is not constant with doping. This may affect observed brightness. No measurements have been done to determine how the brightness vs. frequency curves change as the applied voltage is altered. It is

clear, however, that frequency and voltage are not independent variables on the brightness observed. To get a true understanding of how a phosphor will perform 3-D graphical representations of brightness vs. frequency and voltage are recommended. Also no measurements of emission life times for devices driven with sine or sawtooth waveforms have been performed for comparison to the bipolar case. This is recommended for future work.

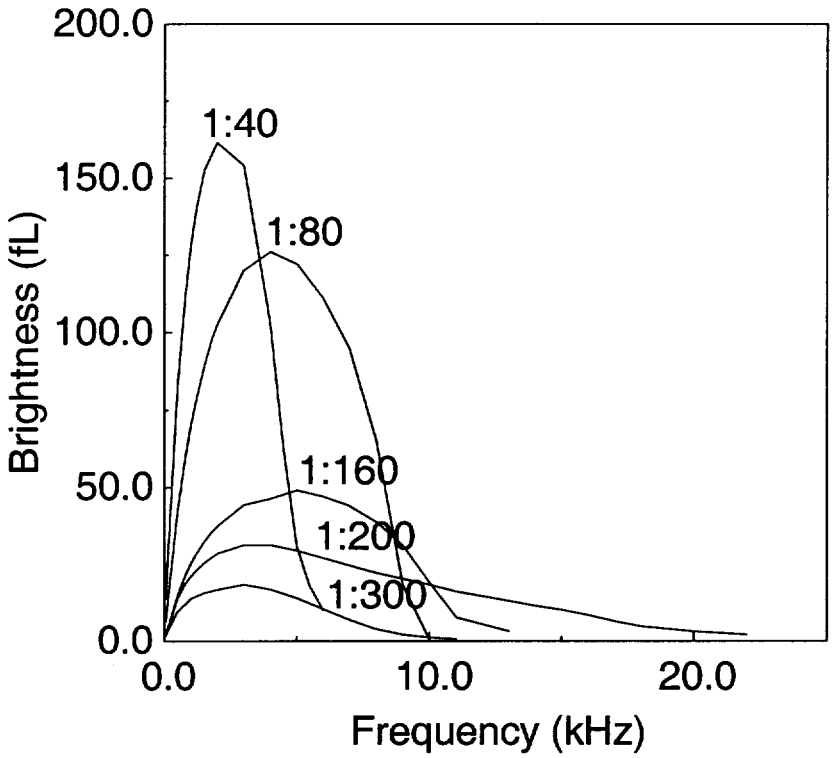

Fig. 4.10 Brightness vs. Frequency for ZnS:Mn with varying doping levels.

From this research it has been demonstrated that the performance of a SrS:Ce device (as well as other TFEL phosphor types) is dependent on more than the driving voltage amplitude. The total achievable brightness is also a variable of phosphor thickness, doping concentration, frequency, and waveform. These dependencies have also been shown to be interdependent. As a result, to produce the highest brightness for a given application, all of these variables must be considered extensively.

4.2 Codoping in SrS:Ce

Historically codoping, or the addition of a second, typically non-emitting, dopant into a TFEL host along with the activator, has shown to have some benefits on the performance of some phosphor materials, including SrS:Ce. In the past codoping was often unavoidable due to limitations of thin film processing technology. Improvements in technology over the years has allowed for a reduction in contamination of thin films. Though many phosphors films have been improved, some 'cleaner' films have shown a decrease in performance.

These decreases in the optical performance of different phosphors due to a reduction in codoping contaminants have been explained with a number of different reasons. Certain codopants can improve a host crystallinity resulting in improved the device efficiency [42]. Other codopants may act as a coactivator for the standard activator [28]; allowing for transfer of energy from the excited codopant to the standard dopant, improving overall luminous efficiency. In the case of the alkaline earth sulfides, and in particular SrS:Ce devices, codoping with an element with large electronegativity may help to further relax the f-f selection rules, or alter emission spectra in other ways [28, 43]. Further, codoping may be instrumental in decreasing the oxidation mismatch between activator and host ions, allowing for greater incorporation of activator in the host [28, 44].

In the case of oxidation mismatch, it has been known that upon formation of a semiconductor film, charged intrinsic stoichiometric defects in the lattice, such as Schottky and Frenkel defects in the form of intersticials and vacancies are readily created. In order to maintain charge neutrality, these defects must be compensated. In addition the charge mismatch of a dopant should be accounted for to optimize doping limitations [44].

In the case of structures like the alkaline earth sulfides, these effects are even stronger due to the strong ionicity of the lattice. In the case of SrS:Ce, when a Ce^{3+} ion is to take the place of an Sr^{2+} site an additional -1 charge is needed on the anion, S, site to neutralize it, or, as is the case with Cl codoping, a +1 charge (Cl^{+}) is added to compensate for the neighboring 3+ charge of the Ce^{3+} ion.

4.2.1 SrS:Ce with Nitrogen and Bismuth Codoping

In an attempt to improve emission spectral quality and overall device brightness from SrS:Ce devices, investigations into the effects of intentional codoping with -3 charged ions (chosen to neutralize the Ce^{3+} ions at the anion site) were performed. Nitrogen and bismuth were chosen for their close size match to S.

Initial attempts to incorporate N^{3-} used gaseous ammonia (NH_3) as the source material. To accomplish the codoping, the standard SrS:Ce growth procedure was followed with nitrogen, provided in the form of gaseous ammonia through ports #6 (see fig 3.5). (Note that this may allow for ammonia contamination of the Sr or Ce sources, which were loaded into ports #4 and #5 respectively, before reaching the substrate, but because gaseous port #3 is necessary for the H_2S source there was no alternative.) Ammonia pulses of 0.88 seconds, followed by an N_2 purge of 0.66 seconds were applied at varying times of the growth cycle, as described in greater detail below. The amount of ammonia flow allowed into the system was controlled by an external needle valve. It is important to note the difficulty inherent in this procedure due to the degradation effects of ammonia on the viton seals of the F-120 ALE reactor. This required constant examination and seal replacement to avoid leaks and related problems. Unfortunately, no suitable replacement for viton in the reactor has been found.

Figures 4.11, 4.12 and 4.13 show the effects of the nitrogen codoping in varying concentrations on the emission spectra, brightness vs. voltage curves, and CIE coordinates of the phosphor emission respectively. All phosphor layers were grown to the standard 0.35 micron thickness with the 1:80 SrS:Ce ratio. Although no firm measurements on the exact amount of nitrogen codoping in these devices was available, it is not believed that the pulsing sequence resulted in true ALE incorporation. For this reason, the amount of pulsing of the ammonia source was varied. From Fig 4.11 (and reflected in Fig 4.13) it can be clearly seen that as the concentration of nitrogen codoping was increased into the phosphor, the overall emission spectra of the device was shifted to the blue. Additionally, it appears that as the nitrogen concentration increased the relative effects of the longer wavelength peak in the typical SrS:Ce spectra seem to decrease. At the same time, as can be seen in Fig 4.12, as the concentration of nitrogen codoping was increased, the overall brightness of the devices decreased. Much of the reduced brightness can be attributed to the eye's response to a shift in emission spectra. The response to the SrS:3N,Ce,3N device is approximately 1.7 less than that of SrS:Ce [45]. Any additional decrease may likely be attributed to an overall decrease in crystalline quality as seen in figure 4.14.

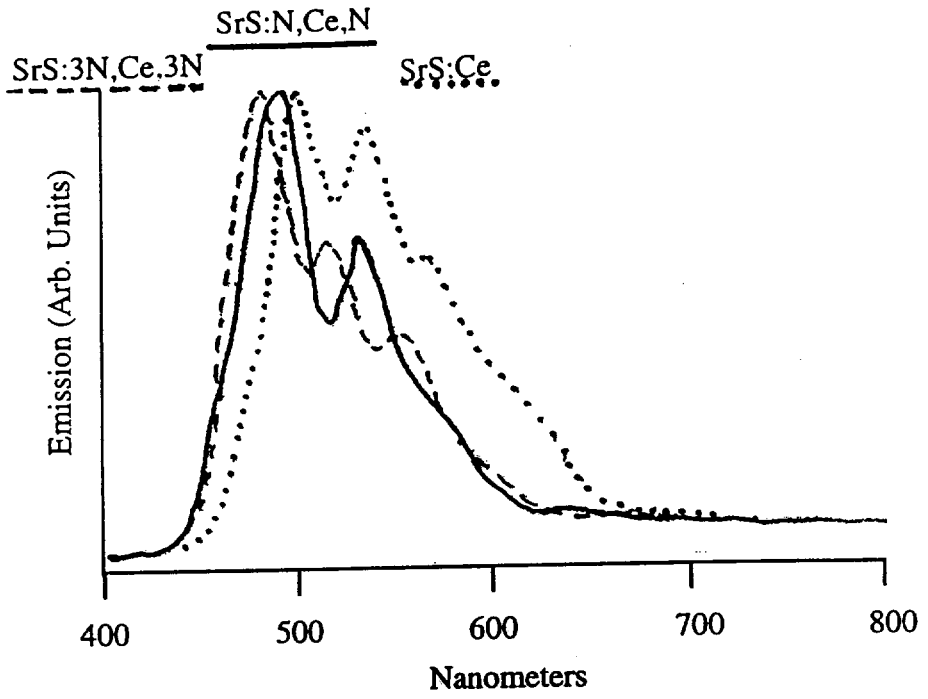

Fig. 4.11 Emission of SrS:Ce with varying concentrations of N codoping.

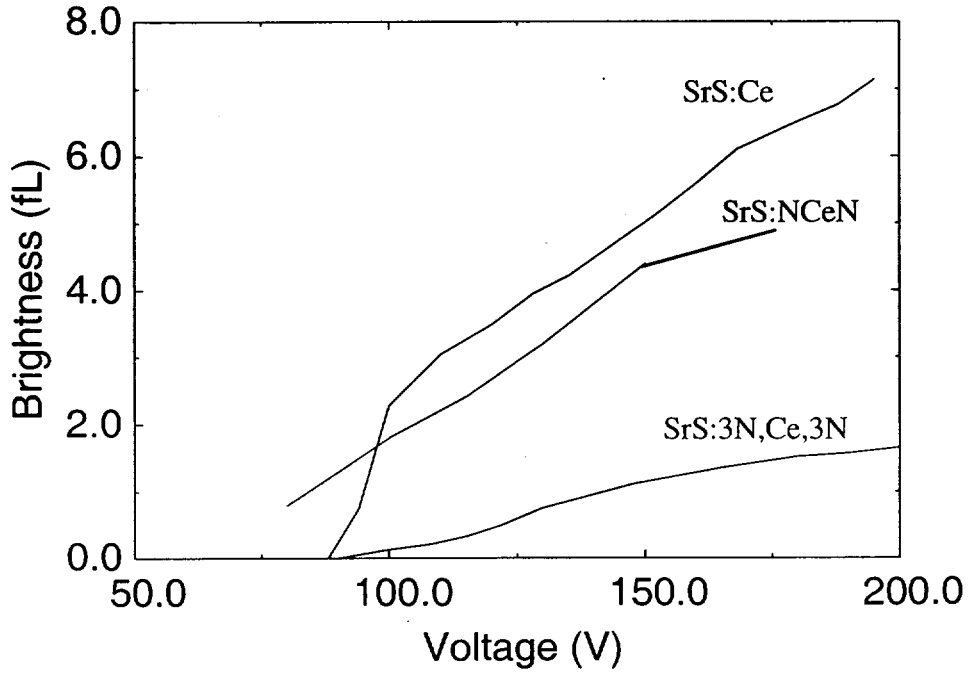

Fig. 4.12 Brightness vs. Voltage of SrS:Ce with varying concentrations of N codoping.

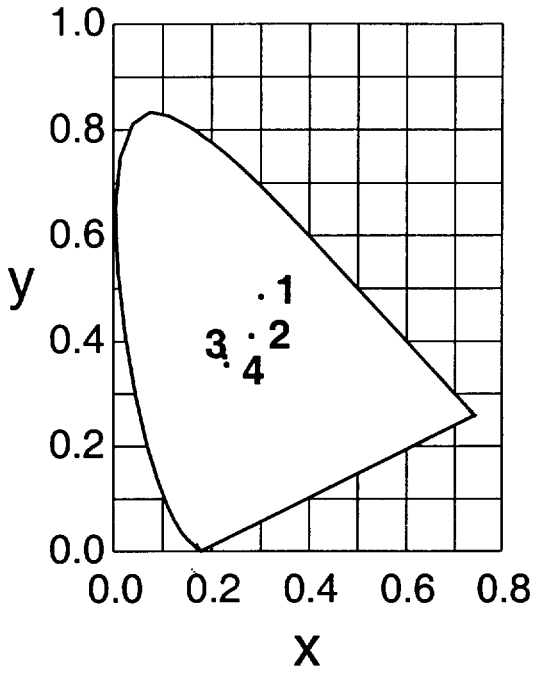

Fig. 4.13 CIE coordinates for SrS:Ce with varying concentrations of N codoping. 1) SrS:Ce 2) SrS:NCeN 3) SrS:3N,Ce,3N 4) SrS:5N,Ce,5N

In an attempt to improve the overall intensity achievable with these devices and to gain insight to the role that crystalline quality plays on the device performance, the rapid thermal anneal (RTA) procedure was performed on a SrS:3N,Ce,3N phosphor. Four sets of identical devices were created. One received no anneal, the others were annealed using the RTA method for 60 seconds at 600 °C, 700 °C and 800 °C respectively in an inert N_2 atmosphere prior to the deposition of the top oxide layer. Fig 4.14 shows the X-ray spectra of SrS:3N,Ce,3N with and without RTA at 800 °C as well as that for SrS:Ce with no codoping. From the figure it can be seen that there are no additional emission peaks created from the inclusion of the ammonia. There is, however, a large reduction in the sharpness of the X-ray peaks, correlating to an overall decreased crystalline quality of the SrS host. This is improved with RTA, though the original quality is not achieved.

Fig 4.15 shows the spectral emission of the SrS:3N,Ce,3N devices with and without RTA for 60 second at 800 ^{o}C. As can be seen there is a red shift associated with the RTA process, perhaps indicating partial elimination of nitrogen from the sample. Slightly smaller shifts were observed for devices with 600 and 700 ^{o}C RTA treatments. Fig. 4.16 and 4.17 show brightness vs. voltage, and CIE emission coordinates, respectively, for the phosphors with an RTA for 60 seconds at 600, 700, and 800^{o}C. From the figures it can be seen that the RTA process did indeed improve the crystalline quality as well as the overall intensity of the phosphor, but again appear to shift the emission closer to the original SrS:Ce with no codoping.

Nitrogen codoping has been shown to be useful in producing a 'truer blue' emission in SrS:Ce devices. Unfortunately, limitations in overall device brightness caused by decreased crystallinity with inclusion of nitrogen through ammonia, appears to be a limiting factor. This may be the partial result of contamination in the film due to left over hydrogen from the ammonia source which may not have been completely removed in the growth process or the result of too much nitrogen incorporation. Currently no alternate nitrogen sources have been found suitable for incorporation with the F-120 ALE reactor. Further work using other source materials, perhaps in an alternate growth environment, may prove more controllable, allowing for a better optimization of amounts and placement of nitrogen within the phosphor.

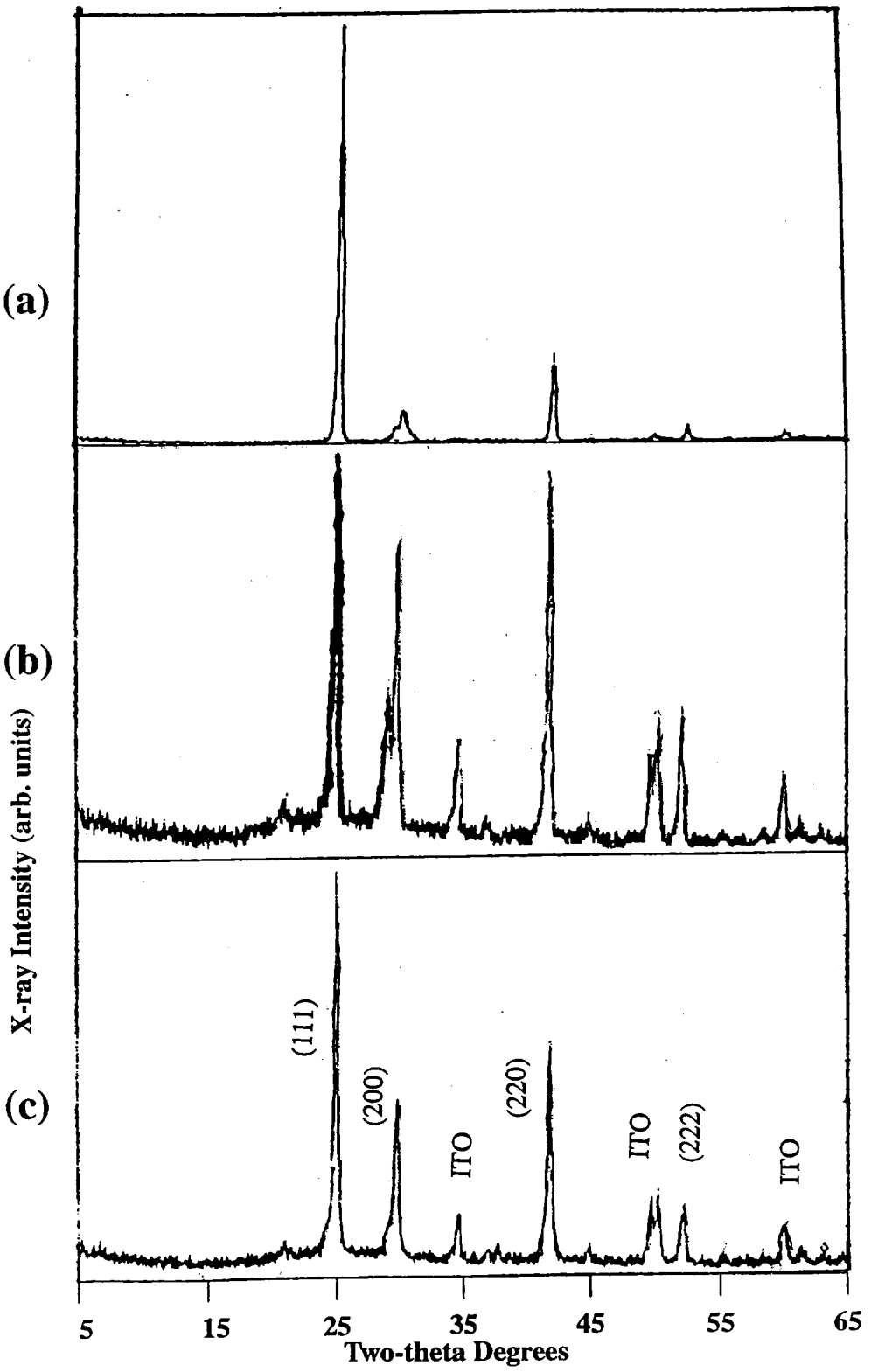

Fig. 4.14 X-ray Diffraction from (a) SrS:Ce (b) SrS:3N,Ce,3N without RTA and (c) SrS:3N,Ce,3N with RTA at 800 °C.

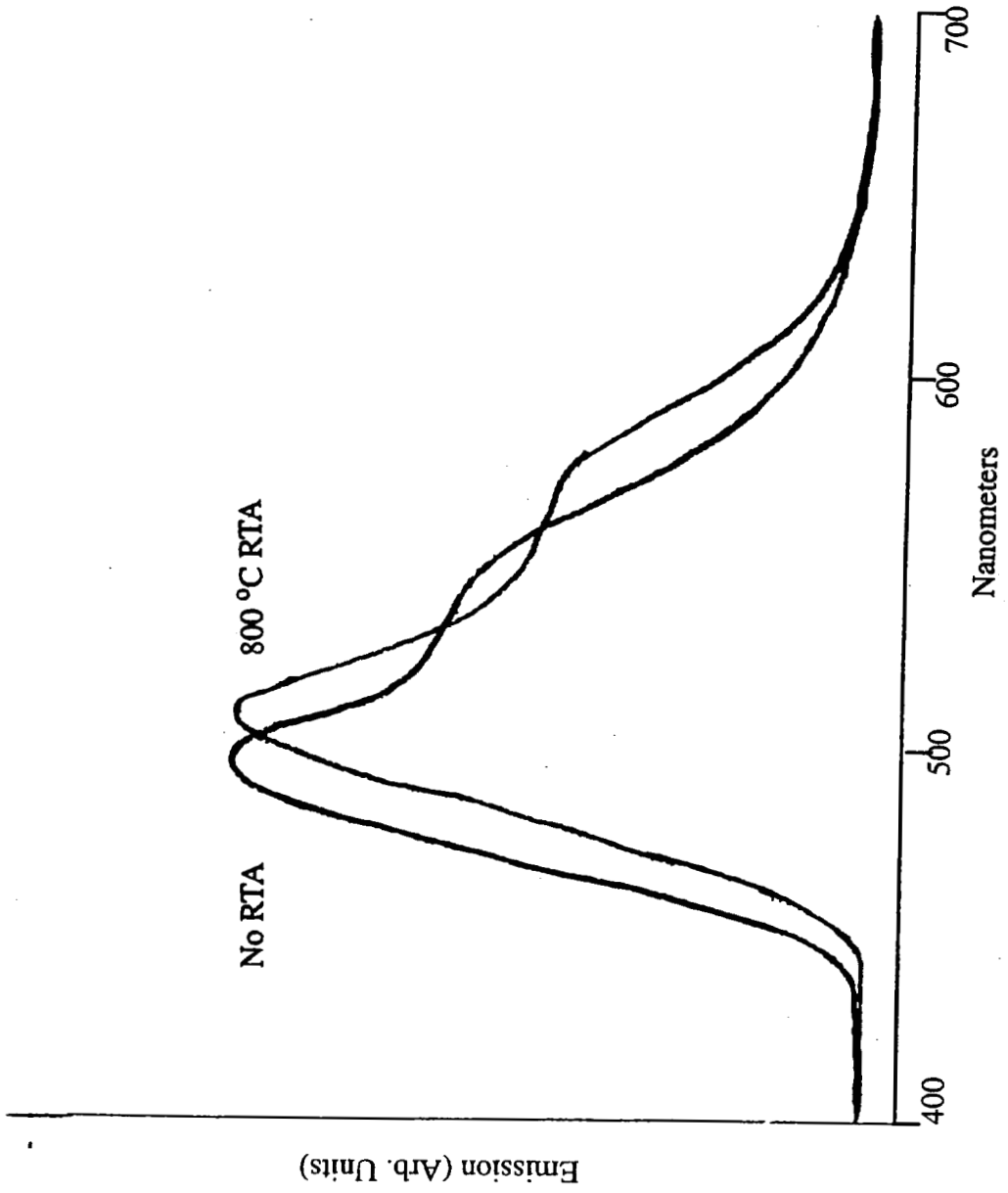

Fig. 4.15 Emission Spectra of SrS:3N,Ce,3N with and without RTA

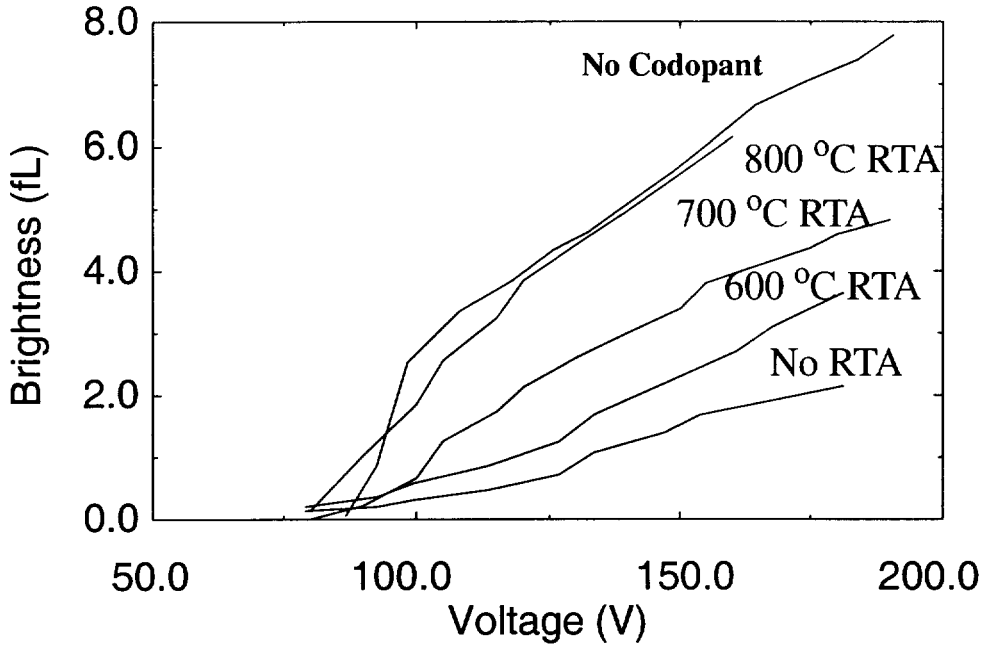

Fig. 4.16 Brightness vs. Voltage for SrS:3N,Ce,3N devices with and without RTA.

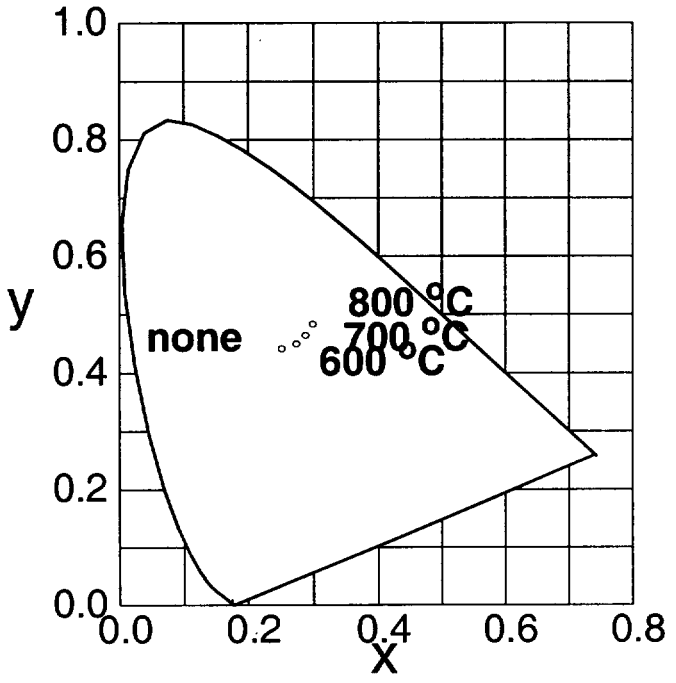

Fig. 4.17 CIE coordinates for SrS:3N,Ce,3N devices with and without RTA

In an attempt to eliminate the potential co-contaminants potentially introduced using ammonia as a nitrogen source and to decrease the erosion effects associated with ammonia on the F-120 ALE reactor, the experiments of the previous section were repeated using Bi^{3-} codoping. Here, bismuth was chosen because it has a very similar structure to nitrogen with a larger atomic radius, appearing directly below nitrogen on the periodic table. Additionally, bismuth can be introduced from solid $Bi(thd)_3$, commercially available through Strem Chemical LTD.

The Bi source was placed in port #1 (reducing the chance of cross contamination with $Sr(thd)_2$ or $Ce(thd)_3$, placed in ports #4 and 5 respectively, prior to reaching the substrate). (See Fig 2.5) An optimal source temperature of 120°C was experimentally determined based on growth of Sr_3Bi_2 films. The results, detailed in Figures 4.18, 4.19 and 4.20 again show the same characteristics observed for the case of nitrogen codoping. Here overall brightness appears to decrease even further than in the case of nitrogen codoping. It should be noted that the bismuth source, which melts below the 120°C point, becomes dark black in color, possibly indicating sulfur contamination in the form of black Bi_2S_3. This has produced blackish phosphor films. This black film color may inhibit the amount of light emitted from the phosphor.

Although both nitrogen and bismuth codoping in SrS:Ce have shown to have the effect of shifting the emission towards the blue spectra, thus far neither has been shown to produce very bright phosphors. Currently the limitations appear to be in the incorporation of the codopants into the phosphor. Better results may be available using alternate growth techniques.

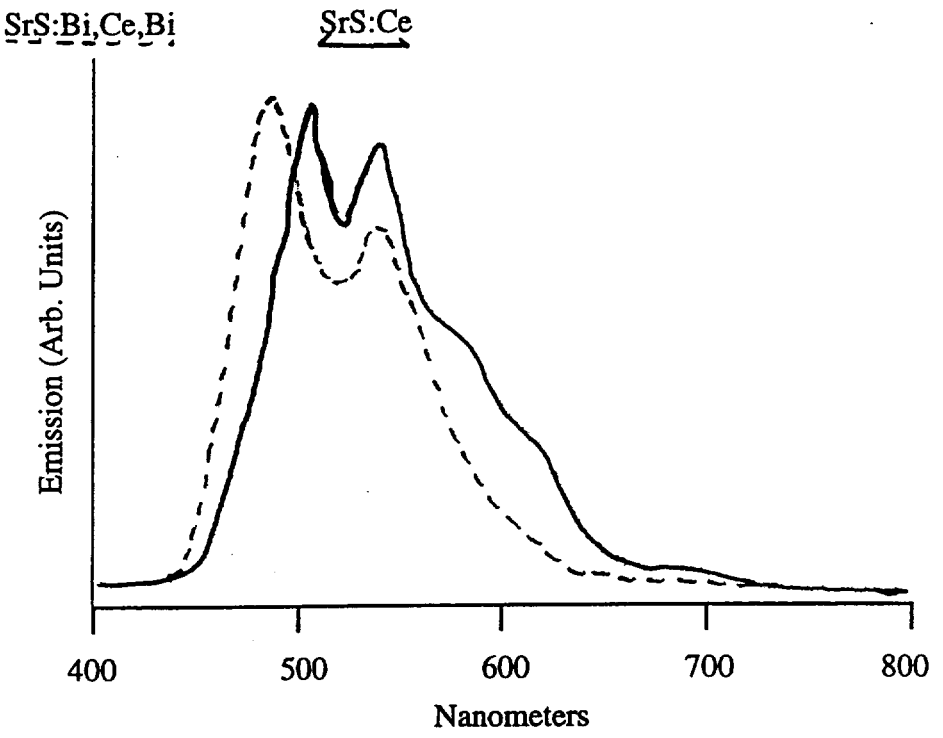

Fig. 4.18 Emission Spectra from SrS:Ce codoped with Bi.

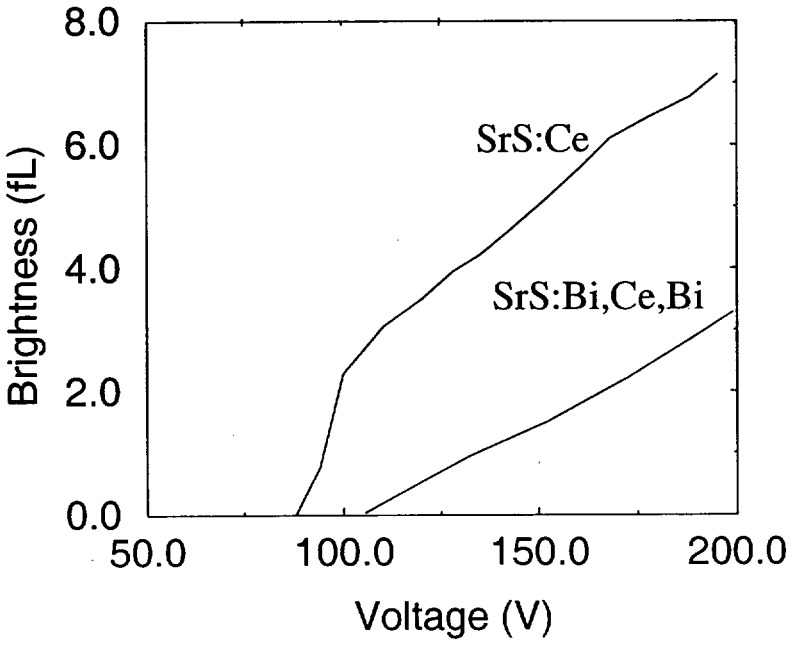

Fig. 4.19 Brightness vs. Voltage for SrS:Ce with Bi codoping.

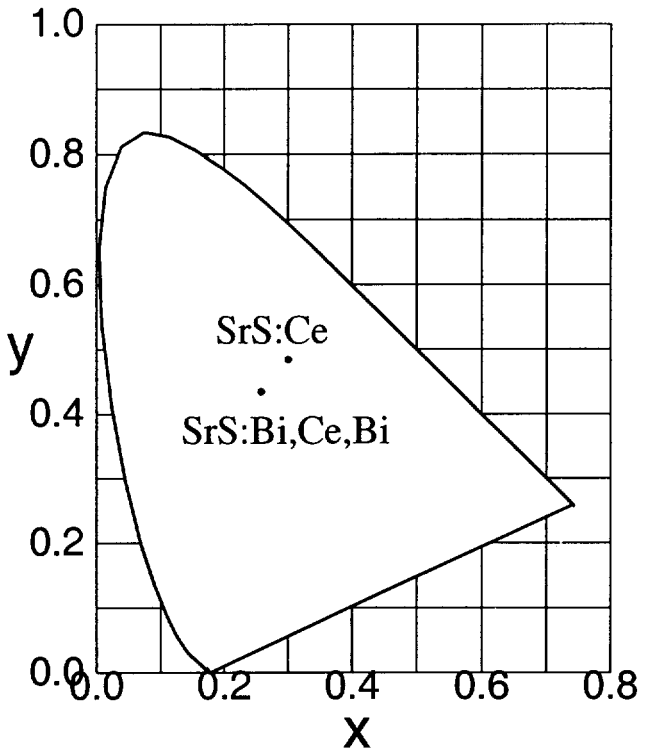

Fig. 4.20 CIE coordinates for SrS:Ce with Bi codoping.

4.2.2 SrS:Ce with Oxygen Codoping

For many years oxygen contamination, typically through interactions with moisture, has been believed to be detrimental to most TFEL device performance. Oxygen contamination has been linked to reduced efficiency as well as a decrease in device shelf lives [28]. In an attempt to gain more insight into this SrS:Ce devices were fabricated with intentional oxygen codoping added through H_2O. Water vapor was supplied to the reactor externally through port #6 (see fig 3.6) for pulse times of 0.88 seconds followed by 0.66 seconds of nitrogen purge both immediately before and after the CeS layer. Again this was performed for the standard 1:80 doping level and 0.35 micron thickness.

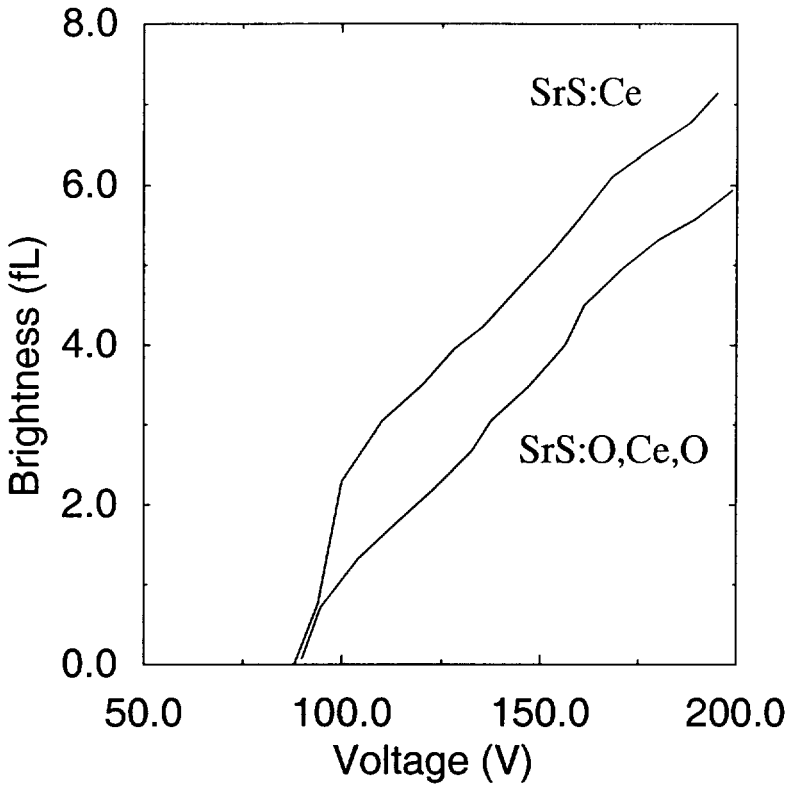

Fig. 4.21 Brightness vs. Voltage for SrS:Ce with and without O codoping.

Surprisingly, there was very little effect observed on the overall emission of the devices with the oxygen codoping. Fig 4.20 shows the brightness vs. voltage for SrS:Ce devices with and without oxygen codoping. From the figure there can only be seen a very slight decrease in brightness for the device with oxygen codoping vs. the device without it. This difference is within the error range for different devices produced under identical run conditions. Although no change was noticeable change in brightness, there was an observed shift towards the blue in the spectrum of the oxygen codoped devices. This is likely due to improved crystallinity at the activator site with the smaller oxygen atoms replacing the sulfur. No studies were done on the overall aging effect the oxygen has on the life spans of the devices.

4.2.3 SrS:Ce with single layer ZnS incorporation

The incorporation of ZnS layers into the typical SrS:Ce phosphor have been linked to improvements in the crystallinity of the phosphor, particularly in and around the Ce site, resulting in improved emission [46, 47, 48]. In an attempt to isolate this phenomenon, the standard SrS:Ce devices were again made, with single layer ZnS codoping placed on either side of the CeS layer (...SrS/ZnS/CeS/ZnS/SrS...). To avoid chlorine contamination, as detailed in section 4.4, the single strand ZnS layers were grown using the $Zn(thd)_2$ procedure detailed in Appendix B. X-ray analysis of the devices showed only slight improvement in crystallinity for the phosphors with ZnS incorporation over standard SrS:Ce phosphors

In this case it was found that the overall achievable brightness of the SrS:Ce devices did not change significantly with ZnS layers, but there was an observed shift towards the blue for these devices. Figures 4.22 and 4.23 show the emission spectra and CIE location for these devices respectively. These results tend to agree with previous work, linking the improvements to relaxation of the lattice field in the vicinity of the activator. No work has been done to optimize the positioning or thickness of the ZnS layers. In this case a significant shift towards the blue spectra with little or no decrease in brightness is achieved. This indicates an improvement of almost twice the overall intensity from the traditional SrS:Ce devices [45]. For this reason, this type of incorporation appears promising. No work has been done at this point to investigate using ZnS layers only on one side of the Ce activator or to re-optimize doping levels in this configuration. Similarly, there has been no work on these structures to determine the effects this structure has on the brightness vs. frequency effects reported earlier.

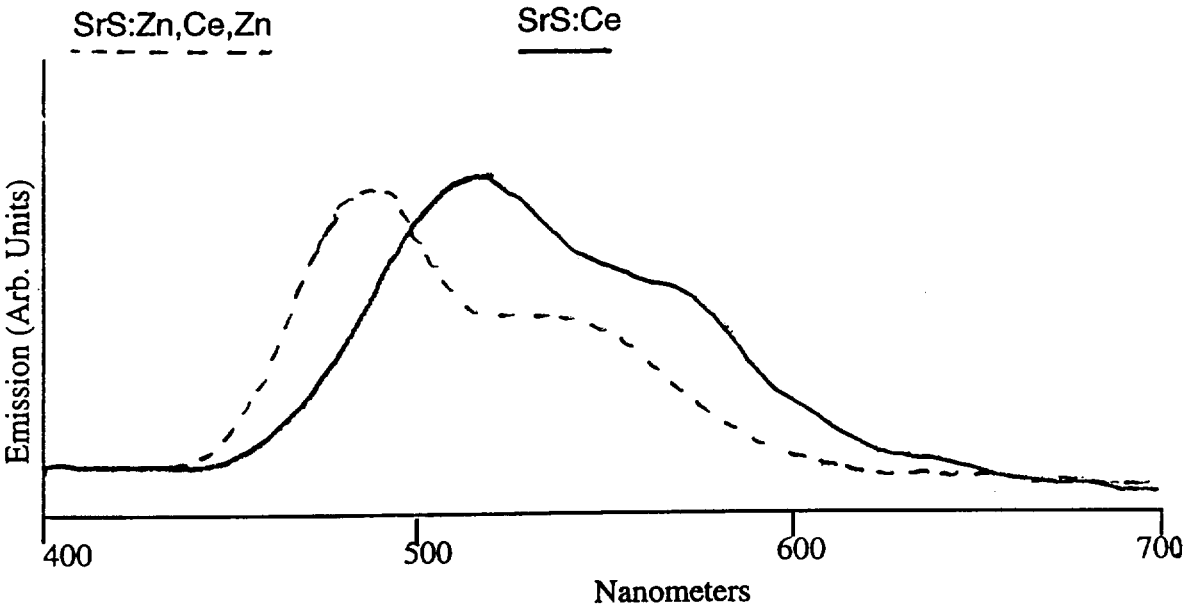

Fig. 4.22 Emission of SrS:Ce with single layer ZnS codoping

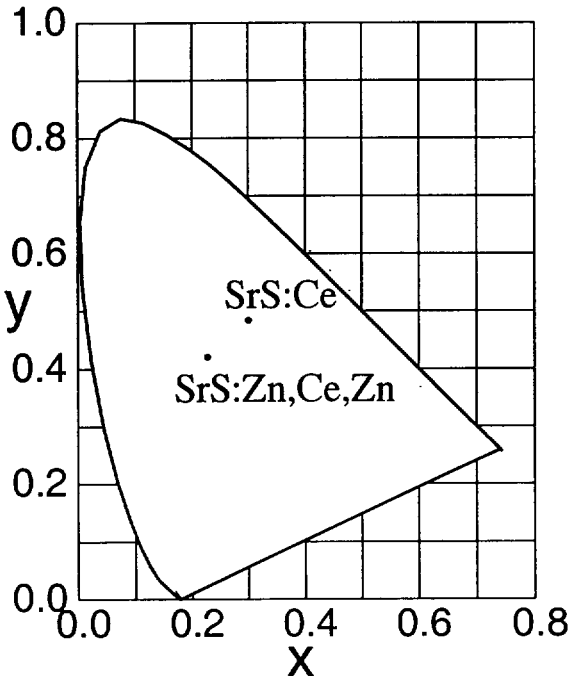

Fig. 4.23 CIE location of SrS:Ce with single layer ZnS codoping

4.3 Blue Emission from Other Activators in SrS Hosts

Tellurium in ZnS and SrS has been long known as a blue photoluminescence emitter [49, 50, 51]. However, attempts at creating blue EL emitters from these materials have failed. Most researchers have pointed to field quenching and impact quenching of the phosphors as the reason for failure [52]. To further investigate Te as a potential blue activator, ZnS:Te and SrS:Te devices were made. A TeCl precursor was initially used to create these devices. The $TeCl_4$ source was heated to 178°C and pulsed for 0.22 seconds followed by a nitrogen purge of 0.66 seconds. This was followed by a pulse of H_2S of 0.88 seconds and a subsequent nitrogen purge of 0.66 seconds. This was doped into both the traditional ZnS (see Appendix B) and SrS hosts (see Appendix A) with a doping concentration of 1:80.

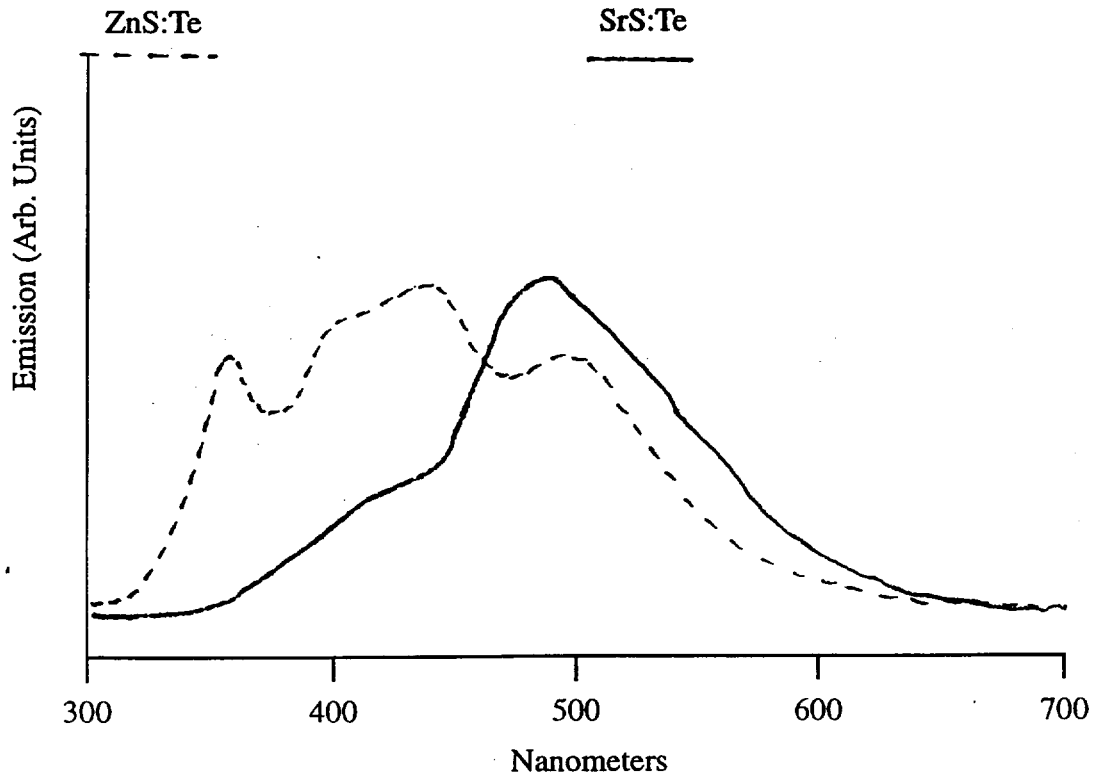

Fig. 4.24 Emission spectra from ZnS:Te and SrS:Te from TeCl precursor.

Surprisingly, blue electroluminescent emission from these devices was detected for both ZnS and SrS host materials. Fig 4.24 shows the emission from these devices. As detailed in section 4.4, chlorine contamination in SrS hosts materials has been shown to produce blue emission from some activators [24]. To eliminate this as the possible source of emission here, another set of SrS:Te devices was created using elemental Te as the source to eliminate any possible chlorine contamination. This source was heated to 310°C and pulsed for 0.77 seconds followed by a 0.66 second nitrogen purge.

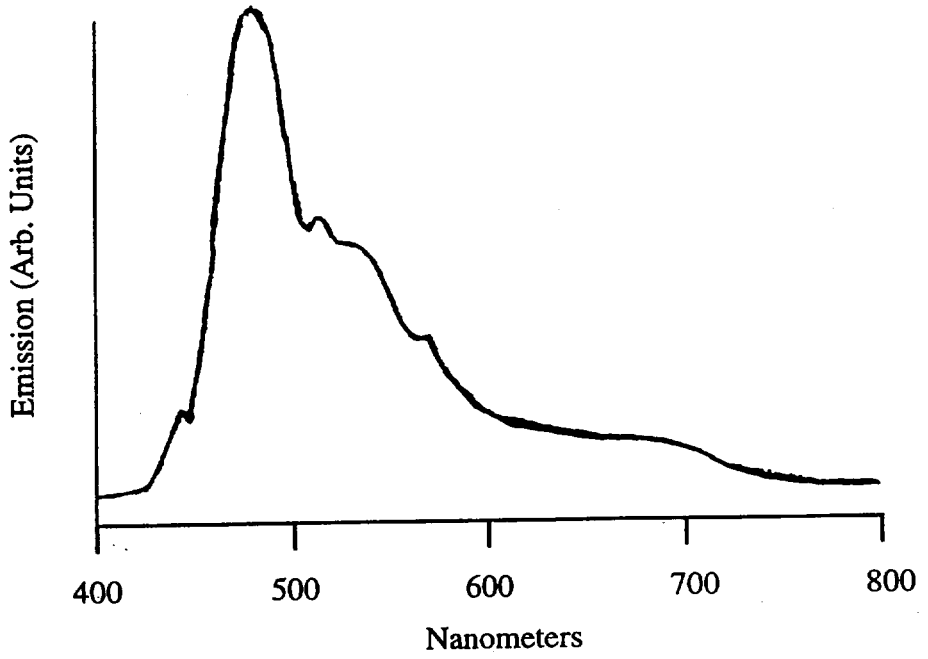

Fig. 4.25 Emission from SrS:Te from elemental Te precursor.

Again, blue emission from SrS:Te was clearly visible, with peak emission at about 475 nm, indicating this as the true source of emission. In this case the emission was significantly brighter than observed in the case phosphor created from $TeCl_4$, perhaps indicating contamination in the latter. Fig 4.25 shows the emission from SrS:Te using the elemental precursor. Fig 4.26 shows the CIE location from this phosphor material. Fig 4.27 shows the brightness vs. voltage for this particular device compared with the standard SrS:Ce device. Clearly from this figure it can be seen that the SrS:Te devices, are actually quite close to the standard SrS:Ce devices in performance. Taking into account the position of the emission from these two phosphors it appears that the overall intensity of SrS:Te is approximately 1.75 that of the SrS:Ce device [45]. It should be noted that further optimization on these devices is still possible. As seen previously, it may be possible to increase the overall achievable brightness of these devices by optimizing the doping level and increasing device thickness. Also, no work has currently been done to characterize these devices with respect to driving frequency or waveform. The ZnS:Te devices are of particular interest. Although no devices of this type have been fabricated using elemental Te, if phosphors of this type can be optimized to the point where its brightness and efficiency are comparable to others currently used in commercial TFEL displays, it would make be an ideal candidate for incorporation with existing red ZnS:Mn and green ZnS:Tb phosphors.

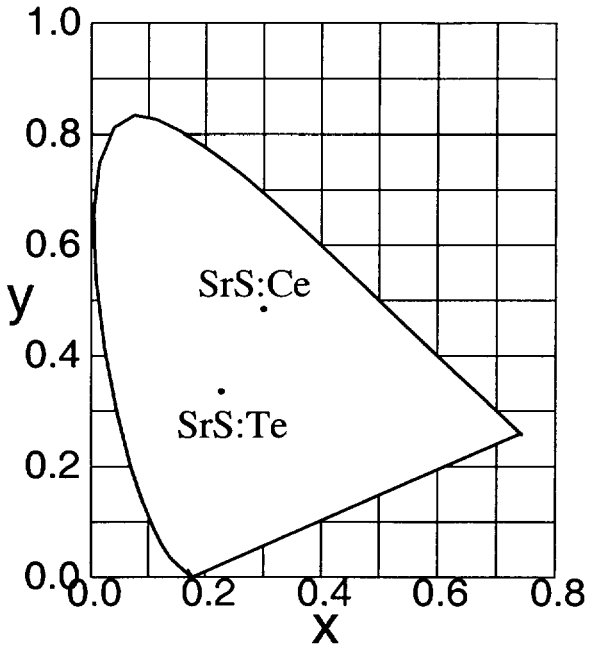

Fig. 4.26 CIE location of SrS:Te EL emission.

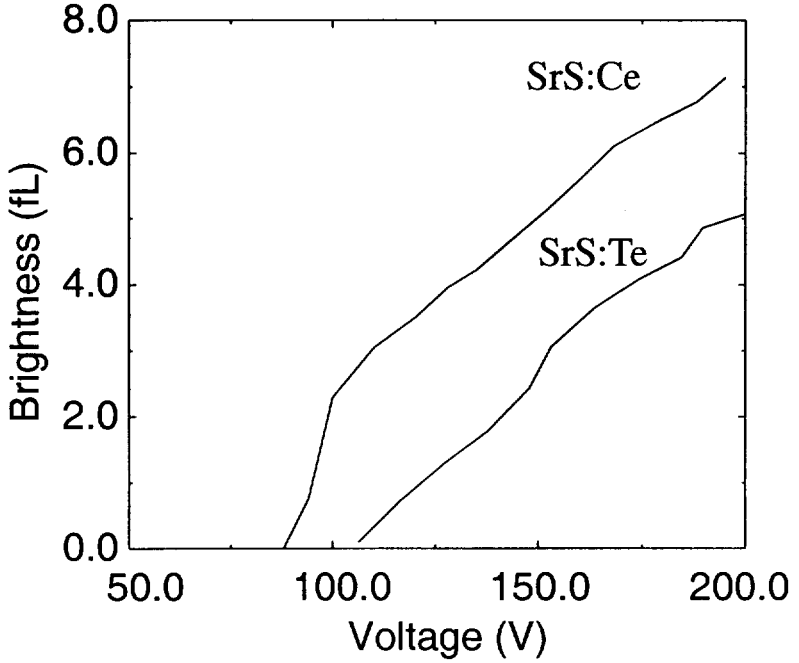

Fig. 4.27 Brightness vs. Voltage for SrS:Te from elemental Te compared with SrS:Ce.

4.4 TFEL Emission from $SrCl_2$ formed in ZnS/SrS Stack

Previous attempts to improve the crystallinity and hence the emission brightness from SrS based phosphors using ZnS stacking layers were carried out using $ZnCl_2$ as the Zn solid source material. Additionally, in this work the back oxide layers were created using $AlCl_3$ as the Al source, as detailed in Appendix C. In this work it was found that when the SrS layers were doped with normally red emitting Eu^{2+}, violet light was emitted [24]. This emission has been linked to emission from the inadvertent creation of $SrCl_2$:Eu phosphors at the ZnS and Al_2O_3 interfaces.

In order to further characterize the $SrCl_2$ phosphor hosts created from the ZnS/SrS stacks, and to find other potential TFEL phosphors which emit in the UV to blue spectra, a number of similar phosphor devices were created using various other RE dopants. These included Ce, Sm, Er, Tb, Ho, and Tm. Fig 4.28 shows the typical emission of these activators in SrS hosts created from EB-deposition [53]. Similarly fig 4.29 shows the emission from the stacked phosphor devices.

It is clear from the figures that Ce and Sm were the only additional activators which appeared to show any significant changes of spectral luminescence in the $SrCl_2$ environment versus that of SrS, each showing emission at about 400 nm. Note that emission from Tm in the stacked structure was too weak to weak to be picked up with the Jarrel-Ash spectrometer. The lack of new emission peaks with the other activators may be explained in many ways. It is quite possible that these activators do not have a radiative transitions in the $SrCl_2$ environment. Another explanation may be the doping concentration. A 1:10 doping level (optimized in the old F-120 reactor configuration) may not be the optimized for each of these activators in the $SrCl_2$ material; if it is too high quenching

may occur in this lattice, and if too low there may not be adequate emission. Attempts to optimize the doping level were largely unsuccessful, due mainly to the inability to control the concentration, thickness, or placements of $SrCl_2$ in the given growth environment. It should be noted that the exact thickness and doping concentrations for the $SrCl_2$ layer are not easily determined in such an uncontrolled growth process.

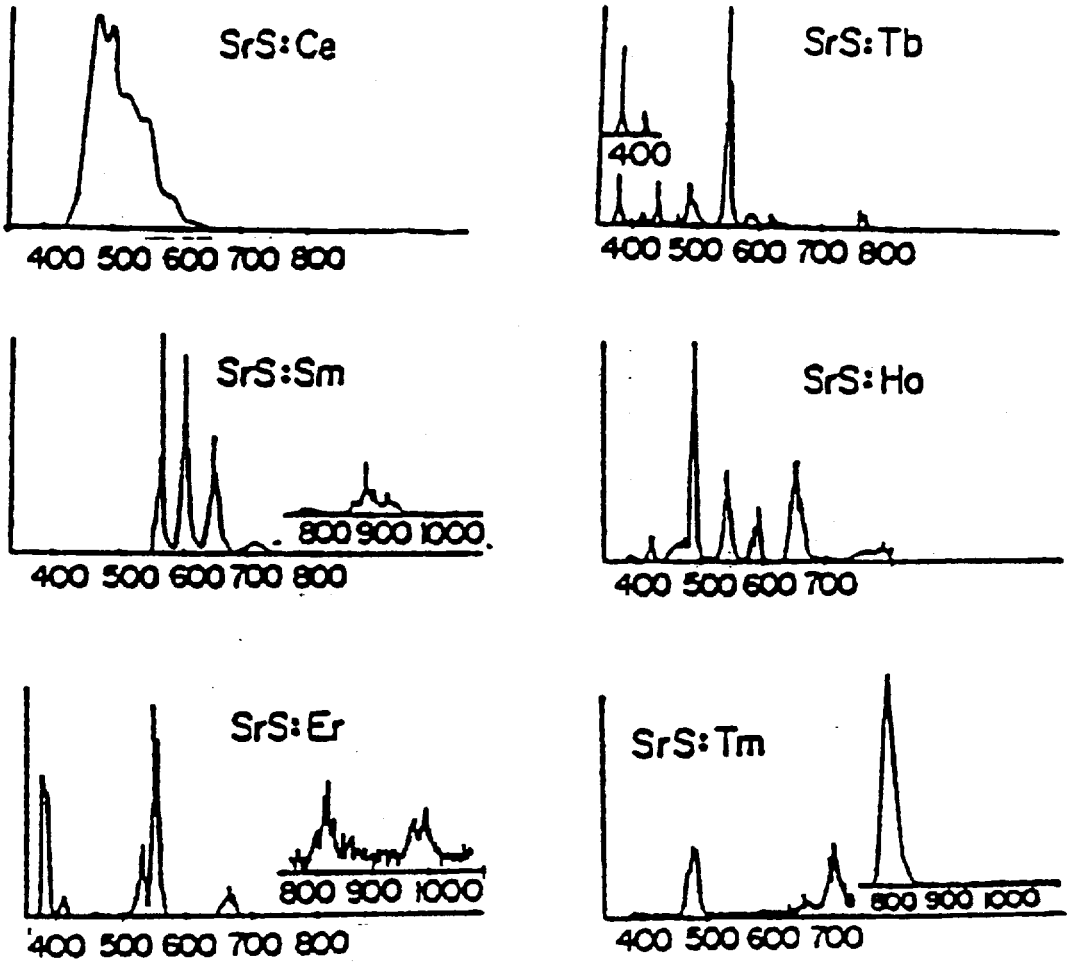

Fig. 4.28 Emission from standard SrS TFEL phosphors with various activators [52].

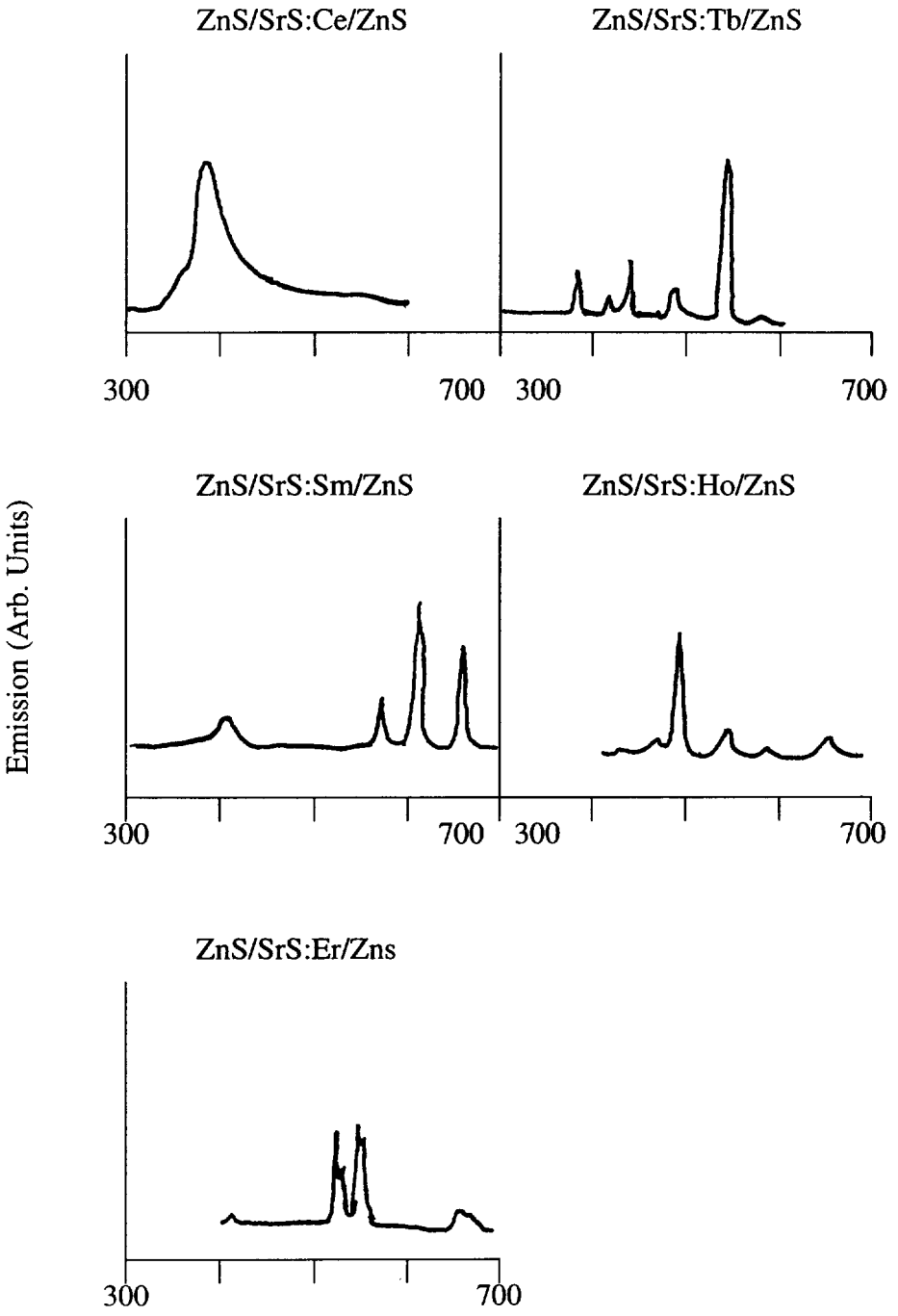

Fig. 4.29 Emission from SrS with ZnS stacking layers with various activators.

$SrCl_2$ host materials have been shown to produce violet-blue emission when doped with Eu, Ce and Sm activators. These phosphor materials, if optimized, show promise as potential blue TFEL phosphors. The $SrCl_2$:Eu emission, in particular, may be an ideal candidate for a blue phosphor because of its CIE location at X=0.17, Y=0.01. Unfortunately, its narrow emission peak [24] and low brightness level limits its use in multi-color display devices. If its overall brightness can be optimized to a much greater point, it may open a wide range of the blue spectrum for TFEL devices. The big hurdle remains the efficient production of $SrCl_2$ thin films which can be easily doped. Currently no suitable chlorine source material has been found for production of this host in the ALE environment. The current techniques are very uncontrolled and often not reproducible. Other deposition techniques such as evaporation or CVD may be more promising for creation of this phosphor type. Once a controllable method of creating the $SrCl_2$ host exists, studies into phosphor optimization can be performed to see whether these phosphor materials can ever reach the luminous efficiency required for TFEL displays.

4.5 Conclusion

In this chapter investigations into techniques available to improve brightness from SrS:Ce devices has been presented. It has been clearly shown that brightness can be optimized for a given current and frequency range by optimizing for phosphor doping concentration and thickness. By making these optimization improvements in observed brightness of an order of magnitude have been observed.

Additionally, investigations presented on the effects that frequency has on the observed device brightness show that significant increases in brightness over the tradi-

tional 60 Hz devices are available by optimizing for driving frequency. This optimization has been shown to depend on driving waveform as well as doping concentration. It has also been shown that the optimization can vary greatly for different phosphor types. This is very important when considering the creation of full color devices made up of different phosphors. From these results it is recommended that devices are created and optimized for the specific frequency range it is intended to be used in. One cannot assume that the relative device performance at low frequency will necessarily carry over to high frequency applications.

Investigations into the chemical and crystalline environment of Ce in the SrS host have been presented including the effects of codoping with nitrogen, bismuth and oxygen as well as the incorporation of single layer ZnS layers in the vicinity of the Ce activators. These investigations have revealed methods available to shift the observed emission spectra of SrS:Ce towards the blue. Presently, the ZnS single layer incorporation method is the only one to show a significant shift in spectral emission without loss of brightness in the current growth environment. The other methods do show some promise should the current growth limitations be overcome.

Finally emission in the blue to violet spectral range was observed from $SrCl_2$ hosts with Ce and Sm as well as from SrS:Te devices. In the first case the uncontrolled growth of the host in the F-120 ALE reactor has been too difficult to achieve bright devices in a reproducible fashion. The Te based devices, however, do appear to show promise as a bright blue phosphor material.

Chapter 5

Quantum Well Activated Phosphors

As has been discussed in detail, traditional (characteristic) TFEL phosphors consist of high band gap semiconducting materials doped with luminescing activator impurity ions. In addition to this, cathodoluminescence (CL) has also been observed from donor/acceptor doped semiconductor (non-characteristic) phosphors. The operating principles of the characteristic phosphors have already been discussed in detail in Chapter 3. It is generally accepted wisdom that the high field in EL applications separates the electrons and holes generated during impact ionization too quickly to allow for radiative recombination via donors/acceptors to occur, thus non-characteristic phosphors exhibit low EL efficiencies.

In this chapter a new class of phosphor, consisting of deep quantum wells (QWs) embedded in high band gap materials, is presented [54]. As will be discussed in greater detail, the embedded quantum wells in this phosphor effectively trap electrons and holes for subsequent recombination, thus acting as efficient radiative recombination centers. As such, the multi-quantum well (MQW) system can be considered a hybrid between non-characteristic and characteristic phosphors. This chapter will detail the theory behind emission from these devices, present the inherent advantages of such a system, present initial results of grown MQW devices, and lastly discuss the limitations and further work required in this field.

5.1 Theory of MQW Device Emission

Fig. 5.1 illustrates the operating principles involved in the emission from MQW devices. As is the case with conventional TFEL devices, the electron source is believed to be from trap sites in the oxide interface [55]. These electrons are then transported under the force of the field to the site of the quantum well (1). Given sufficient well depth, electrons, upon falling into the well (2), may release sufficient energy to allow for electron - hole pairs to be generated across the bandgap of the quantum well material (3). These electron - hole pairs can then be trapped in the energy bands of the quantum well; and may later recombine radiatively (4). Unlike conventional TFEL devices which require a high electric field in order to accelerate the electrons to a high level in order to impart enough energy for impact ionization or excitation, MQW devices rely on the energy from the fall of the electron into the well. As a result MQW devices should exhibit low threshold voltages. Furthermore, because the emission from MQW devices is governed by the quantum levels in the well, it should be possible to engineer the emission characteristics of MQW devices based exclusively on the choice of host and well materials.

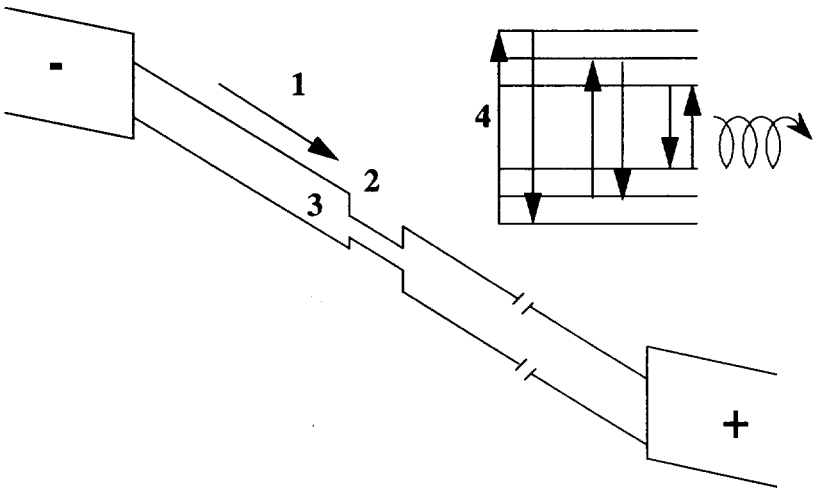

Fig. 5.1 MQW Device Band Model

5.2 Modeling of Emission from Deep MQW Devices

In order to properly determine the emission from a particular MQW device, one must be able to identify the locations of the quantum levels in both the conduction and valence band wells. The MQW emission energy can then be determined as the sum of the well material bandwidth plus the energy from the particular conduction well quantum level to the bottom of the conduction well plus the energy from the corresponding valence well quantum level to the top of the valence well. In general, the recombination from such structures is only expected from parity allowed transitions, meaning transitions between the same quantum states from conduction band well to the valence band well. For the purposes of this work, devices were modeled using the finite well solution to Schroedinger's time-independent equation [56] to model the quantum level location of all the levels in both the conduction band well and valence band well. This procedure is detailed below.

$$X_n \cot X_n = \left(-\left(\frac{m_A}{m_B}\right)\right)\sqrt{2m_A V_o\left(\frac{L}{\hbar}\right)^2 - X_n^2} \qquad \text{Eq. 5.1}$$

$$X_n \tan X_n = \left(\frac{m_A}{m_B}\right)\sqrt{2m_A V_o\left(\frac{L}{\hbar}\right)^2 - X_n^2} \qquad \text{Eq. 5.2}$$

Where X_n is defined as the following:

$$X_n = \frac{L}{2}\sqrt{2m_A E_n} \qquad \text{Eq. 5.3}$$

Here, E_n represents the quantum energy level in the well, h is Plank's constant, m_A and m_B are the effective masses of the particles in the well material and host material respectively (electron for conduction band well, hole for valence band well), L is the width of the well, and V_0 is the depth of the particular well.

These equations represent only the simplest modeling of the MQW devices. To further model the true position of the quantum levels, and hence the final emission of the devices, one should also consider such variables as the applied field. The method of perturbations [57, 58] has been successfully used to estimate the change in the location of the first quantum level in similar quantum well structures [59]. It should be noted that for simplicity of calculation only the bound states are considered for the case of perturbations, and the tunneling of carriers out of a well are not considered.

For the MQW devices described, the perturbation is simply the increase in potential due to the additional field applied across the device. The total field across the phosphor is the total voltage across the MQW phosphor divided by the phosphor thickness.

$$H = \frac{(eV_{phos}z)}{t_{phos}} \qquad \text{Eq. 5.4}$$

Where the total voltage across the MQW device is given by the following:

$$V_{tot} = V_{top} + V_{phos} + V_{bot} \qquad \text{Eq. 5.5}$$

$$C_{top}V_{top} = C_{phos}V_{phos} = C_{bot}V_{bot} \qquad \text{Eq. 5.6}$$

Here V_{tot} is the voltage across the entire device; V_{top} and C_{top} are the voltage and capacitance of the top oxide, V_{bot} and C_{bot} are the voltage and capacitance of the bottom voltage, V_{phos} and C_{phos} are the voltage and capacitance of the phosphor layer, t_{phos} is the thickness of the phosphor layer, and e is the particle charge. Solving for V_{phos} in terms of V_{tot} and the individual capacitances of the top and bottom oxides as well as the capacitance of the total phosphor layer and substituting the thicknesses and permittivities constants in place of the total capacitances, the voltage across the phosphor is determined below.

$$V_{phos} = V_{tot}\frac{\left(\frac{t_{phos}}{\varepsilon_{phos}}\right)}{\left[\left(\frac{t_{top}}{\varepsilon_{top}}\right)+\left(\frac{t_{phos}}{\varepsilon_{phos}}\right)+\left(\frac{t_{bot}}{\varepsilon_{bot}}\right)\right]} \qquad \text{Eq. 5.7}$$

Plugging back into Eq. 5.4 one obtains the perturbation to the well potential. From this the perturbation Hamiltonian can be defined using the time-independant Schroedinger's Equation [57, 59]:

$$H_{nm} = \frac{eV_{tot}}{(\varepsilon_{phos})}\frac{Z_{nm}}{\left[\left(\frac{t_{top}}{\varepsilon_{top}}\right)+\left(\frac{t_{phos}}{\varepsilon_{phos}}\right)+\left(\frac{t_{bot}}{\varepsilon_{bot}}\right)\right]} \qquad \text{Eq. 5.8}$$

Where Z_{nm} is the normalization of the distance, z.defined below using standard normalization methods.

$$:Z_{nn} = \frac{-B_n^2(k_2(n)L+1)}{2k_2^2(n)} \qquad \text{n=m} \qquad \text{Eq. 5.9}$$

$$Z_{nm} = \frac{-2B_nB_m\left((k_2(n)+k_2(m))\frac{L}{2}+1\right)}{[k_2(n)+k_2(m)]^2} \qquad \text{n, m even or n, m odd} \qquad \text{Eq. 5.10}$$

$$Z_{nm} = -2B_nB_m\left(\frac{(k_2(n)+k_2(m))\frac{L}{2}+1}{(k_2(n)+k_2(m))^2}\right) + A_nA_m[A^1+A^2+A^3+A^4] \qquad \text{Eq. 5.11}$$

n even, m odd or n odd, m even

Here the terms numerical simplifiers, A^1, A^2, A^3, and A^4 are defined below.

$$A^1 = \frac{\sin(k_1(n)-k_1(m))\frac{L}{2}}{(k_1(n)-k_1(m))^2} \qquad \text{Eq. 5.12a}$$

$$A^2 = \frac{\sin(k_1(n)+k_1(m))\frac{L}{2}}{(k_1(n)+k_1(m))^2} \qquad \text{Eq. 5.12b}$$

$$A^3 = -\frac{\frac{L}{2}\cos\left[(k_1(n)-k_1(m))\frac{L}{2}\right]}{(k_1(n)-k_1(m))} \qquad \text{Eq. 5.12c}$$

$$A^4 = -\frac{\frac{L}{2}\cos\left[(k_1(n)+k_1(m))\frac{L}{2}\right]}{(k_1(n)+k_1(m))} \qquad \text{Eq. 5.12d}$$

Here k_1 and k_2 are defined below.

$$k_1(n) = \frac{2X_n}{L} \qquad \text{Eq. 5.13}$$

$$k_2(n) = \sqrt{\left[\frac{2m_B V_o}{h^2} - \frac{m_B}{m_A}k_1^2(n)\right]} \qquad \text{Eq. 5.14}$$

A_n is the normalization coefficient inside the well material; and B_n is the normalization coefficient outside the well.

$$A_n = \frac{1}{\sqrt{\left[\frac{L}{2} + \frac{\sin(k_1(n)L)}{2k_1(n)} + \frac{\left(\cos\left(k_1(n)\frac{L}{2}\right)\right)^2}{k_2(n)}\right]}} \qquad \text{n odd} \qquad \text{Eq. 5.15}$$

$$A_n = \frac{1}{\sqrt{\left[\frac{L}{2} - \frac{\sin(k_1(n)L)}{2k_1(n)} + \frac{\left(\sin\left(k_1(n)\frac{L}{2}\right)\right)^2}{k_2(n)}\right]}} \qquad \text{n even} \qquad \text{Eq. 5.16}$$

$$B_n = A_n\cos\left(k_1(n)\frac{L}{2}\right) \qquad \text{n odd} \qquad \text{Eq. 5.17}$$

$$B_n = A_n\sin\left(k_1(n)\frac{L}{2}\right) \qquad \text{n even} \qquad \text{Eq. 5.18}$$

From this the final change in the quantum energy levels can be defined below:

$$\Delta E_n = H_{nn} - \sum_{m \neq n} \frac{|H_{nm}|^2}{E_{om} - E_{0n}} \qquad \text{Eq. 5.19}$$

Here E_{0n} is the calculated value for the n^{th} energy level from the finite well method. It should be noted that this approximation does not take into account the polarization field from trapped drive electrons.

From this model it appears possible that by properly selecting the choice of quantum well material, host material, number of wells, thickness of the well and host materials, and applied voltage, it should be possible to engineer luminescent devices. Further, it may be possible to choose these parameters in such a way as to determine the spectral emission. It is expected that as the applied voltage to the device is increased the energy levels will come down in the conduction well and rise in the valence well, causing a red shift in emission. It is also expected that higher energy levels may be observed in the emission as more electron - hole pairs will be created. The following chapter will apply these fundamental equations to model the emission from actual MQW devices.

Chapter 6

Emission from Multi-Quantum Well Devices

In order to test the theories presented previously in Chapter 5, it is necessary to create and characterize such multi-quantum well (MQW) devices. As eluded to previously there are a number of parameters which must be considered when determining proper materials in the growth of MQW devices. In order to establish a proper quantum well, the host and well materials must be chosen such that there is an adequate phase matching to help ensure a consistent crystalline environment. The off-set of the conduction and valence bands from the host material to the well material must be such that upon the moving of an electron into a well, there will be sufficient heating to allow for the creation of electron-hole pairs in the well material trapped in the quantum wells. Additionally, the energy difference from conduction band well to valence band well should be chosen such that emission given off from the recombination of the electron - hole pairs will produce emission in the visible spectrum. In addition to these requirements the host should be one in which sufficient tunneling (or injection) from the oxide interfaces in the standard ACTFEL structure is achievable to produce the necessary electrons to provide the required energy upon falling into the wells. Lastly, the ability to grow both the well and host materials in an environment suitable for MWQ device fabrication must be considered.

In this work all MQW devices created were grown using the ALE technique as described previously in Chapter 2. As was the case with all standard ACTFEL devices, the devices were grown on substrates consisting of glass, ITO (used as the front contact) and ATO (used as the front insulator layer) provided by Planar America. Again, the back insu-

lator layer was Al_2O_3 created using the aluminum-isopropoxide source ALE method as detailed in Appendix C. Sputtered aluminum spots were used for the back contacts.

6.1 CdSe Wells in an SrS Host

The first MQW devices created consisted of CdSe wells embedded in an SrS host. This particular combination was chosen not only because of the good lattice match between rocksalt SrS (0.6019 nm) and zinc blende CdSe (0.6052 nm) [61, 62] and the large band off-set between the two, as shown in Fig 6.1 [63], but also because of the considerable knowledge already established in the growth of SrS in an ALE environment. Note that the well levels in Fig 6.1 are not drawn to scale and are for illustrative purposes only.

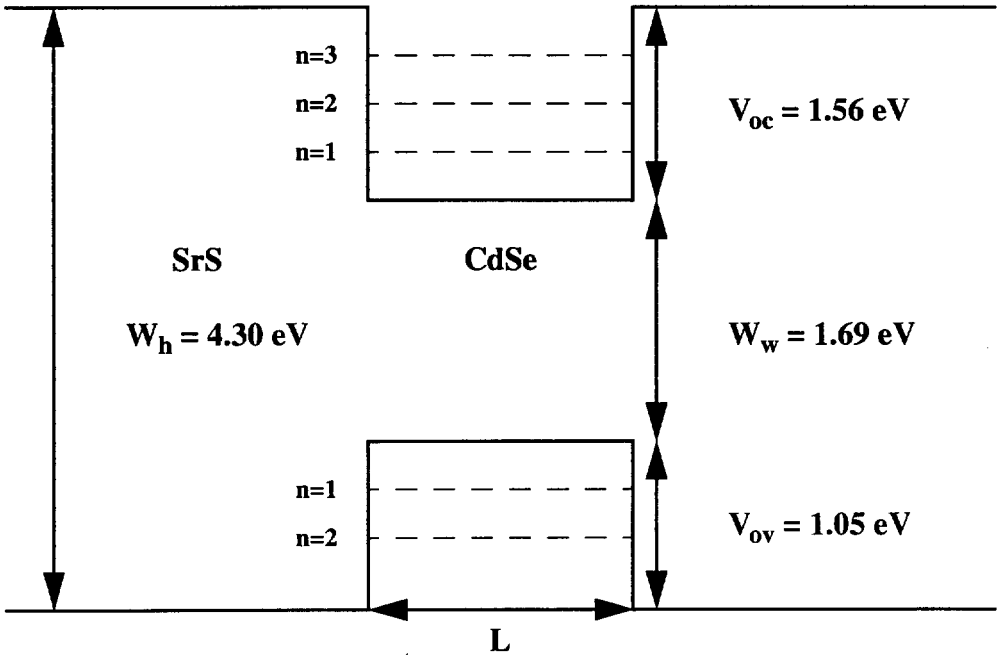

Fig. 6.1 Band Offset of CdSe Wells in SrS Host

6.1.1 Growth of SrS/CdSe MQW Devices

For purposes of investigation MQW devices were grown via ALE using standard ITO/ATO substrates. SrS layers were grown using the standard growth procedures described in Appendix A with sublimated $Sr(thd)_2$ source material provided from Planar America. Growth of CdSe via ALE proved to be more difficult. CdSe films were grown using elemental sources for both Cd and Se. For device growth efficiency, the substrate temperature of SrS (380° C) was kept constant during the CdSe growth period, in order to easily create the SrS/CdSe MQW devices. Source temperatures of 280° C for elemental Se and 340° C for Cd were optimized for film uniformity across the device from reported parameters for ALE and MBE growth of CdSe on GaAs [64, 65, 66]. Pulse times of 0.33 and 0.22 seconds for Cd and Se sources respectively were found to be optimal for CdSe growth. Both were followed by a 0.66 second pulse of dry nitrogen.

Using a CdSe film grown under these conditions for 2000 cycles on a standard ITO/ATO substrate with a 200 nm SrS layer, the growth rate of CdSe was found to be 0.20 per cycle with a deviation of 5% in the vertical (perpendicular to flow) direction and 15% in the horizontal (parallel to flow) direction. Unfortunately, accurate measurements of such films proved to be very difficult. Because CdSe films are opaque, profilometry, which has proven far less accurate than ellipsometry measurements, was the only method available for calculating film thicknesses. In addition, suitable etchants to create the necessary CdSe mesa needed for profilometry were difficult to find that did not also etch the SrS underlying layer. By contrast, growth of CdSe on bare glass was found to be 0.45 nm per cycle. It should also be noted that the large growth rate seems to imply that this is not an ideal ALE reaction and may actually be a CVD type reaction. As a result the calculated growth rate for CdSe on SrS may not be a constant with the number of cycles grown.

To further illustrate the role of substrate on the growth of CdSe layers, Fig 6.2 shows the X-ray analysis for CdSe films grown on bare glass and SrS substrates. As can be seen the crystalline make up of the final CdSe film is highly dependent upon the substrate crystallinity. It is important to point out that the CdSe film grown on SrS indicates the presence of hexagonal phase CdSe; whereas there are clearly no hexagonal peaks for the growth on glass substrates. Note that many of the observed peaks may represent either cubic or hexagonal phase CdSe. As a result it is not clear whether the anticipated cubic phase is truly dominant.

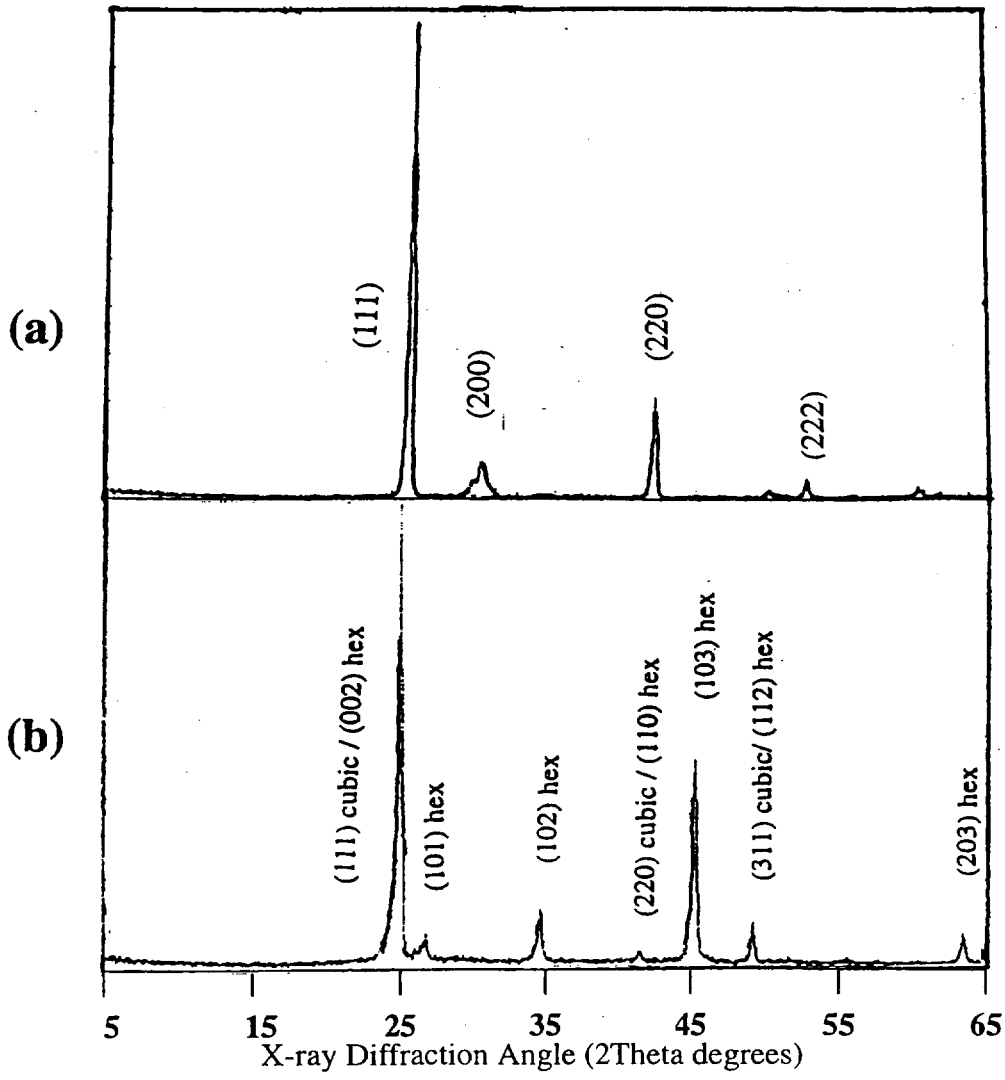

Fig. 6.2 X-ray diffraction of CdSe film grown on a) bare glass and b) SrS substrates.

Using the same growth conditions described earlier for SrS and CdSe, six sets of SrS/CdSe MQW devices were created, each consisting of 10 CdSe wells of constant thickness. The thickness of the wells was changed from device to device; well thicknesses of 15, 10, 8, 5, 3, and 1 nm were selected for the various sets. (A growth rate of 0.2 nm per cycle as calculated previously was used to estimate well thickness.) The thickness of the separating SrS host layers was 60 nm for the 15 and 10 nm well devices and 40 nm for the narrower well devices. (These thicknesses were chosen to be large enough to be able to ignore the effects of neighboring wells in modeling. The 40 nm thickness was later used for ease of fabrication.)

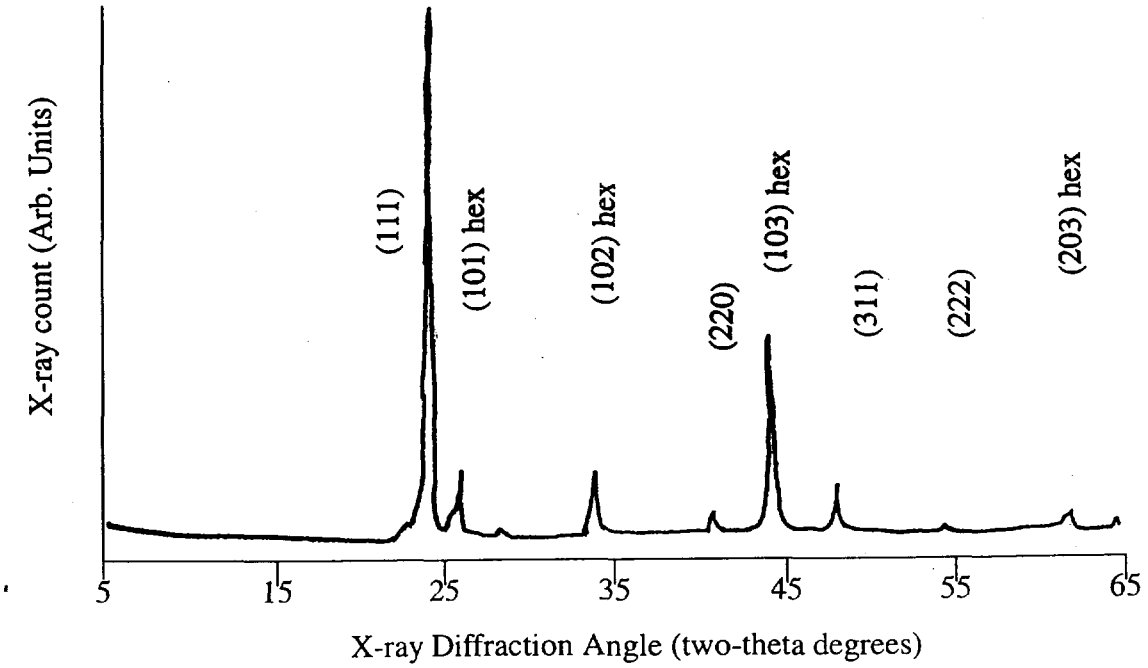

Fig. 6.3 X-ray Diffraction of SrS/CdSe MQW Device with 8 nm thick wells.

In contrast to Fig 6.2, Fig 6.3 shows the X-ray diffraction of the SrS/CdSe MQW device consisting of 8 nm thick wells. All devices closely matched in crystalline quality. Quite surprisingly, it appears that although some phase matching of the CdSe to SrS has taken place; there is still clear evidence of hexagonal phase CdSe. It is important to note again that the main peak cannot be determined as <111> cubic phase or <002> hexagonal though the cubic phase is suspected through phase matching to SrS.

6.1.2 Observed Emission from SrS/CdSe MQW Devices

The electrical and optical characteristics of these devices were examined by applying the standard bipolar pulses as described in section 4.1.2. Light emission from all six sets of SrS/CdSe MQW devices was observed. Emission spectra were measured with the 0.25 m Jarrel-Ash spectrometer. Unfortunately, the total intensity of all devices was very low. For this reason no brightness measurements were achievable. All devices emitted multiple wide emission peaks. This is somewhat unexpected as the quantum transitions should be well defined, and hence produce a sharp emission peak. This unexpected result may be the result of multiple grains of different crystallinity, or widening of quantum levels at the grain boundaries. It may also be the result of film contamination.

As the well thicknesses of the devices were reduced, three general trends were observed. First, there was a shift in the location of all the peaks towards the shorter wavelength, consistent with quantum well behavior. Second, the longest wavelength peak was attenuated whereas the intensity of the two shorter wavelength peaks increased. This may be related to the higher density of states for the narrower wells. As fewer carriers are trapped in the lowest states emission at the larger wavelength diminishes. At the same time a greater number of carriers are trapped in higher energy levels, increasing the rela-

tive emission of the lowest wavelength emission peaks upon recombination. Third, the EL brightness increased, indicating a greater number of trapped carriers recombining radiatively. In summary, as the well size was decreased the emission became brighter and shifted towards the blue, with a total shift of the shortest wavelength peak from 518 nm for the 15 nm MQW device to 424 nm for the 1 nm MQW device. Fig 6.4 shows the spectral shift from the 10 nm well device to the 3 nm well device at a drive frequency of 500 Hz.

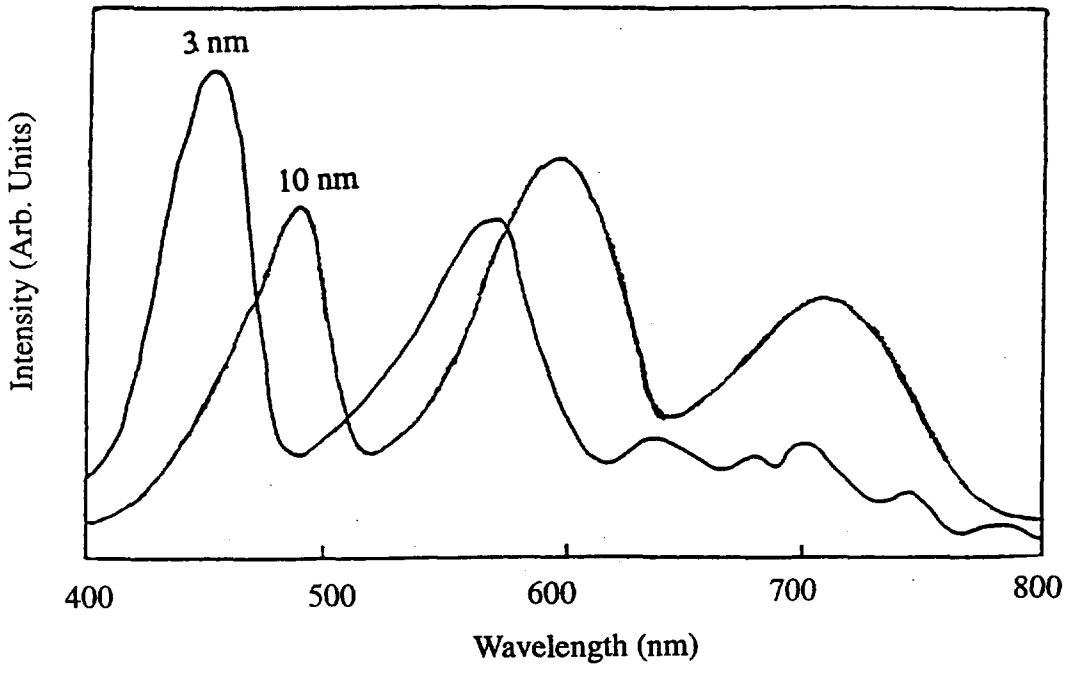

Fig. 6.4 Emission spectra of the 10 nm and 3 nm SrS/CdSe MQW devices at 500 Hz.

As the applied voltage to a given device was increased, at constant drive frequency, two general trends were observed. First, there was a red shift in the emission of all observed peaks, as expected from the model. A comparison between the observed shift and estimated shift is presented below. Secondly, there was a general relative reduction of the lower energy level (higher wavelength) peaks with respect to the higher energy level

peaks in conjunction with an overall increase in intensity. This too is expected. As the applied voltage is increased, so is the number of created electron - hole pairs. It is expected that as the maximum capacity of the lowest quantum level is reached, additional electron - hole pairs, if given sufficient energy, will begin to be trapped by the higher quantum level bands. Fig 6.5 shows the emission spectra of the 15 nm well device structure at 500 Hz drive frequency and varying applied voltage.

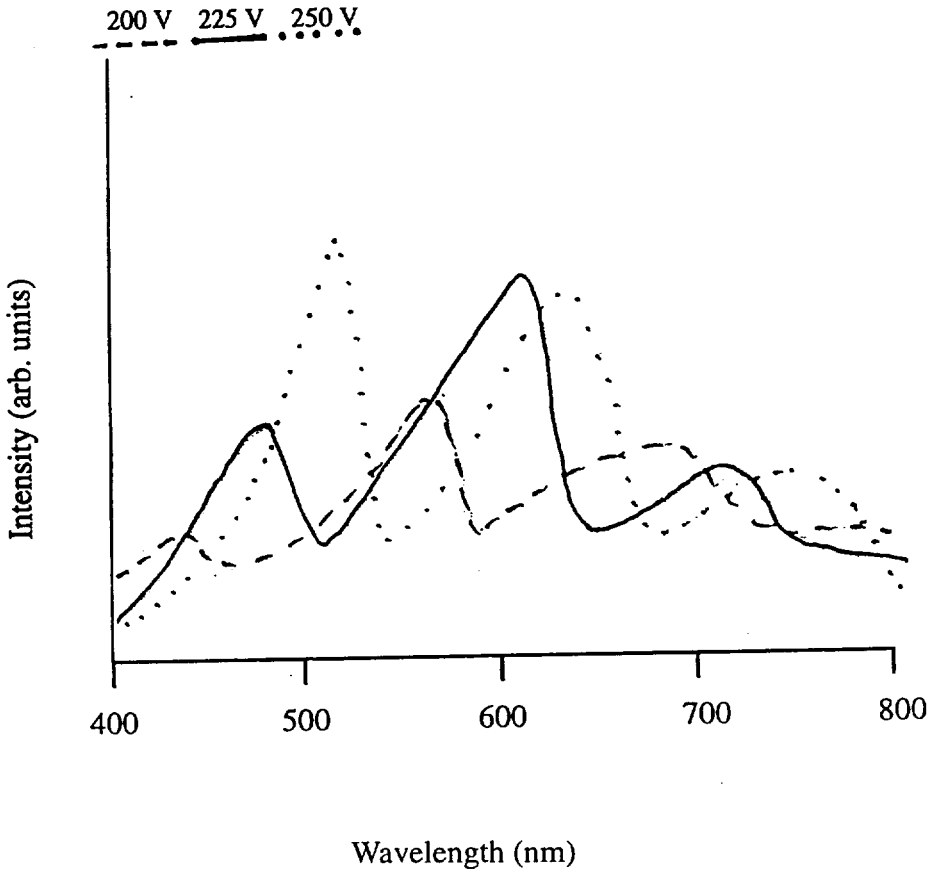

Fig. 6.5 Emission Spectra from 15 nm device at 500 Hz and Varying Applied Voltage.

Fig 6.6 shows the intensity vs. voltage characteristics for the 5 nm device at 60 Hz. (This frequency was chosen for comparison to standard work done with traditional ACT-FEL phosphors.) These measurements were performed using the sum of all emission as a measure of device intensity. As can be clearly seen from the figure, the predicted low emission threshold for MQW devices is indeed observed. This again is indicative of the high energy attained by the electrons as they move into the well. The observed emission at higher energy (lower wavelength) also supports this assumption.

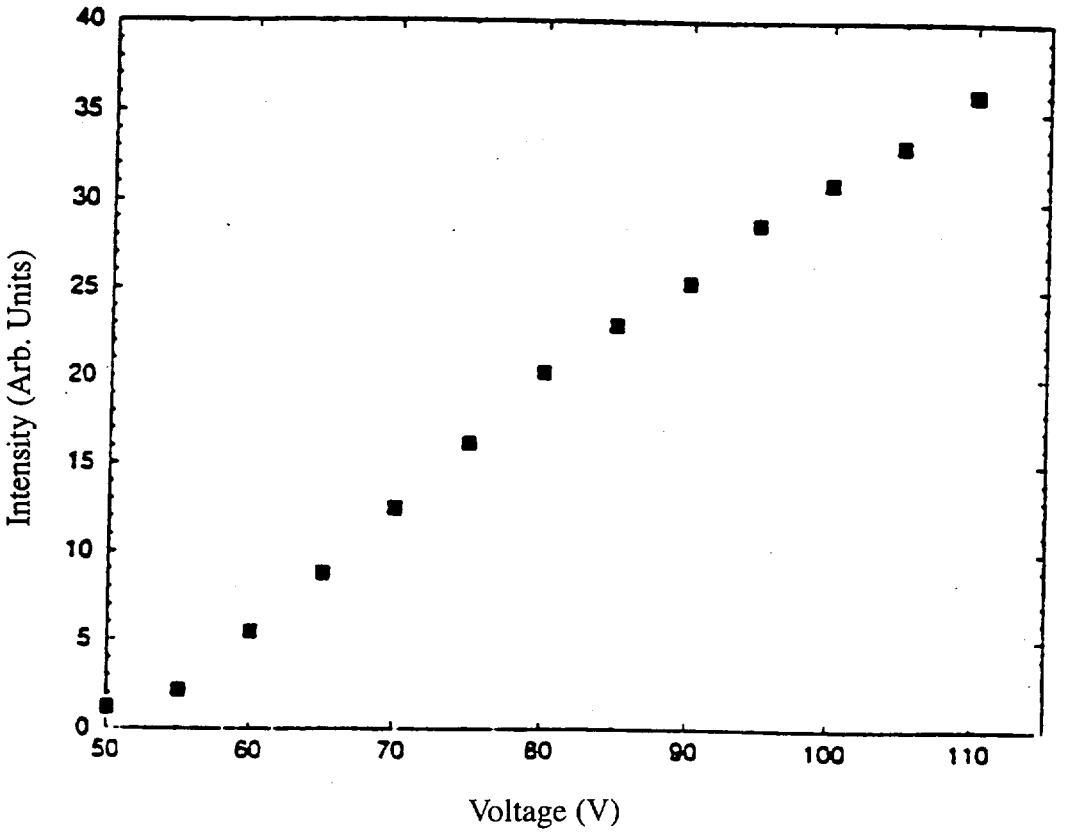

Fig. 6.6 Intensity vs. Voltage for the 5 nm SrS/CdSe MQW device at 60 Hz.

The EL emission spectrum of a 3 nm MQW device is shown in Fig 6.7. As can be seen from this figure, at a drive frequency of 500 Hz, there are two distinct peaks at 453 nm and 565 nm. As the drive frequency is decreased to 200 Hz only half the number of peaks are observed. A similar 'disappearance' of emission peaks with a change in frequency was observed for all the devices, though the frequency range over which it was observed varied for each device. It is hypothesized that acoustic waves in the devices, excited by the driving voltage, result in strong phonon coupling, causing elimination of emission at certain frequencies. In all cases it was observed that as the frequency was increased the more peaks were observed, until a threshold was reached (generally 2 to 3 kHz) when the peaks began to merge together. In some cases, it also appears that there was a slight shift towards the red end of the spectra with increasing frequency. This, however, was not consistently repeatable. There have been no experiments performed to analyze the effects of other driving waveforms.

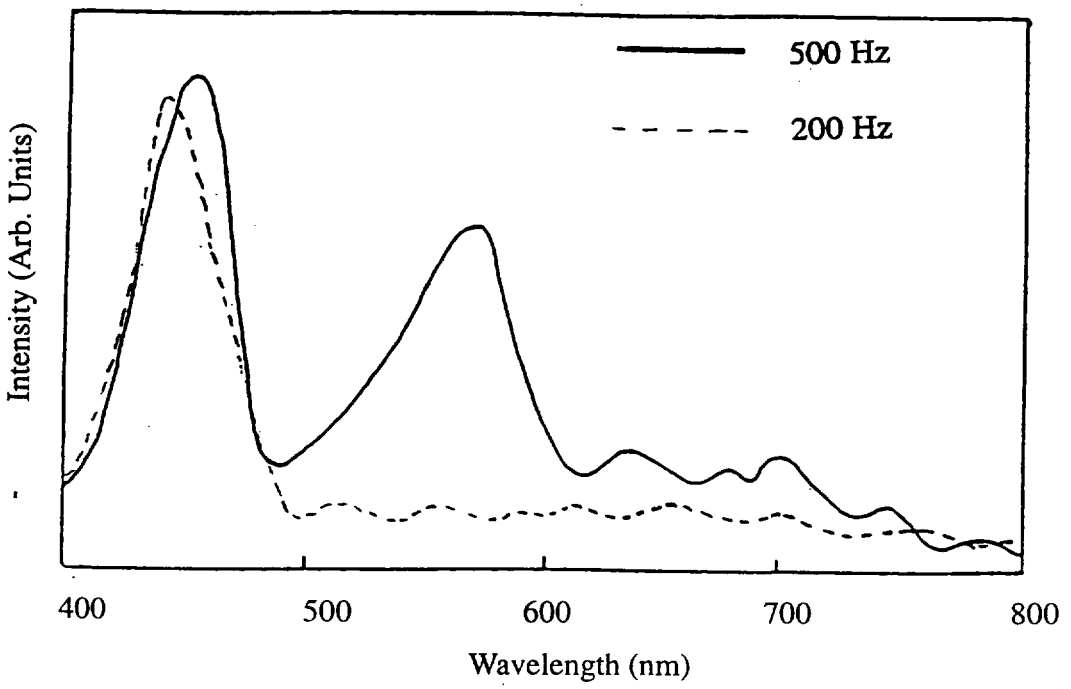

Fig. 6.7 Emission spectra of the 3 nm CdSe/SrS MQW device at 500 and 200 Hz.

The temporal response of the emission from these devices was also examined. Fig 6.8 shows the temporal emission from the 1 nm device, with a 12 μs relaxation time. As can be seen, most of the emission occurs at the leading edge of the voltage pulse. Because the electron hole pairs are generated as the field is increased, this is consistent with theory. A much smaller emission is also observed for the falling edge. This most likely represents emission generated from carriers traveling in the reverse direction driven by the polarization field.

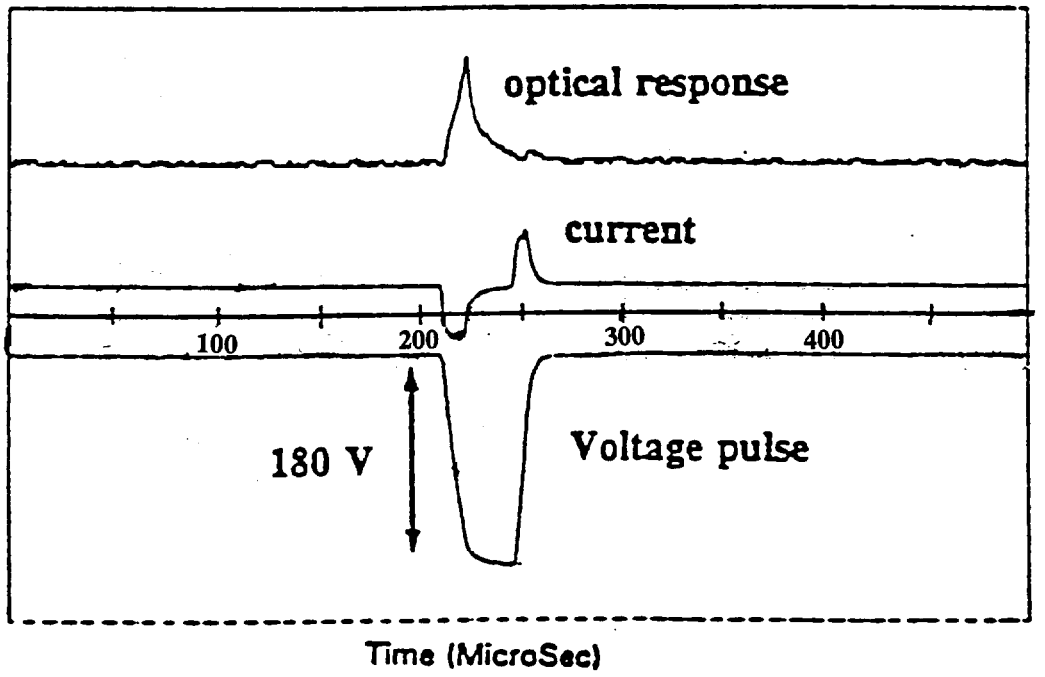

Fig. 6.8 Current and optical response of 1 nm SrS/CdSe MQW device to a single applied voltage pulse.

The low emission from these devices may be attributed to a number of causes. It is believed that increasing the total number of wells (much like increasing the total thickness or doping level in standard ACTFEL devices) should help to increase the total achievable brightness. Optimal host and well thicknesses have also not yet been resolved, though higher intensity was generally observed for the narrower wells. Crystalline defects may also play a strong role in the observed low emission intensity.

6.1.3 Comparison to Model

In order to properly model the MQW phosphor, the electron and hole masses for both SrS and CdSe must be known, as described in Eq 5.2. Unfortunately, there is very little data on such parameters for both SrS and CdSe in the literature. Although it appears from the X-ray analysis that the SrS/CdSe MQW devices may consist of both cubic and hexagonal CdSe, cubic phase values of 0.13 m_0 for the electron mass and 0.45 m_0 for the hole mass of CdSe were used for purposes of modeling [64]. Unfortunately, no data on the difference between heavy holes and light holes was available. Masses for SrS were calculated from the theoretical band model of SrS shown in Fig 6.9 [67]. No similar data for either phase of CdSe has been reported.

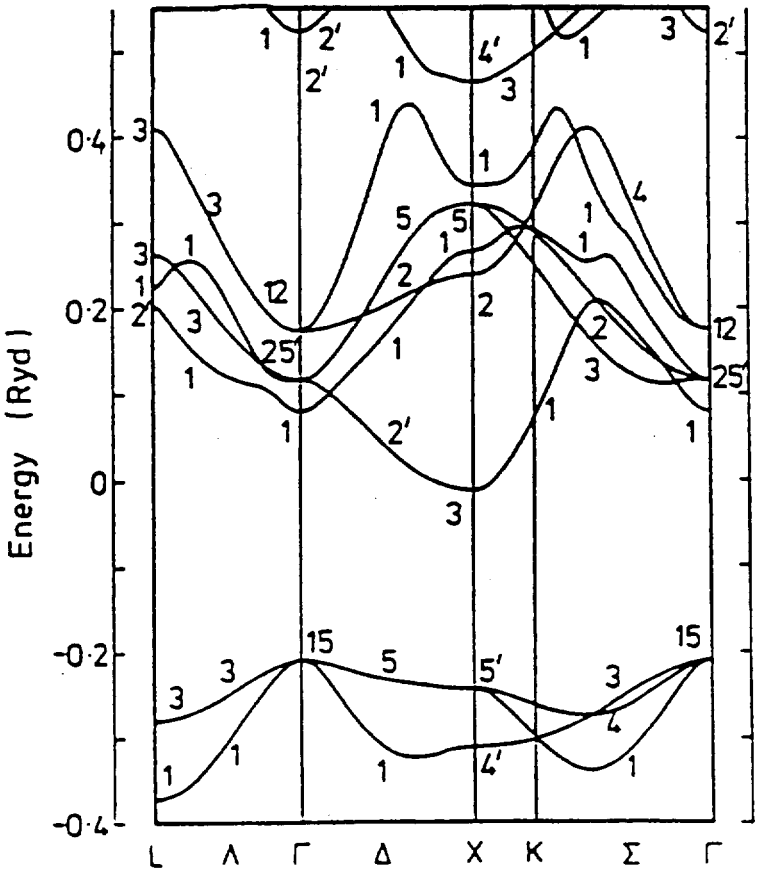

Fig. 6.9 Band Structure of SrS

As described in Eq 6.1 [68] the effective mass is related to the curvature of the band structure. By fitting the conduction and valence band curves to a quadratic polynomial of the form in Eq 6.2 and plugging back into Eq 6.1 the effective mass is calculated as in Eq 6.3. Note that the quadratic fit is only an estimation. As a result, the calculated masses may not be completely accurate. Here, the primary error associated is in graphical extraction from the curves of Fig 6.9. It was observed, however, that the effects of a change of the effective masses in the host are very insignificant in terms of the total calculated emission values. For this reason, the approach here is sufficient.

$$m_B = \frac{h}{\left(\frac{d^2\varepsilon}{dk^2}\right)} \qquad \text{Eq. 6.1}$$

$$\varepsilon = A + Bk + Ck^2 \qquad \text{Eq. 6.2}$$

$$m_B = \frac{h}{2C} \qquad \text{Eq. 6.3}$$

Using this approach, hole masses of 1.9 m_o for heavy hole and 1.0 m_o for light hole were obtained. Similarly, electron masses of 1.4 m_o in the parallel (X - Γ) direction and 0.4 m_o in the perpendicular (X - K) direction were obtained. Because only the more general hole and electron masses in CdSe were available, the values obtained for SrS were generalized using Eq 6.4 and Eq 6.5, where m_h represents the hole mass, m_{hl} is the light hole mass and m_{hh} is the heavy hole mass; and m_e is the electron mass, m_{per} is the perpendicular and m_{par} is the parallel. From these, values of 2.36 m_o for the SrS hole mass and 0.61 m_o for the SrS electron mass were obtained.

$$m_h^{\frac{3}{2}} = m_{hl}^{\frac{3}{2}} + m_{hh}^{\frac{3}{2}} \qquad \text{Eq. 6.4}$$

$$m_e^{\frac{3}{2}} = \left(m_{per}^2 \cdot m_{par}\right)^{\frac{1}{2}} \qquad \text{Eq. 6.5}$$

Using the above values, the MQW emission energies were calculated for both the finite well model and the perturbation model. Here thickness values of 260 nm and 120 nm and dielectric constants of 19 and 8 were used for the ATO and Al_2O_3 oxide layers respectively. Similarly, a dielectric constant of 9.3 was used for the well phosphor. Though there is still some uncertainty involved with the values for input parameters the maximum error in total calculation was found to be less than 10%. (This error was arrived at by incorporating values for effective masses both inside and outside the well, an order of magnitude off and finding the maximum discrepancy.)

As discussed in Sect. 6.1.2, the drive frequency had a pronounced effect on the number of peaks observed. For illustration, the results for the 15 nm well device at constant voltage and varying frequency are shown in Table 6.1 and compared to the model. From the table, it is clear that, though no frequency range showed all predicted peaks, the 1 - 2 kHz range provided the largest coverage of peaks. It should be noted that for frequencies greater than 1 kHz, the emission at the central peaks was reduced. As a result, it becomes difficult to differentiate the peaks. As frequency was decreased below 1 kHz more of the expected emission peaks were not observed. It should be noted that, as frequency was varied, it was not always the same emission peaks that were 'missing'. Rather, as can be seen in the difference between observed peaks at 200 Hz and 500 Hz for this device, there are some peaks in each that are not existent in the other. From the table it

appears that our estimation for device thickness is indeed correct. It should also be noted that, due to the low intensities, the emission for these devices in the lower frequency ranges (< 500 Hz) have a great deal of noise associated with them. For devices with lower thickness, the 1 kHz range appeared optimal for number of peaks observed and their clarity.

Table 6.1 Observed and Predicted Emission for 15 nm Device with Varying Applied Frequency at 200 V

Applied Frequency	QW Energy Transitions (ev)											
	1	2	3	4	5	6	7	8	9	10	11	12
3 kHz	-	-	1.73	-	1.85	1.98	2.18	2.32	-	2.58	-	-
2 kHz	-	-	1.69	1.75	1.83	1.97	2.16	2.33	2.41	-	2.82	
1 kHz	-	-	1.70	1.78	-	1.97	2.15	-	2.41	-	2.79	-
500 Hz	-	-	-	1.78	-	-	2.16	-	-	-	2.85	
200 Hz	-	-	1.70	-	1.84	1.97	2.14	-	2.40	2.63	-	-
Model	1.64	1.66	1.72	1.81	1.90	1.99	2.16	2.38	2.43	2.56	2.83	3.04

Table 6.2 shows the observed emission from the 15 nm well device at 1 kHz and varying applied voltage as well as the predicted emission from the model. It should be noted that because this work focuses on emission in the visible spectra, only emission in the range of 400 to 800 nm was tested. (As a result, some of the predicted transitions were not confirmed.) A number of observations can be made from the table. First, for each observed peak, there is a good match to the prediction. Secondly, as expected there is a general red shift of all the peaks with increasing applied voltage. This effect appears greater for the higher energy level transitions. This also agrees with the model. The effects

from the applied voltage do not appear linear, but rather decrease with increasing voltage. Lastly, it can be noticed that not all the expected peaks have a corresponding observed emission. This may relate to the effects of frequency discussed in Sect. 6.1.2.

Table 6.2 Observed and Predicted Emission for 15 nm Device with Varying Applied Voltage at 1 kHz

.

V	Model /Obs	QW Energy Transitions (eV)											
		1	2	3	4	5	6	7	8	9	10	11	12
0	Model	1.69	1.74	1.81	1.90	2.03	2.18	2.36	2.58	2.82	3.09	3.39	3.69
150	Model	1.65	1.68	1.74	1.83	1.94	2.04	2.22	2.29	2.57	2.72	3.02	3.31
	Obs	-	-	1.72	1.80	-	2.02	2.18	-	2.53	-	2.97	-
200	Model	1.64	1.66	1.72	1.81	1.90	1.99	2.16	2.38	2.43	2.56	2.83	3.04
	Obs	-	-	1.70	1.78	-	1.97	2.15	-	2.41	-	2.79	-
250	Model	1.63	1.65	1.70	1.78	1.87	1.95	2.09	2.45	2.37	2.56	2.68	2.84
	Obs	-	-	1.68	1.75	-	1.94	2.06	-	2.36	-	-	3.02

Table 6.3 shows the predicted and observed emission for all SrS/CdSe MQW devices at 200 V and 1 kHz. From the table a number of observations can be made. As predicted by the model, there appears to be a larger effect from field perturbation on the narrower wells than on the wider wells. It appears that as the width of the well is decreased, the match between predicted and observed peak positions begins to fall off. This is not completely unexpected as the narrower wells will be more sensitive to variations in input parameters.

Table 6.3 Calculated and Observed Emission from SrS/CdSe MQW Devices at 1 kHz and 200 V.

QW Width (nm)	Theory/ Experiment	QW Energy Transitions (eV)											
		n=1	n=2	n=3	n=4	n=5	n=6	n=7	n=8	n=9	n=10	n=11	n=12
15	Finite Well	1.69	1.74	1.81	1.90	2.03	2.18	2.36	2.58	2.82	3.09	3.39	3.69
	Perturbation	1.64	1.66	1.72	1.81	1.90	1.99	2.16	2.38	2.43	2.56	2.83	3.04
	Observed	-	-	1.70	1.78	-	1.97	2.15	-	2.41	-	2.79	-
10	Finite Well	1.72	1.80	1.94	2.13	2.40	2.73	3.12	3.57				
	Perturbation	1.58	1.72	1.84	2.01	2.17	2.47	2.82	3.12				
	Observed	1.59	1.69	1.82	2.02	2.18	2.40	2.70	-				
8	Finite Well	1.73	1.85	2.06	2.36	2.76	3.25						
	Perturbation	1.58	1.76	1.94	2.02	2.39	2.76						
	Observed	1.59	1.80	1.94	2.02	2.38	2.70						
5	Finite Well	1.77	2.04	2.52	3.21								
	Perturbation	1.58	1.83	2.12	2.62								
	Observed	-	1.81	2.07	2.58								
3	Finite Well	1.86	2.46	3.57									
	Perturbation	1.64	2.06	2.86									
	Obvserved	1.59	2.10	2.64									

In addition to electroluminescence, standard photoluminescence was also detected in some devices. Fig 6.10 shows the PL emission from the 8 nm device. As can be seen there is a very close match between the PL emission and the predicted emission using the standard finite well calculation, represented in the figure with bold lines. Surprisingly the predicted transitions in the figure represent only the n=5 and n=4 transitions. The reason for this is not known at this time.

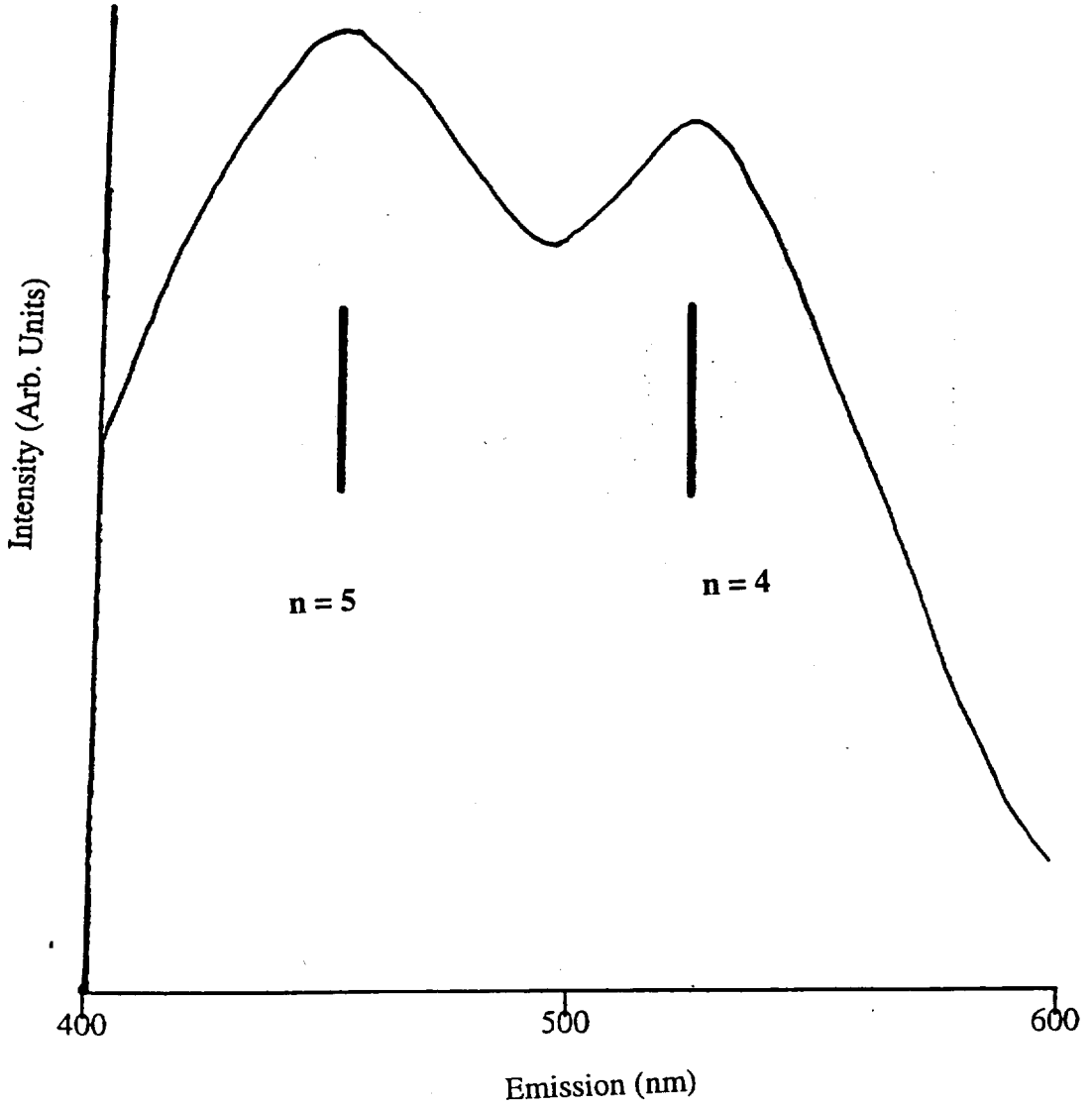

Fig. 6.10 Photoluminescence of the 8 nm SrS/CdSe MQW device.

6.2 ZnSe Wells in CaS Hosts

In order to verify that the emission seen in the SrS/CdSe MQW devices was reproducible for other choices of materials, a new MQW device was created from a completely new set of host and well materials. For this particular device the choice of ZnSe wells in CaS host materials was selected. Like SrS, CaS has been studied for some time as a possible ACTFEL host material and has been successfully grown in our lab with the F-120 ALE reactor. Similar to the case of CdSe in SrS, ZnSe was chosen as the well material for its close lattice match to CaS (5.695 nm to 5.668 nm respectively) and for the relatively large difference in band gap to CaS (2.70 eV to 4.40 eV respectively) (See Fig. 6.11.)

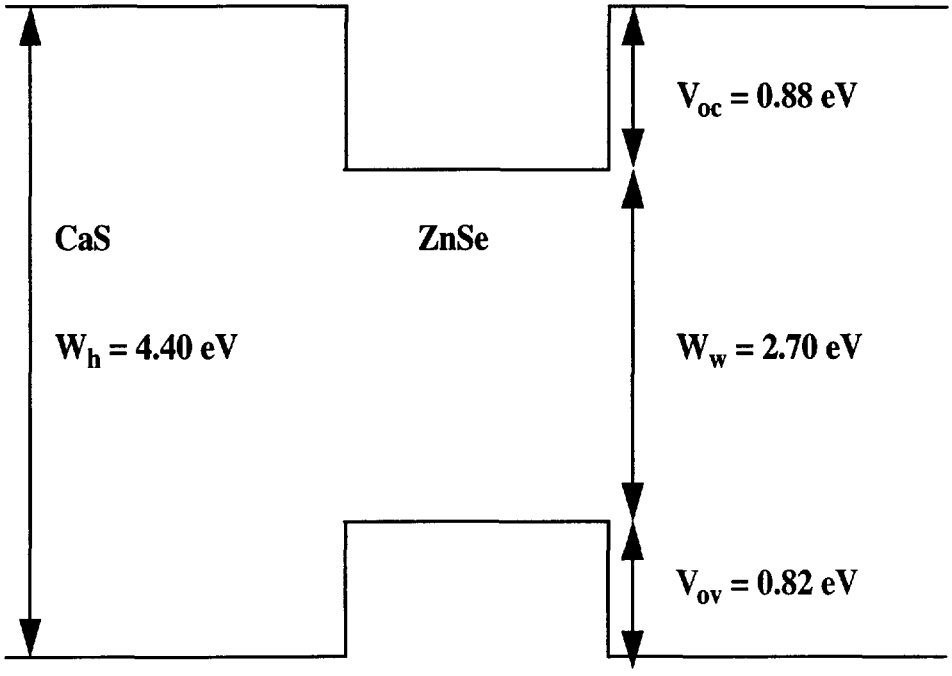

Fig. 6.11 Band Structure of the CaS/ZnSe MQW Devices.

6.2.1 Growth of CaS/ZnSe MQW Devices

Like SrS, growth of CaS has been previously optimized with the F-120 ALE reactor for use in ACTFEL devices, using $Ca(thd)_2$ and H_2S precursors. Substrate temperature used was 395°C. The source temperature for $Ca(thd)_2$ was 186°C. The $Ca(thd)_2$ source was purged for 0.66 seconds followed by a 0.33 second dry nitrogen purge and a 0.88 second H_2S cycle and a subsequent 0.66 second dry nitrogen purge. Growth rate was measured via profilometry and determined to be 0.06 nm/cycle with a 3% deviation in the vertical (perpendicular to flow) direction and a 6% deviation in the horizontal (parallel to flow). It should be noted that thickness measurements of CaS using profilometry are very difficult as the CaS films grown are very soft. Often a small track in the film from the profilometry probe was observed indicating that the probe was actually penetrating the film. As a result, the actual growth rate may be slightly higher. Fig 6.12 shows the X-ray diffraction of CaS film grown on bare glass. From the figure it appears the resulting film is almost amorphous. The visible peaks are the <200>, <220> and <222> cubic orientations.

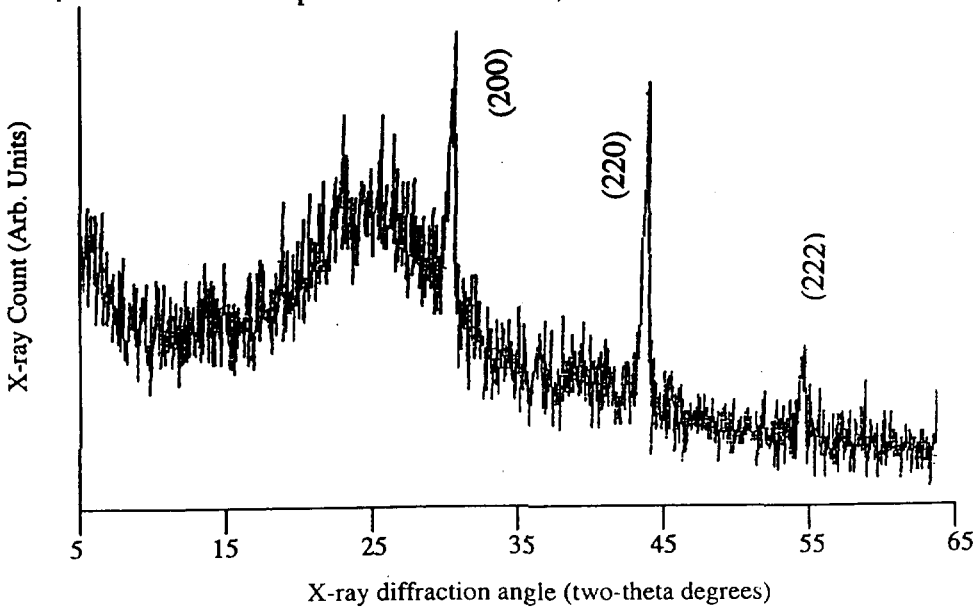

Fig. 6.12 X-ray Diffraction of CaS on bare glass.

For incorporation into the CaS host, growth of ZnSe was optimized at the same substrate temperature of 395 °C. Elemental Zn and Se served as the solid source materials. The Zn source was heated to 382 °C and pulsed for 1.54 seconds followed by a 0.99 second nitrogen purge to prevent formation of ZnSe in the neck of the reactor. The Se source was heated to 275 °C and pulsed for 0.33 seconds followed again by a 0.99 second purge of dry nitrogen. The growth rate of ZnSe on bare glass was found to be 0.3 nm/cycle with less than 5% deviation across the substrate. This large growth rate, as in the case of CdSe wells, indicates that a true ALE reaction had not taking place; though in both cases it should be noted that growth rate appeared constant over a wide range of growth rates. Fig 6.13 shows the X-ray diffraction of ZnSe on bare glass. Unlike the previous CdSe example, no hexagonal phase peaks were observed.

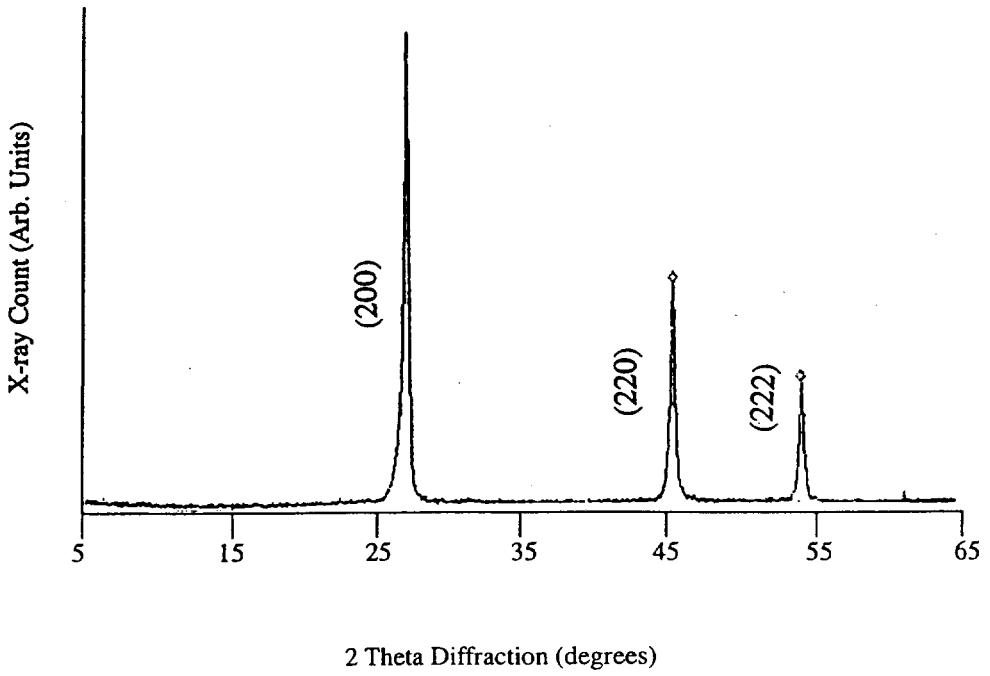

Fig. 6.13 X-ray Diffraction of ZnSe on Bare Glass.

To verify the emission theory CaS/ZnSe devices were created consisting of 10 ZnSe wells separated by 40 nm of CaS. Devices consisting of 10, 8, and 5 nm wells were created. Fig 6.14 shows the X-ray diffraction from the 5 nm device on the traditional ATO/ ITO stack. Although the total crystallinity is low, it can clearly be seen that the orientation of the ZnSe, unlike the previous CdSe example, has switched from the previously dominant <111> orientation to the <200> orientation, matching that of CaS. Again the <220> and <222> orientations are also observed. It should be noted that there is a slight shift from the peaks observed in the MQW structure from those observed for CaS alone. This is an expected result of the size mismatch between CaS and ZnSe molecules.

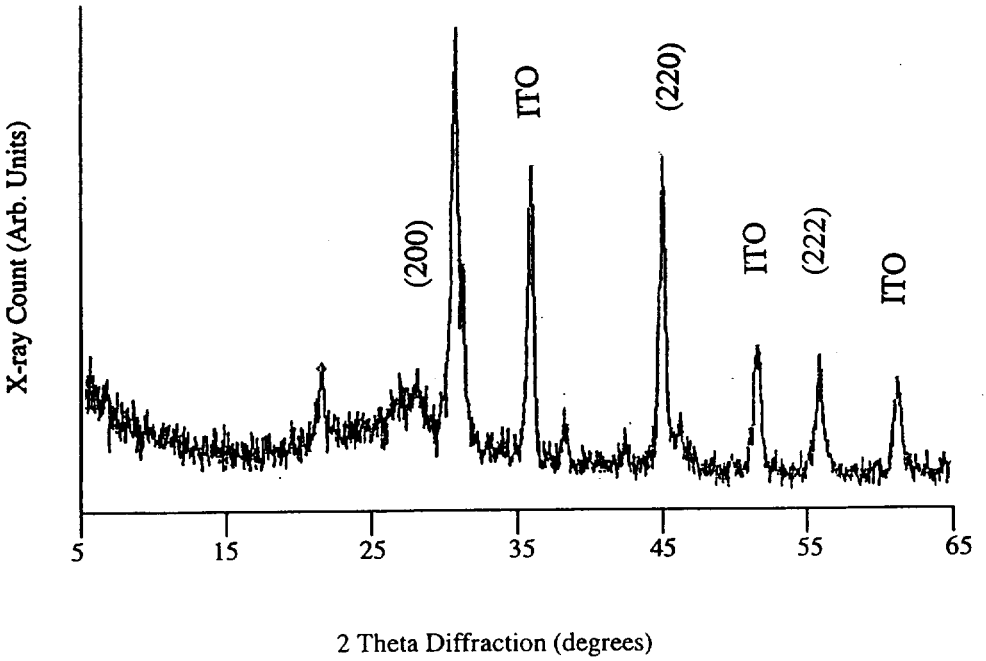

Fig. 6.14 X-ray Diffraction of 5 nm CaS/ZnSe MQW Device.

6.2.2 Emission from CaS/ZnSe and Comparison to Model

Of the three devices grown, emission from the CaS/ZnSe MQW was only observed for the 10 nm device. An emission spectrum at 200 V and 200 Hz is shown in Fig 6.15. Like the SrS/CdSe structure, overall emission was very low. Unlike the SrS/CdSe structure there was no change in emission spectra observed with a change in frequency.

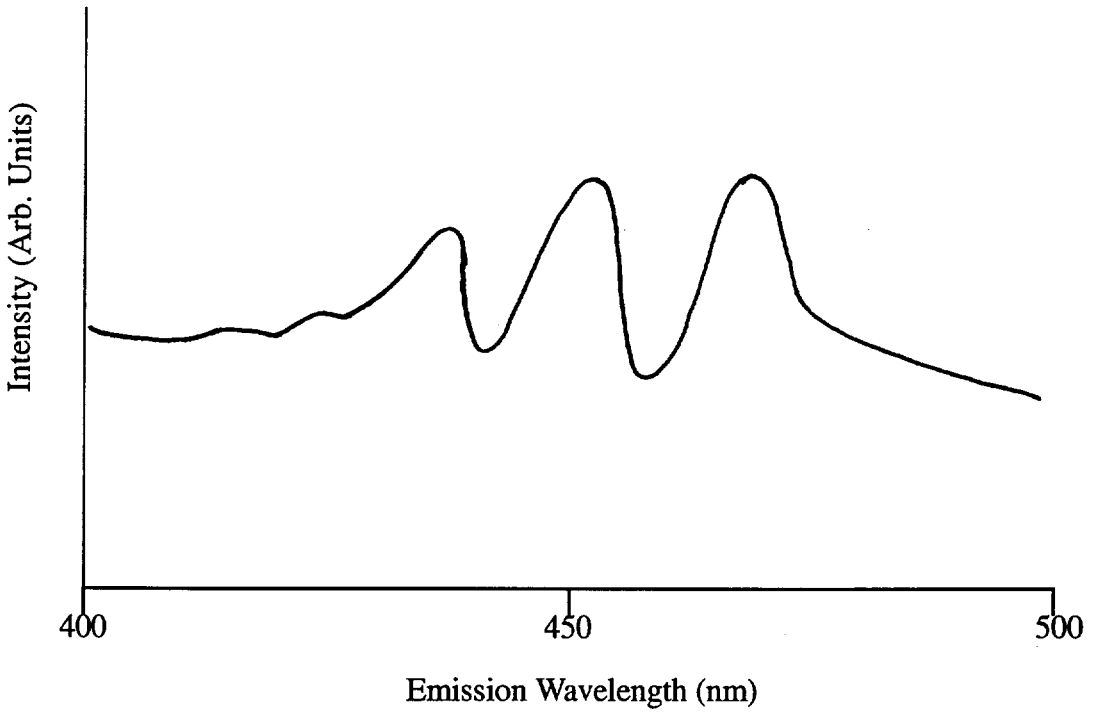

Fig. 6.15 Emission Spectra from 8 nm CaS/ZnSe Structure at 200 V and 200 Hz.

Fig 6.11 shows the band structure of the CaS/ZnSe MQW devices [63]. For the purposes of calculation, masses of 0.15 m_0 and 0.66 m_0 were used for the electron and hole mass of ZnSe respectively [62]. Because of the lack of references and the small impact (< 5%) on the final calculations, the same host masses were used for CaS as were used for the SrS calculations.

The predicted emission energies for the CaS/ZnSe structure at 200 Hz and 250 V are tabulated along with the observed peaks in Table 6.4. In this case the same values for oxide thicknesses and their dielectric constants were used as in the SrS/CdSe case. A dielectric constant of 12 was used for CaS. As can be seen from the table, there is a very close correlation between the model and observed emission peaks. Again, not all expected peaks were observed. This structure does confirm, however, the prediction that emission from MQW devices is indeed possible, though clearly more work is needed to make this a viable commercial product.

Table 6.4 Observed and Predicted Emission for the 8 nm CaS/ZnSe MQW Device.

V	Model/Obs	QW Energy Transitions (eV)				
		n=1	n=2	n=3	n=4	n=5
0	Model	2.73	2.83	3.01	3.25	3.58
200	Model	2.62	2.66	2.76	2.90	3.05
	Obs	-	-	2.73	2.87	3.00
250	Model	2.59	2.62	2.69	2.81	2.95
	Obs	-	-	2.65	2.75	2.84

6.3 Conclusion

The predicted emission from MQW TFEL devices has been successfully demonstrated. Though the match between predicted emission and observed emission is not 100%, the expected trends for MQW emission are clearly seen. From these results, it appears true that for this type of phosphor, it may be possible to engineer the phosphor such that at a known applied voltage the device will emit with a predictable emission spectrum. It is also clear that these devices can be tuned with appropriate field.Clearly, the largest unresolved obstacle at this point is the low intensity observed. Further optimization is still required to determine whether it is indeed possible to produce brightness suitable for flat panel display usage with the MQW configuration. Further work is also required to gain better understanding of the observed effects of driving frequency in the SrS/CdSe device so that any new host/well combinations chosen for MQW work can be created appropriately.

Chapter 7

Conclusions and Future

In this work a number of alternative approaches for blue emission in an ACTFEL display environment have been investigated and reported. In the traditional SrS:Ce blue emitting phosphor it has been shown that it is possible to optimize the total brightness from the devices by optimizing for phosphor layer thickness, frequency and driving waveform as well as the traditional voltage and doping levels. This also appears to be true for other traditional ACTFEL devices. From the data it is clear that it is very possible to achieve far brighter emission from SrS:Ce devices by selecting an appropriate frequency and waveform. It is important to note here that optimizing with respect to frequency and driving waveform is highly application dependent. It is also important to note that when incorporating multiple phosphor layers in producing a white emitting phosphor stack, one must consider the impacts of each phosphor layer separately with respect to driving voltage, frequency and waveform, as each phosphor will have different responses.

It has also been shown that by adding appropriate codopants with Ce in the SrS host it is indeed possible to shift the traditional emission towards the blue. This was observed with both nitrogen and bismuth codoping. This shift is most likely due to charge compensation and relaxation of the crystal lattice field in the vicinity of the activator. Unfortunately, anticipated improvements in brightness, due to greater incorporation of the blue emitting Ce^{3+} ion was not observed. The reduced brightness with these codopants is most likely due to contamination from codopant by-products within the host. Further experimentation in this area, using the same codopants, but from other source compounds, is recommended. This may help to relieve the problems of contamination. It is also useful

to note that by including the investigated codopants from the source compounds used within this work and again optimizing over the proper conditions, it may still be possible to produce a 'bluer' emission than traditional SrS:Ce and still have brightness suitable for ACTFEL display purposes.

Similarly it has been shown that by using ZnS layers within the SrS:Ce phosphor it is possible to again relax the crystal lattice fields at the activator site and again shift the emission towards the blue end of the spectrum. Again there is a decrease in brightness observed in this case. It is recommended that further work be done in this area to optimize for the best position and thickness of the ZnS layers within the phosphor for optimal emission shift and brightness. It is also important to note that care must be taken when selecting the Zn source. Chlorine contamination from $ZnCl_2$ has been shown to alter device emission in some SrS based phosphors, including SrS:Ce. $Zn(thd)_3$, on the other hand has been shown not to have these effects while still producing suitable ZnS host layers.

In the cases of SrS doped with Eu, Sm and Ce, chlorine contamination in an ALE environment has shown to produce emission in the UV to violet range from $SrCl_2$ host formed inadvertently. Currently emission from none of the devices produced in the ALE environment have produced emission in this range suitable for display applications. The main problem here is the inability in this environment to control the chlorine inclusion in the phosphor for optimization. Alternative fabrication techniques, including evaporation or CVD, may prove to be a more suitable method of producing purely $SrCl_2$ host materials.

It has also been shown that blue emission from SrS:Te, which has previously been discarded due to poor intensity, has been shown to produce emission very comparable to those currently achievable with SrS:Ce. Here, however, the emission spectrum from the devices lie more in the desired blue range than those of SrS:Ce. With further optimization

it may be possible to produce a truer blue ACTFEL phosphor material from SrS:Te with emission suitable for display purposes. Further work remains to be done to optimize for doping levels and phosphor thickness.

Finally, a new class of display phosphor, so called QW - activated phosphors, has been presented and investigated. It has been shown that by creating quantum wells within the traditional insulating stack sandwich structure, even in the poly-crystalline environment of ACTFEL devices, emission can be produced due to the recombination of trapped electron - hole pairs excited in the well from electrons moving into the well region. From the research done it does appear that it may indeed be possible to use this technology to 'color engineer' phosphor materials based solely on the choice of host and well materials and applied voltage. The current quantum-well model does adequately represent the observed emission peaks. It is also clear that the high field required in traditional ACTFEL devices is not required here. It is still unclear how the applied frequency affects emission in all devices. Clearly, there is still a considerable amount of work which needs to be done in this area. Investigations into other, well characterized, host/well combinations, for example the nitrides is recommended. Research into other growth techniques which may allow for better epitaxial growth, is also encouraged.

Additionally, further work is required to determine whether the MQW device structure is indeed suitable for producing emission bright enough for use in display technologies. In the observed cases all intensities were quite low. Further work should be continued to try to optimize emission by optimizing well and host thicknesses, total well count and total phosphor thickness. It is also recommended that further work be done to understand the role the overall phosphor crystallinity plays on emission. It is possible that by improving crystallinity, sharper emission lines may be observed. Experiments using other fabrication techniques, annealing procedures, and other host/well combinations may shed further light in this area.

In general, even though this work has not resulted in the creation of a blue emitting phosphor suitable for replacing the existing technologies, considerable insight has been gained into the operating mechanisms of potential ACTFEL devices. With further work it is believed that improved blue emitting ACTFEL phosphors are indeed achievable suitable for display purposes. Note that in the time since these experiments have been performed new information on blue ACTFEL emission from SrS:Cu,Na and CaS:Pb has been published and show great promise [68, 69, 70].

Appendix A

SrS growth via ALE

The atomic layer epitaxy technique has been widely used for the creation of SrS based phosphor materials [23]. By far, the most widely used precursor material used as the strontium source has been $Sr(thd)_2$ [9]. (or bis(2,2,6,6-tetramethyl-3,5-heptaedionato)). This material has become more and more widely available as its demand has increased. In an attempt to evaluate the continuity in growth and performance of the SrS family of devices and in particular the SrS:Ce phosphors, research was performed comparing the growth and luminous characteristics of $Sr(thd)_2$ received from a number of sources, including both commercial vendors and private fabricators. Table A.1 compares the growth and crystalline characteristics of SrS films grown on the previously described ATO/ITO stacks, using the ALE technique with $Sr(thd)_2$ supplied from Strem, Gelest, and ATMI commercial vendors as well as source provided privately by TKK University, Planar America Inc., and Los Alamos National Labs. Both the Planar and Los Alamos Labs sources have undergone an additional sublimation procedure to help in the elimination of contaminants.

For the purposes of comparison, all films were grown using the same basic growth parameters. The only parameter which was optimized for each device was the $Sr(thd)_2$ source temperature which was varied in each case to maximize overall uniformity of the film. All of the SrS films were grown with a substrate temperature of 380°C. H_2S served as the sulfur source in all cases. All phosphors were doped with 1 CeS layer for every 80

SrS layers, as described in Chapter 4. The Ce source used in all cases was $Ce(thd)_3$ from Strem Chemical. In all cases the pulse width for Sr(thd)2 was 0.44 seconds followed by a 0.33 second nitrogen purge. The H_2S pulse width for each run was 0.88 seconds followed by a 0.66 second nitrogen purge. The Ce was doped with a 0.77 second pulse width followed by a 0.66 second nitrogen purge. All films were grown for a total of 3200 SrS cycles. For each film grown, in order to quantify the benefits of annealing [28], one of the two substrates underwent a 4 hour anneal at 500°C exsitu in a nitrogen environment.

As can be seen from the table, the films created from each of the provided sources varied greatly in composition. In general both the Los Alamos and Planar precursor materials produced excellent quality films. While the other materials typically left a deep red or brown residue of unused materials after growth was completed, the sublimated sources typically had only a clear amber residue remaining, perhaps indicating fewer impurities. As can be seen from the table, these materials also produced thicker and typically more uniform films (<5% non-uniformity over the 2"x2" substrates compared with as much as 10% non-uniformity for the commercial sources). The source provided from ATMI produced the poorest crystallinity with very low X-ray counts for all peaks observed. The Strem material was found to be very problematic in that results were seldom reproducible under the exact same run conditions. Often the <200> peak would appear as the dominant peak with little or no <111> peak visible for one run, a second run with the same conditions could then produce a very strong <111> peak with little or no <200> peak visible! Further, the source temperature required for best uniformity also varied from one 10 gram container of material to the next, even for containers produced from the same batch.

Table A.1 Characteristics of SrS films grown via ALE from $Sr(thd)_2$ from varying sources

Source		Source Temp (°C)	Thickness /Cycle (A)	FWHM of the (2Θ) XRD Peaks		
				(111)	(200)	(220)
Strem	before anneal	219	0.63	0.29	0.33	0.43
	after anneal		0.58	0.30	0.34	0.40
Gelest	before anneal	215	0.69	0.30	-	0.56
	after anneal		0.70	0.28	-	0.53
TKK	before anneal	210	0.71	0.28	-	0.46
	after anneal		0.67	0.27	-	0.44
ATMI	before anneal	220	0.58	0.40	0.30	0.50
	after anneal		0.63	0.39	0.38	0.51
Los Alamos	before anneal	223	0.83	0.43	0.51	0.60
	after anneal		0.79	0.40	0.52	0.61
Planar	before anneal	224	0.85	0.32	-	0.42
	after anneal		0.81	0.29	-	0.39

In virtually all cases the anneal did appear to increase the intensity and reduce the full width at half maximum for the dominant X-ray peak. (Which peak was "dominant" was determined by comparing the intensity of each visible peak with the reported intensities for uniform SrS powder materials. The peak with the largest of film to powder in X-ray intensity was considered dominant.) The opposite appeared to happen for the smaller peaks. This seems to indicate that in general the anneal helps to improve crystallinity by increasing the grain sizes and eliminating the less common peaks. (Note that in some cases the full width at half max for some of the secondary peaks appears to have increased. It should be pointed out that often the total count for these peaks typically decreased for what in some cases were already small peaks. As a result the error associated with the measurements for these peaks may be higher than for the dominant peaks.) In all cases the (222) peak was visible, but was too small to be accurately measured. A typical X-ray pattern of SrS is shown in Fig 4.4.

It should also be pointed out that the choice of activator doped into the host can have a dramatic effect on the crystallinity of the film. In general SrS films doped with Eu had a stronger (111) peak and reduced (200) peak with the exception of films produced using the Sr(thd)2 source from Strem Chemical, which had the exact opposite effect. This is likely the effect of the differences in size and solubility of the different dopants.

A.1 Optical performance

Using the same growth conditions, ACTFEL devices were created using Al_2O_3 created with the Al-isopropoxide precursor method for the back-side oxide, as described in Appendix C, and sputtered Al dots as the back-side conductor and sputtered ITO and ATO as the front (substrate side) conductor and oxide respectively. All phosphors were

doped with 1 CeS layer for every 80 SrS layers. These devices were compared against total achievable brightness. The results are presented in table A.2. All measurements were made at 60 Hz and 40 V above threshold. (V_{th} varied within 10% between films, most likely due to changes in total film thickness and amounts of contamination.)

As can be clearly seen from the table the Planar America and TKK sources, both of which have undergone a sublimation process, produced phosphors which emitted far brighter light. The table also clearly demonstrates the benefits of the anneal procedure. All phosphors, with the exception of the ATMI sourced devices, achieved greater brightness and a slight blue shift in CIE coordinates with an anneal at 300 ^{o}C for three hours. In general, it was also observed that the devices which underwent the anneal process consistently survived greater applied fields before device failure. This is consistent with previous works which linked improved crystalline quality with enhanced optical quality [71]. As detailed in Chapter 4, it has been observed that the brightness and emission from SrS:Ce as well as other phosphors is a variable of the total thickness of the device. In general thicker devices produce brighter emission with higher threshold voltages and sharper brightness vs. voltage slopes. This may be a factor in the improved performance of the devices grown from the sublimated source over the non-sublimated source materials.

In general all devices appeared to exhibit the same type of electrical behavior, consistent with those reported previously [2]. In all devices grown, the typical SrS:Ce device has both a leading and trailing edge intensity peak associated with each voltage pulse. This is typically attributed to the role of space charge in the phosphor. As a voltage pulse is applied some of the Ce ions will be activated producing the leading edge pulse. Other Ce ions may be actually further ionized. The freed electrons may then travel to the opposite end of the phosphor film. As the voltage is relaxed these freed electrons are able to move back across the phosphor. These may recombine with the ionized activators again produc-

ing emission. This is associated with the trailing edge emission [72]. In all devices, the leading edge emission was greater than the trailing edge emission, for both the positive and negative voltage pulses.

Table A.2 Optical characteristics of SrS:Ce grown via ALE with varying $Sr(thd)_2$ sources

Source		CIE	Brightness (fL)
Strem	before anneal	x=0.28, y=0.60	0.95
	after anneal	x=0.22, y=0.39	1.10
Gelest	before anneal	-	-
	after anneal	-	0.35
TKK	before anneal	x=0.38, y=0.51	1.35
	after anneal	x=0.33, y=0.48	1.50
ATMI	before anneal	x=0.31, y=0.47	1.05
	after anneal	x=0.29, y=0.48	1.00
Los Alamos	before anneal	x=0.33, y=0.52	2.35
	after anneal	x=0.30, y=0.50	2.55
Planar	before anneal	x=0.31, y=0.48	3.85
	after anneal	x=0.27, y=0.45	4.30

From these experiments, it was determined that the sublimated $Sr(thd)_2$ sources from Planar America and Los Alamos Labs proved to have the highest achievable brightness, best crystalline quality and best film uniformity. Additionally, these films in general produced more consistent results from run to run. For this reason the majority of devices using SrS materials were created using one of these two sources, typically the source from Planar America. Unfortunately, because neither of these are commercial vendors, it was not always possible to secure these sources. In such cases $Sr(thd)_2$ from Strem Chemical was used. Although it was found to have poorer overall performance and the characteristics from one film to the next varied greatly, it is readily available and relatively inexpensive.

A similar comparison was performed between $Ce(thd)_3$ from Strem Chemical vs. sublimated $Ce(thd)_3$ provided by Planar America. Little difference in both film growth and optical performance was detected between the two sources. Because of its availability, the Strem source was chosen as the Ce source for all SrS:Ce device research presented previously in this work.

Appendix B

Low Temperature Growth of ZnS:Mn Phosphors from Diketonate Precursor

As has already been pointed out, the highly efficient orange-yellow emission from ZnS:Mn based TFEL devices have become the standard by which all other phosphor types are measured. Several deposition methods, including evaporation, CVD and ALE, have been successfully used to produce this phosphor [53]. Typical ALE growth of the ZnS host material has been accomplished with the use of $ZnCl_2$ precursors, though the use of zinc acetate, $Zn_4O(CH_3COO)_6$, has also been successful [73]. Both of these methods, however, require processing at high temperatures (400 to 500 ^oC). This high temperature not only adds additional time to the fabrication process, but it also can make the creation of stacked phosphors, used for the production of white light emitting or multicolored phosphors, more difficult. For example, the typical substrate temperature for SrS growth from its beta diketonate, is 375 ^oC. Additional reactor time is required to heat/cool between every subsequent layer of SrS and ZnS type materials. In addition, as was observed for the ZnS/SrS stacked devices reported in Chapter 4, growth from $ZnCl_2$ has been shown to have chlorine contamination which may aversely affect the emission from neighboring SrS phosphors in a white light emitting or multicolored structure. For these reasons the ALE growth of ZnS from its beta-diketonate precursor, $Zn(thd)_2$ was investigated.

B. 1 ALE Growth of ZnS from $Zn(thd)_2$

Undoped ZnS films were prepared simultaneously on bare glass and standard ITO/ ATO coated plates. The sulfur source was again H_2S. ZnS film growth was accomplished using a $Zn(thd)_2$ source temperature of 112 °C. The pulse width of the $Zn(thd)_2$ was 0.22 seconds followed by a 0.66 second nitrogen purge. Similarly, the H_2S pulse width was 0.22 seconds followed again by a 0.66 second nitrogen purge. The substrate temperature was varied from 200 to 450 °C. In addition to the undoped phosphors, ZnS:Mn phosphor films were also produced on both bare and coated substrates. The precursor used for Mn incorporation was $Mn(thd)_3$. The source temperature for this compound was 130 °C. Its pulsing time was 0.22 seconds followed by a 0.66 second nitrogen purge. This was followed by a 0.88 second H_2S pulse and another 0.66 second nitrogen purge. Doping levels were varied from 1:200 to 1:40. Al_2O_3 from the Al-isopropoxide method detailed in appendix C and sputtered aluminum dots were used to complete the devices.

Fig B.1 shows the X-ray analysis for phosphor layers deposited on bare glass substrates with varying substrate temperature. In all cases, the <111> cubic ZnS peak dominated. The <220> cubic phase and <311> hexagonal phase were also observed in some of the films. It can be clearly seen that the relative intensity of the latter peaks increased for films grown at higher temperatures. This is consistent with similar studies using chemical vapor deposition, CVD, with a dimethyl zinc precursor [74]. From the figure it is also clear that deposition at 300 °C provided the best crystalline quality, with a full width half maximum (FWHM) for the <111> cubic phase peak of 0.2°.

In addition to the effects of substrate temperature, it was also found that the doping level played a roll in the final film crystallinity. Fig B.1 also shows the difference between

an undoped ZnS film and one doped 80:1 with Mn. Both films were deposited at 300 °C. It shows an overall decrease in intensity and increase in the FWHM of the <111> cubic phase peak for the doped film. In addition the recurrence of the <311> hexagonal peak is also seen. It was observed that as the doping level was increased from 200:1 to 80:1 the FWHM of the <111> cubic phase peak increased from 0.24° to 0.28°. In addition, the <311> peak spread from a FWHM of 0.41° to 1.08°. This phenomena is most likely due to the size mismatch between Zn and Mn atoms. As the larger Mn atoms are incorporated into the film, smaller grain sizes are created.

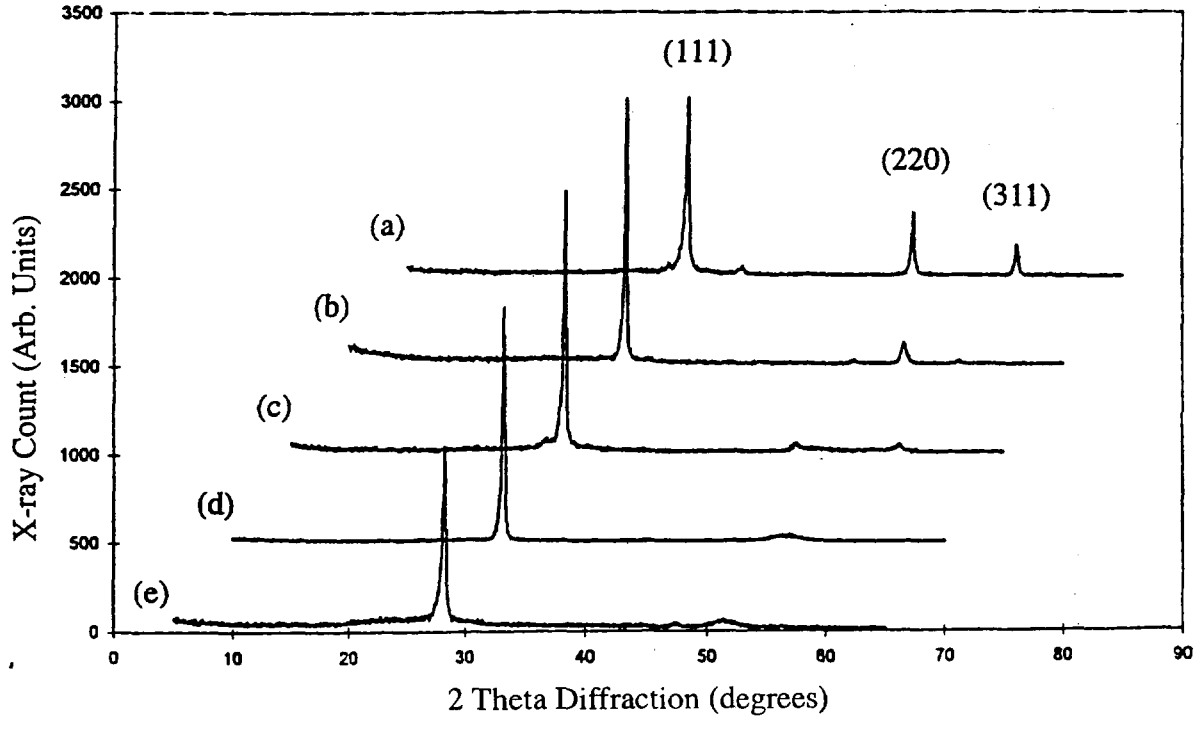

Fig. B.1 X-ray diffraction spectra for ZnS grown at (a) 450 °C, (b) 350 °C (c) 300 °C (d) 300 °C with Mn doping 80:1 and (e) 250 °C.

In addition to a decrease in crystallinity with Mn doping, the overall film uniformity decreased dramatically with an increase in Mn doping. Table B.1 shows the growth rate of ZnS:Mn layers and the degree of non-uniformity for different doping levels. As the doping level was increased the non-uniformity also increased. This non-uniformity was so great as to cause as much as 20% difference in emission brightness for devices operating under the same amplitude bipolar waveform for pixels at opposite ends of the film. For this reason all emission characteristics measured were taken from the pixels closest to the inlet source (for maximum Mn incorporation). This problem may be eased with use of a more suitable Mn precursor or with a suitable codopant.

Table B.1 Growth Rate and Uniformity for ZnS:Mn devices at various doping levels.

Doping Ratio	Growth/Cycle (Angstroms)	% Deviation (perpendicular to flow)	% Deviation (parallel to flow)
Undoped	0.86	1	3
200:1	0.85	9	17
160:1	0.82	15	26
80:1	0.83	18	29
40:1	0.79	21	32

B.2 EL Emission

The ZnS:Mn devices were excited with the standard bipolar waveform with a frequency of 60 Hz. All devices emitted the same expected orange-yellow broad band spectra peaked at 593 nm as shown in Fig B.2 with CIE coordinates of x=0.49 and y=0.50. Fig B.3 shows the brightness versus voltage characteristics for the devices with varying Mn doping concentration. As Mn concentration increased, overall brightness of the device also increased, creating a steeper curve and hence increasing the threshold voltage. Overall the threshold voltage increased from 35 V for 200:1 doping to 120 V for 40:1 doping. This increase in the threshold voltage may be due to the distortion of the crystal lattice observed with an increase in Mn concentration in the X-ray analysis.

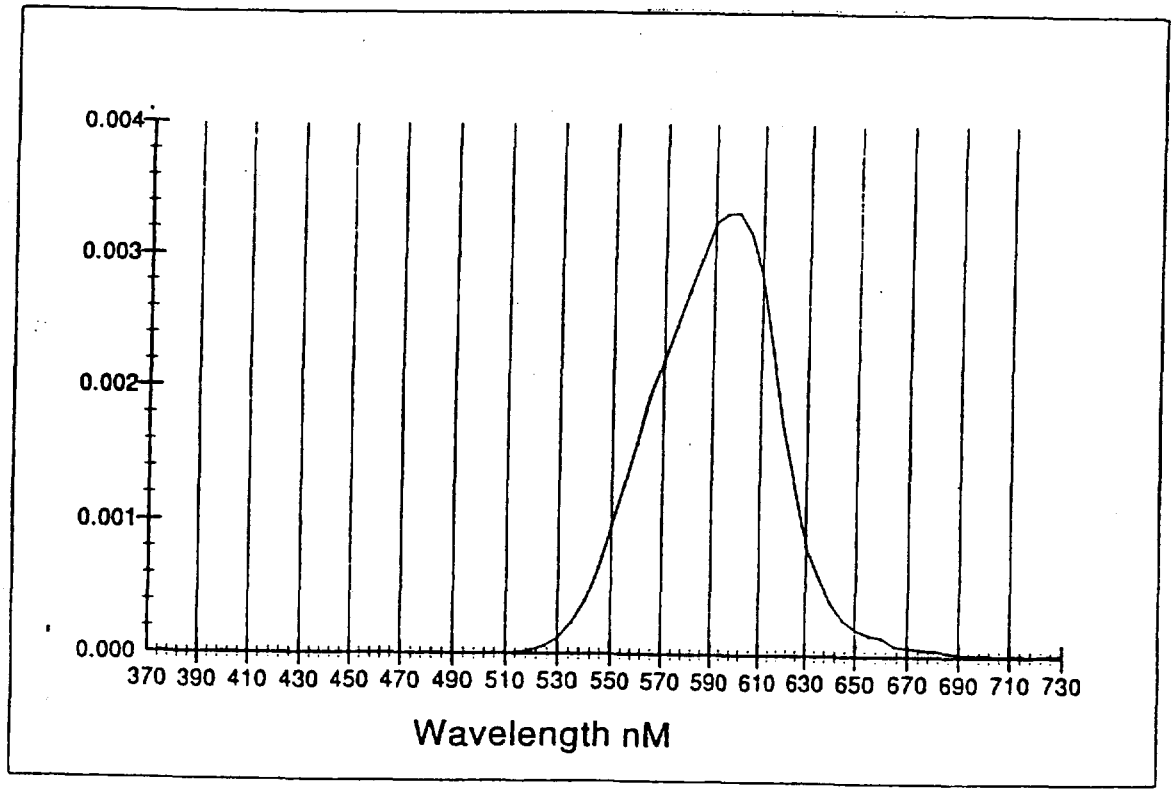

Fig. B.2 Emission Spectra of ZnS:Mn grown from Zn(thd)2 precursor.

The EL lifetimes were measured by applying 5 microsecond wide pulses at 100 Hz. It was observed that as the doping concentration was increased there was a general decrease in emission lifetimes. This agrees with previous observations [75]. The observed decrease in lifetimes ranged from 0.8 microseconds for the 200:1 devices to 0.5 microseconds for the 40:1 doped devices. This drop in lifetimes for higher Mn concentrations may be due to Mn^{2+} to Mn^{2+} interactions, where the energy from an excited ion is transferred to an unexcited ion which then releases energy via nonradiative decay.

Fig B.3 shows the effect of doping level on brightness for the ZnS:Mn devices. Like the case for the SrS:Ce devices, there is an overall increase and brightness and shift towards higher threshold voltage with increased doping, until a saturation point is reached where further increase in doping no longer increases the device brightness. This may be due to an overall change in the crystal environment with excess doping levels.

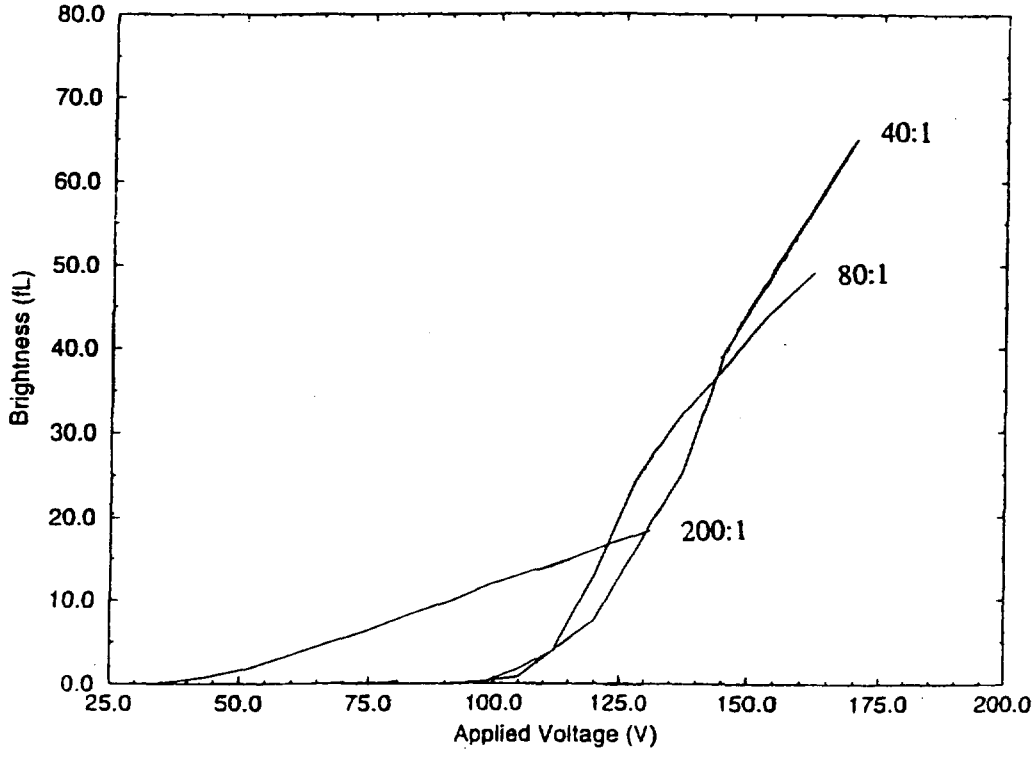

Fig. B.3 Brightness vs. Voltage for ZnS:Mn devices at varying doping levels.

Appendix C

TFEL Oxide Layer Growth by Atomic Layer Epitaxy

As has been described previously, the ACTFEL device requires a "double insulating sandwich" structure. The insulators in the structure act as the source of electrons necessary for luminescence in the phosphor material. There are many characteristics which must be considered when choosing the proper dielectric layer materials. In ACTFEL applications, the insulating layers should be transparent to allow for transmission of the light through the material. The material should be as free of defects and pin holes as possible to prevent electrical breakdown and increase shelf life of the device. A high permittivity will assure that a high portion of the applied electric field will be present across the phosphor during operation. Good film uniformity is also important to keep the performance of each pixel similar. Another consideration is the index of refraction of the film. Because emitted light must travel from the phosphor through the top dielectric layer, this layer should ideally have an index of refraction lower than that of the phosphor material. Similarly, since light may pass through the back dielectric and be reflected off the metal contact to pass through the dielectric again into the phosphor, this material should be matched closely to the index of refraction of the particular phosphor. For this reason, the top oxide and bottom oxides in an ACTFEL structure are typically not the same.

Aluminum oxide (Al_2O_3) has long been used in the ACTFEL industry as a top layer insulator. Successful growth by the ALE technique has been reported using $AlCl_3$ solid source with both H_2O and $(CH_3)OH$ liquid oxygen sources [24, 76, 77]. This appendix presents the growth and electrical characterization of Al_2O_3 using alternative Al

sources, including Al-isopropoxide $[OCH(CH_3)_2]_3$, $Al(thd)_2$ or bis(2,2,6,6,-tetramethyl-3, 5heptanedionate), $Al(C_2H_5)_3$ or (triethyl aluminum or TEA), and $Al(CH_3)_3$ or (trimethyl aluminum or TMA). Additionally, growth of Ta_2O_5 using H_2O with $Ta(OC_2H_5)_5$ solid sources is presented.

C.1 ALE Growth of Al_2O_3

The Al_2O_5 oxide layers grown with the F-120 ALE reactor using $AlCl_3$ solid source material have been associated with chlorine contamination, which may have an effect on phosphor emission [24]. For this reason, alternative aluminum source materials have been investigated for possible use in the growth of Al_2O_5 films. A number of alternative films have been grown using the F-120 ALE reactor with various metallic and non-metallic precursors. Their growth and electrical properties are summarized in table C.1. (Horizontal deviation represents uniformity deviation of the film in the direction of the source flow. Vertical is perpendicular to the direction of source flow.) All of the Al_2O_3 films grown were found, through X-ray analysis, to be amorphous. The growth conditions and quality of film growth varied greatly for the various precursors. The ALE growth and characterization of Al_2O_3 from $AlCl_3$ with H_2O and $(C_3H)_3OH$ has already been reported in detail [27]. The following sections will detail the growth or attempted growth of Al_2O_3 from Aluminum isopropoxide with no additional oxide source, and from Trimethyl Aluminum, Triethyl Aluminum and $Al(thd)_2$ metallic precursors with water. Thicknesses and index of refraction were measured using profilometry or ellipsometry. Dielectric Constant was determined by measuring the capacitance of the thin films on ITO with sputtered Al top contacts for films with known thicknesses [26].

Table C.1 Properties of Al_2O_3 Grown from Various Precursor Materials

Sources	Growth Rate (A/cycle)	deviation (horizontal)	deviation (vertical)	dielectric constant	index of refraction
$AlCl_3$ H_2O	0.80	NA	NA	12.3	NA
$AlCl_3$ $(C_3H)_3OH$	0.45	NA	NA	12.3	NA
Al $[OCH(CH_3)_2]_3$	2.33	6%	1.5%	8.5	1.57
$Al(C_2H_5)$ H_2O	0.1	NA	NA	NA	NA
$Al(CH_3)_3$ H_2O	0.85	5%	2%	12.6	1.51
Al(thd) H_2O	No Growth				

C.1.1 Al_2O_3 growth from Aluminum Isopropoxide

The growth of Al_2O_3 from aluminum isopropoxide in an ALE environment was based on previous work [78]. Although the films are grown in the F120 ALE reactor, it is not truly an ALE process, but rather a modified CVD process. In this growth process, the aluminum isopropoxide source acts as both the metallic and nonmetallic source and is carried to the substrate in one single pulse.

In order to grow Al_2O_3 in the F120 reactor with the aluminum isopropoxide source, a preprocessing step, consisting of a source melt in an inert atmosphere, was required. Because the solid isopropoxide source is so fine, melting it within the F120 reactor proved to be impossible, as the vacuum pump alone was enough to eliminate the full amount of source. As a result an exsitu melt was required. To accomplish this task, a small amount (~2 grams) of source was placed in a glass boat and covered with aluminum foil (to prevent evaporation and loss of the source material during the melt). This was then placed in a furnace in a dry nitrogen atmosphere and heated for 25 minutes at 175° C.

This procedure was found to be very important. It was observed that when the source was not fully liquefied prior to placement in the F120 reactor, the corresponding film quality was very poor. Films grown under such conditions were often cloudy in appearance and 'gummy' in texture. Thicknesses of these devices varied greatly and the overall uniformity of such films was very poor. Similarly, films grown from source material which had been fully liquefied and then resolidified, also were poor in quality. Best results were found only when the source was fully melted and placed in the F120 reactor while still in liquid form. Even though the source in such cases would partially resolidify during the growth process, film quality appeared consistently good, with clear uniform deposition.

Once the source was placed in the reactor it was heated to 90° C and purged for 0.44 seconds to the substrate at 380° C followed by a dry nitrogen purge of 6 seconds. At the substrate the material acted as both metallic and non-metallic source forming Al_2O_3. Because this is clearly not an ALE process, the growth rates observed are much higher than the typical one atom per cycle typically expected. Also, unlike a true ALE process, where growth rate varies little at constant substrate temperature with variation in the total number of cycles, the growth rate for the oxide films using aluminum isopropoxide,

though fairly stable, was found to be dependant upon the number of cycles purged. Fig C.1 illustrates this dependency in further detail. As the figure clearly illustrates, the growth rate starts low and initially increases to a peak. It then begins to decrease in growth rate. This decrease in growth rate may be a result of the liquefied source material cooling from the original 175° melting temperature to the 90° C purging temperature. In addition it was observed that the film growth on Si substrates was significantly higher than that on ITO or phosphor materials. For most ACTFEL devices reported here 600 cycles of purged aluminum isopropoxide was used. This resulted in top oxide films of 130 nanometers thick. The same conditions applied to Si substrates produced films close to 200 nanometers thick with uniformity deviations less than 1% in both the vertical and horizontal directions.

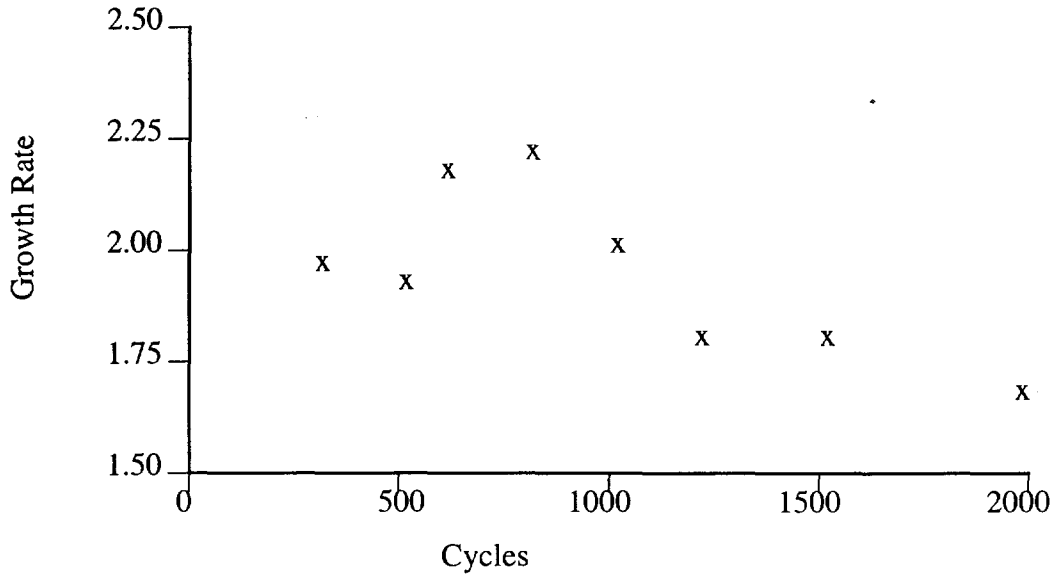

Fig. C.1 Growth Rate vs. Cycles for aluminum isopropoxide grown Al_2O_3.

In addition to the preprocessing melt step required, a post-processing anneal step has also been recommended for this growth procedure. After the film has been grown, the substrate is removed from the reactor and placed back into the furnace in a nitrogen environment. The films are then annealed. Table C.2 summarizes the film characteristics under various anneal conditions. All films were grown for 600 cycles as detailed previously on Si substrates. As can be seen from the table, the film growth characteristics on Si vary only slightly with anneal. It is clear that an anneal at 500°C is superior to one at 300°C for improved film quality. Because there seems to be little improvement from 4 hours to 8 hours, it was decided that a 4 hour anneal at 500° C would be adequate for high quality oxide films.

Table C.2 Al_2O_3 Film Characteristics with Anneal

Anneal Conditions	Growth/ Cycle	Deviation (horizontal)	Deviation (vertical)	Dielectric Constant	Index of Refraction
None	3.41	0.6%	0.4%	8.3	1.52
300°C, 4 hrs	3.37	0.5%	0.3%	8.2	1.54
300°C, 8 hrs	3.33	0.4%	0.3%	8.5	1.55
500°C, 4 hrs	3.31	0.5%	0.3%	8.5	1.57
500°C, 8 hrs	3.30	0.5%	0.2%	8.5	1.59

Although the aluminum isopropoxide source method for growing Al_2O_3 films is somewhat unreliable and very process dependant, it does produce good quality films and is relatively quick (1/2 day for the total oxide procedure) and very inexpensive. For this

reason, it has become the method of choice for top oxide growth for the majority of devices created for this work.

C.1.2 Al_2O_3 growth from $Al(C_2H_5)$ and $Al(CH_3)_3$ with water

$Al(C_2H_5)_3$ and $Al(CH_3)_3$ were investigated as metallic sources in an attempt to possibly produce cleaner, higher quality oxide films than those produced using the aluminum isopropoxide method without introducing chlorine. Both materials are highly pyrophoric and as a result, must be handled very carefully. In order to prevent oxygen contamination, both materials were contained in lecture bottles and valved directly into the evacuated reactor chamber as gasses through ports 3 and 7, with the vapor flow controlled by an external leaker valve. The non-metallic source, H_2O, was kept as a liquid bath external to the reactor and kept at a constant 19°C and purged through lines 6 and 8.

Attempts at growth using the TEA source were largely unsuccessful. Substrate temperatures were varied between 150 and 350°C. TEA purge times were varied between 0.44 and 2.64 seconds. Because the TEA has a much lower vapor pressure, heating of the external lecture bottle and gas lines to 85°C was tried in order to purge more material successfully to the substrate. This was done by means of a heater coil wrapped around the lecture bottle and valves surrounded by an insulator material. Through it all, only very slight growth was ever observed. This growth did not seem to increase, however, with further pulsing. The TEA source was found to be extremely messy and difficult to work with. Frequent cleaning of the lines and valves was necessary to prevent clogs. This may actually be an indication of why thick films were never produced, as it is possible that the valves would be blocked after even very slight usage.

Greater success was found with the TMA source. The vapor pressure of TMA is much higher. Initial growth showed thick film growth through the center of the substrates with much less on the tops and bottoms. This appears indicative of too high a flow rate of the source material. For this reason the outer source valve was reduced and the source purge time was kept to only 0.22 seconds. This greatly improved uniformity in the vertical direction. Black film growth in the 'neck' of the reactor satellite indicated a CVD type reaction occurring as the reactants combined. To eliminate this long nitrogen purge times were necessary, 1.1 second pulse widths were found to be adequate. Water purge times were never varied, but kept constant at 0.22 seconds. Substrate temperatures were varied between 150 and 350°C. Growth appeared for those substrates processed at 200°C and higher, but uniformity for all substrates below 350°C was poor (>10% nonuniformity). Those processed at 350°C show exceptional uniformity as is evidenced in table C.1.

Like the aluminum isopropoxide situation, it appears that the growth rate of aluminum oxide from TMA is much greater on Si substrates than on standard glass, ITO, or phosphor materials. It may be possible that there is some phase matching occurring which improves the growth in this case, but no evidence of such currently exists. Also, much like the aluminum isopropoxide case, it appears that the growth rate per cycle tends to decrease sightly for longer run periods. Films grown for 1000 cycles produced films of 86 nanometers thick while films grown for 5000 cycles produced films of only 401 nanometers; resulting in a 7.5% decrease in total growth rate with increased cycles.

In general, the TMA process, much like the TEA attempted process, is very messy, requiring constant cleaning of the valves and inlet lines. Another difficult cleaning step comes in the reactor satellite. As has been mentioned, there is a small CVD reaction component which appears in the inlet neck to the substrate holders. Additionally, the rear of the substrate holder typically collects a light grey coating, believed to be a carbon based

by-product of the TMA. Both of these are very difficult and time consuming to clean adequately. In addition, the TMA process is far more time consuming than the isopropoxide situation. For all of these reasons the aluminum isopropoxide method appears to be the most efficient and economic means to produce high quality films for ACTFEL research on small phosphor test cases such as ours.

C.1.3 Attempted Al_2O_3 Growth from $Al(thd)_2$ and H_2O

The (thd) based molecules have been used successfully in ALE as precursor materials for a number of different compounds. It has been found that the metallic atom can often easily detach from its ligand and as a result often forms very clean films. For this reason the newly developed $Al(thd)_2$ material was tested as a possible Al metallic source with water as the standard oxide source. With substrate temperature varied between 200 and 450°C and $Al(thd)_2$ purge times varied between 0.44 and 0.88 seconds no film growth was ever detected. It has been concluded that $Al(thd)_2$ is not a suitable candidate for metallic precursor in ALE growth of Al_2O_3.

C.2 ALE Growth of Ta_2O_5

In an attempt to find a possible replacement of Al_2O_3 in ACTFEL work and perhaps an oxide suitable for other tasks, Ta_2O_5 was investigated. A metallic source of $Ta(OC_2H_5)_5$ (Tantalum Ethoxide) was used, again with water as the nonmetallic precursor. Film growth first appeared at substrate temperature of 350°C. Higher temps were not investigated in order to keep the growth in a usable temperature range for work with ACTFEL and other materials. ALE growth was performed on Si and SiO_2 substrates. With the

purge times of the Tantalum source and water held constant at 0.22 seconds and nitrogen purge times constrained to 0.44 - 0.66 seconds a number of films were grown.Table C.3 summarizes the growth results of Ta_2O_3 on Si and SiO_2 substrates for 2000 cycles for varying source temperatures.

Table C.3 Growth Rate of Ta_2O_5 from $Ta(OC_2H_5)_5$ at Varying Temperature

Temp (°C)	SiO_2 Substrates			Si Substrates		
	Growth Rate	deviation (hor)	deviation (vert)	Growth Rate	deviation (hor)	deviation (vert)
50	No Growth					
100	0.46	11%	9%	0.50	15%	9%
112	0.68	11%	7%	0.66	17%	10%
125	1.20	9%	1%	0.86	12%	12%
140	1.55	21%	20%	NA	NA	NA

The table shows some surprising results. The large change in growth rate with relatively small change in source temperature seems to indicate that this is not a true ALE process. This may be a partial result of the chosen substrate temperature. The large variation in growth rate from SiO_2 to Si substrates as well as the improved uniformity seen for the SiO_2 substrates may be indicative of some small amount of phase matching between the substrates and Ta_2O_5 film. Indeed, X-ray analysis of the film does appear to show some slight degree of crystallinity, with a small, fairly wide peak visible at around 25°. Currently this peak has yet to be identified for this oxide.

Appendix D

Matlab Program for Determining MQW Emission

The following program is based on the theory presented in Chapter 5 for the MQW model. It was used in conjunction with Matlab [XX] software to determine the empirical values for the unperturbed MQW model presented in Chapter 6. It is immediately followed by a similar program used to determine the values for the perturbed MQW model.

```
**************************************************************************

clear

c=2.998e8;
H=4.136e-15;
pi=3.1416;
hbar=1.05e-34;
e=-1.6e-19;
mo=9.11e-31;

EJ=1.602e-19;
JE=6.242e18;
A=1e-10;

Eg=2.70*EJ;
Voh=0.82*EJ;
Voe=0.88*EJ;
Mae=0.15*mo;
Mah=0.60*mo;
Mbe=0.50*mo;
Mbh=2.00*mo;

L=input('Enter the width (in Angstroms) of the well (0 turns off): ');
```

```
while (L~=0);

L=L*A;

Re=sqrt(Mae/Mbe);
Rh=sqrt(Mah/Mbh);

Ce=sqrt((Mae*Voe*L*L)/(8*hbar*hbar));
Ch=sqrt((Mah*Voh*L*L)/(8*hbar*hbar));

Ae=Ce*Ce;
Ah=Ch*Ch;

Nh=floor(1+sqrt((2*Mah*Voh*L*L)/(pi*pi*hbar*hbar)));
Nc=floor(1+sqrt((2*Mae*Voe*L*L)/(pi*pi*hbar*hbar)));

i=0.001

Tope=1000*Ce;

for n=1:1:Tope

    Xe(n)=i;

    Be(n)=(Re*sqrt(Ae-Xe(n)*Xe(n)));

    Odde(n)=Xe(n)*tan(Xe(n));
    Evene(n)=(Xe(n)/tan(Xe(n)));

    Te(n)=Odde(n)-Be(n);          %for determining odd levels
    Coe(n)=Evene(n)+Be(n);        %for determining even levels

    i=i+0.001;
end

i=0.001

Toph=1000*Ch;

for n=1:1:Toph

    Xh(n)=i;
    Bh(n)=(Rh*sqrt(Ah-Xh(n)*Xh(n)));
```

```
    Oddh(n)=Xh(n)*tan(Xh(n));
    Evenh(n)=(Xh(n)/tan(Xh(n)));

    Th(n)=Oddh(n)-Bh(n);          %for determining odd levels
    Coh(n)=Evenh(n)+Bh(n);        %for determining even levels

    i=i+0.001;
end

j=1

for m=1:1:(Tope-3)

    if abs(Te(m))>abs(Te(m+1))
        if abs(Te(m+2))>=abs(Te(m+1))
            Eoe(j)=(2*hbar*hbar*Xe(m+1)*Xe(m+1))/(Mae*L*L);
            j=j+1
        end
    end

    if abs(Coe(m))>abs(Coe(m+1))
        if abs(Coe(m+2))>=abs(Coe(m+1))
            Eoe(j)=(2*hbar*hbar*Xe(m+1)*Xe(m+1))/(Mae*L*L);
            j=j+1
        end
    end
end

k=1

for m=1:1:(Toph-3)

    if abs(Th(m))>abs(Th(m+1))
        if abs(Th(m+2))>=abs(Th(m+1))
            Eoh(k)=(2*hbar*hbar*Xh(m+1)*Xh(m+1))/(Mah*L*L);
            k=k+1
        end
    end

    if abs(Coh(m))>abs(Coh(m+1))
        if abs(Coh(m+2))>=abs(Coh(m+1))
            Eoh(k)=(2*hbar*hbar*Xh(m+1)*Xh(m+1))/(Mah*L*L);
            k=k+1
```

```
            end
        end
end

if j>k
        Short=k-1;
else
        Short=j-1;
end

for o=1:1:Short
        delEo(o)=JE*(Eoe(o)+Eoh(o)+Eg);
        lam(o)=(H*c/delEo(o))*1e9;
end

L=input('Enter the width (in Angstroms) of the well (0 turns off):  ');

end

**************************************************************************

clear

Cont=input('Enter 1 to continue, 0 to exit:  ');
while (Cont~=0);

clear

%constants
c=2.998e8;          %m/sec
H=4.136e-15;        %eVsec
pi=3.1416;       %const
hbar=1.05e-34;   %const
EJ=1.602e-19;    %conversion of eV to Joules
JE=6.242e18;     %conversion of Joules to eV
mo=9.11e-31;     %effective mass of rest electron
AM=1e-10;        %conversion of angstroms to meters
e=-1.6e-19;      %electron charge

%parameters
tATO=2600e-10;
tAl2O3=1200e-10;
epsilonATO=19;
```

```
epsilonAl2O3=8;

epsilonPhos=9.4; %This is for SrS

L=input('Enter the width (in Angstroms) of the well: ');
L=L*AM;

Lb=input('Enter the width (in Angstroms) of the host: ');
Lb=Lb*AM;

Numwell=input('Enter the number of wells: ');
tPhos=(L*Numwell)+(Lb*(Numwell+1));

Vapp=input('Enter the applied voltage (in V): ');

Nc=input('Enter the number of levels in the conduction band (0 turns off): ');

Mac=input('Enter the conduction band well mass (in units mo): ');
mac=Mac*mo;

Mbc=input('Enter the conduction band host mass (in units mo): ');
mbc=Mbc*mo;

Eoffc=input('Enter the conduction band off-set (in eV): ');
Eoffc=Eoffc*EJ;

Ec=e*(Vapp/epsilonPhos)/((tAl2O3/epsilonAl2O3)+(tPhos/epsilonPhos)+(tATO/e
psilonATO));

n=1;

%determine unperturbed E's and k's as well as normalization coefficients

for i=1:1:Nc,
'
   p=n/2;
   o=ceil(p);

   Xc(n)=input('Enter the X data for unperturbed case: ');
   Eoc(n)=(2*hbar*hbar*Xc(n)*Xc(n))/(mac*L*L);
   Enc(n)=Eoc(n);  %dummy for calculation purposes only
   Ejc(n)=Eoc(n);  %dummy for calculation purposes only
   Eec(n)=Eoc(n)*JE;  %Eo in eV
```

```
    k1c(n)=(2*Xc(n))/L;  %needed for calculation purposes
    kLc(n)=k1c(n)*L;  %for simplification purposes only
    k2c(n)=sqrt(((2*mbc*Eoffc)/(hbar*hbar)) - ((mbc/mac)*k1c(n)*k1c(n)));

    if p==o %evens

      Ac(n)=((L/2)-(1/(2*k1c(n)))*sin(kLc(n))+(1/k2c(n))*sin(kLc(n)/2)*sin(kLc
(n)/2)).^(-1/2);
      Bc(n)=Ac(n)*sin(kLc(n)/2);

    else   %odd by default

      Ac(n)=((L/2)+(1/(2*k1c(n)))*sin(kLc(n))+(1/k2c(n))*cos(kLc(n)/2)*cos(kLc
(n)/2)).^(-1/2);
      Bc(n)=Ac(n)*cos(kLc(n)/2);

    end

    n=n+1;

end

m=Nc;  %same as n essentially

%determine matrix values and calculate final perturbed energy

for j=Nc:-1:1, %go backwards to have best guess on first few levels

    q=m/2;  %to test if odd or even
    r=ceil(q);  %to test if odd or even

    l=1;
    for k=1:1:Nc,

      K1c(l)=k1c(l)+k1c(m);  %simplifies arithmatic
      K2c(l)=k2c(l)+k2c(m);  %simplifies arithmatic
      B2c(l)=-2*Bc(m)*Bc(l)*((K2c(l)*L/2)+1)/(K2c(l)*K2c(l));  %used in all ca
ses

      s=l/2;  %to test if odd or even
      t=ceil(s);  %to test if odd or even
      if l==m  %first term in sum
```

```
        Sc(l)=abs[Ec*B2c(l)];

    elseif t==s  %l even

        if r==q  %both even

          Hc(l)= Ec*B2c(l);
          Sc(l)=abs[Hc(l)*Hc(l)/(Eoc(m)-Eoc(l))];

        else   %l even, m odd

          Kmc(l)=k1c(l)-k1c(m);  %simplifies arithmatic
          A2c(l)=Ac(m)*Ac(l);
          Smc(l)=(1/(Kmc(l)*Kmc(l)))*sin(Kmc(l)*L/2);
          S1c(l)=(1/(K1c(l)*K1c(l)))*sin(K1c(l)*L/2);
          Cmc(l)=(-L/(2*Kmc(l)))*cos(Kmc(l)*L/2);
          C1c(l)=(-L/(2*K1c(l)))*cos(K1c(l)*L/2);
          Hc(l)=Ec*(B2c(l)+A2c(l)*(Smc(l)+S1c(l)+Cmc(l)+C1c(l)));
          Sc(l)=abs[Hc(l)*Hc(l)/(Eoc(m)-Eoc(l))];
          %term for odd/even

        end

    else %l odd by default

        if r==q  %l odd, m even

          Kmc(l)=k1c(m)-k1c(l);  %terms reversed from odd/even case for ev
en/odd case
          A2c(l)=Ac(m)*Ac(l);
          Smc(l)=(1/(Kmc(l)*Kmc(l)))*sin(Kmc(l)*L/2);

          S1c(l)=(1/(K1c(l)*K1c(l)))*sin(K1c(l)*L/2);
          Cmc(l)=(-L/(2*Kmc(l)))*cos(Kmc(l)*L/2);
          C1c(l)=(-L/(2*K1c(l)))*cos(K1c(l)*L/2);
          Hc(l)=Ec*(B2c(l)+A2c(l)*(Smc(l)+S1c(l)+Cmc(l)+C1c(l)));
          Sc(l)=abs[Hc(l)*Hc(l)/(Eoc(m)-Eoc(l))];

        else  %both odd

          Hc(l)=Ec*B2c(l);  %term when both odd
          Sc(l)=abs[Hc(l)*Hc(l)/(Eoc(m)-Eoc(l))];
```

```
        end

      end

      Enc(m)=Enc(m)-Sc(l);  %sum terms, including original Eo
      l=l+1;

    end

    Ejc(m)=Enc(m);
    Ejce(m)=Enc(m)*JE;  %perturbed in eV

    m=m-1;

end

Nv=input('Enter the number of energy levels in the valence band:  ');

Mav=input('Enter the valence band well mass (in units mo):  ');
mav=Mav*mo;

Mbv=input('Enter the valence band host mass (in units mo):  ');
mbv=Mbv*mo;

Eoffv=input('Enter the valence band off-set (in eV):  ');
Eoffv=Eoffv*EJ;

Ev=e*(Vapp/epsilonPhos)/((tAl2O3/epsilonAl2O3)+(tPhos/epsilonPhos)+(tATO/e
psilonATO));

n=1;

%determine unperturbed E's and k's as well as normalization coefficients

for i=1:1:Nv,

    p=n/2;
    o=ceil(p);

    Xv(n)=input('Enter the X data for unperturbed case:  ');
    Eov(n)=(2*hbar*hbar*Xv(n)*Xv(n))/(mav*L*L);
    Env(n)=Eov(n);  %dummy for calculation purposes only
    Ejv(n)=Eov(n);  %dummy for calculation purposes only
```

```
    Eev(n)=Eov(n)*JE;  %Eo in eV
    k1v(n)=(2*Xv(n))/L;  %needed for calculation purposes
    kLv(n)=k1v(n)*L;  %for simplification purposes only
    k2v(n)=sqrt(((2*mbv*Eoffv)/(hbar*hbar)) - ((mbv/mav)*k1v(n)*k1v(n)));

    if p==o %evens

      Av(n)=((L/2)-(1/(2*k1v(n)))*sin(kLv(n))+(1/k2v(n))*sin(kLv(n)/2)*sin(kLv
(n)/2)).^(-1/2);
      Bv(n)=Av(n)*sin(kLv(n)/2);

    else   %odd by default

      Av(n)=((L/2)+(1/(2*k1v(n)))*sin(kLv(n))+(1/k2v(n))*cos(kLv(n)/2)*cos(kLv
(n)/2)).^(-1/2);
      Bv(n)=Av(n)*cos(kLv(n)/2);

    else   %odd by default

      Av(n)=((L/2)+(1/(2*k1v(n)))*sin(kLv(n))+(1/k2v(n))*cos(kLv(n)/2)*cos(kLv
(n)/2)).^(-1/2);
      Bv(n)=Av(n)*cos(kLv(n)/2);

    end

    n=n+1;

end

mv=Nv;  %same as n essentially

%determine matrix values and calculate final perturbed energy

for j=Nv:-1:1, %go backwards to have best guess on first few levels

    qv=mv/2;  %to test if odd or even
    rv=ceil(qv);  %to test if odd or even

    lv=1;
    for k=1:1:Nv,

      K1v(lv)=k1v(lv)+k1v(mv);  %simplifies arithmatic
      K2v(lv)=k2v(lv)+k2v(mv);  %simplifies arithmatic
```

```
      B2v(lv)=-2*Bv(mv)*Bv(lv)*((K2v(lv)*L/2)+1)/(K2v(lv)*K2v(lv));
   q=m/2f p==o %evens

      Ac(n)=((L/2)-(1/(2*k1c(n)))*sin(kLc(n))+(1/k2c(n))*sin(kLc(n)/2)*sin(kLc
(n)/2)).^(-1/2);
      Bc(n)=Ac(n)*sin(kLc(n)/2);

   else   %odd by default

      Ac(n)=((L/2)+(1/(2*k1c(n)))*sin(kLc(n))+(1/k2c(n))*cos(kLc(n)/2)*cos(kLc
(n)/2)).^(-1/2);
      Bc(n)=Ac(n)*cos(kLc(n)/2);

   end

   n=n+1;

end

m=Nc;  %same as n essentially

%determine matrix values and calculate final perturbed energy

for j=Nc:-1:1, %go backwards to have best guess on first few levels

;  %to test if odd or even

      sv=lv/2;  %to test if odd or even
      tv=ceil(sv);  %to test if odd or even
      if lv==mv  %first term in sum

         Sv(lv)=abs[Ev*B2v(lv)];

      elseif tv==sv  %lv even

         if rv==qv  %both even

            Hv(lv)= Ev*B2v(lv);
            Sv(lv)=abs[Hv(lv)*Hv(lv)/(Eov(mv)-Eov(lv))];

         else   %lv even, mv odd

            Kmv(lv)=k1v(lv)-k1v(mv);  %simplifies arithmatic
```

```
        A2v(lv)=Av(mv)*Av(lv);
        Smv(lv)=(1/(Kmv(lv)*Kmv(lv)))*sin(Kmv(lv)*L/2);
        S1v(lv)=(1/(K1v(lv)*K1v(lv)))*sin(K1v(lv)*L/2);
        Cmv(lv)=(-L/(2*Kmv(lv)))*cos(Kmv(lv)*L/2);
        C1v(lv)=(-L/(2*K1v(lv)))*cos(K1v(lv)*L/2);
        Hv(lv)=Ev*(B2v(lv)+A2v(lv)*(Smv(lv)+S1v(lv)+Cmv(lv)+C1v(lv)));
        Sv(lv)=abs[Hv(lv)*Hv(lv)/(Eov(mv)-Eov(lv))];
        %term for odd/even

      end

    else %lv odd by default

      if rv==qv  %lv odd, mv even

        Kmv(lv)=k1v(mv)-k1v(lv);
        A2v(lv)=Av(mv)*Av(lv);
        Smv(lv)=(1/(Kmv(lv)*Kmv(lv)))*sin(Kmv(lv)*L/2);
        S1v(lv)=(1/(K1v(lv)*K1v(lv)))*sin(K1v(lv)*L/2);
        Cmv(lv)=(-L/(2*Kmv(lv)))*cos(Kmv(lv)*L/2);

        C1v(lv)=(-L/(2*K1v(lv)))*cos(K1v(lv)*L/2);
        Hv(lv)=Ev*(B2v(lv)+A2v(lv)*(Smv(lv)+S1v(lv)+Cmv(lv)+C1v(lv)));
        Sv(lv)=abs[Hv(lv)*Hv(lv)/(Eov(mv)-Eov(lv))];

      else  %both odd

        Hv(lv)=Ev*B2v(lv);  %term when both odd
        Sv(lv)=abs[Hv(lv)*Hv(lv)/(Eov(mv)-Eov(lv))];

      end

    end

    Env(mv)=Env(mv)-Sv(lv);  %sum terms, including original Eo
    lv=lv+1;

  end

  Ejv(mv)=Env(mv);
  Ejve(mv)=Env(mv)*JE;  %perturbed in eV
  mv=mv-1;
```

```
end

Eg=input('Enter the bandgap of the well material (in eV):  ');

a=1;

for u=1:1:Nc,

   Ediff(a)=Ejce(a)+Ejve(a)+Eg;
   lam(a)=H*c/Ediff(a);
   lam(a)=lam(a)*1e9;      %nm
   a=a+1;

end
%Output final results
Eec
Ejce
Eev
Ejve
lam

Cont=input('Enter 1 to continue, 0 to exit:  ');

end
```

REFERENCES

[1] L. Tannas, "Electroluminescent Displays," *Aerojet Technology*, vol. 1, n. 1, 4 (1983).

[2] C. King, "Electroluminescent Displays," *Journal of the Society for Information Display*, vol. 4, n. 1, 1 (1996).

[3] T. Inoguchi, S. Mito, "Phosphor Films," *Electroluminescence*, Spring Proc. Phys. edited by J. Pankove, 197 (1977).

[4] G. Destriau, *Journal of Chemical Physics*, vol. 33, 587 (1936).

[5] A. Vecht, N. Werring, R. Ellis, P. Smith, "Direct-Current Electroluminescent in Zinc Sulfide: State of the Art," *Proceedings of the IEEE,* vol. 61, n. 7, 902 (1973) .

[6] M. Takeda, Y. Kakihara, M. Yoshida, Y. Nakata, M. Kawaguchi, H. Kishishita, Y. Yamauchi, T. Inoguchi, S. Mito, "Inherent Memory Effects in ZnS:Mn Thin-Film EL Devices," *Journal of Japanese Society of Applied Physics*, vol. 44, supplement 1975, 103 (1974). (Conference on Solid State Devices, 6th, 1974, Tokyo)

[7] J. Haaranen, R. Tornquist, J. Koponen, T. Pitkanen, M. Surma-aho, B. Baro, C. Laakso, "A 9 Inch Diagonal, Compact, Multicolor TFEL Display," *SID 92 Digest*, 348 (1992).

[8] S. Tanaka, "Thin Film Electroluminescent Devices Using CaS and SrS," *Journal of Crystal Growth*, vol. 101, 958 (1990).

[9] C. King, "Electroluminescence: An Industry Perspective," *Journal of the Society for Information Display*, vol. 4, n. 3, 153 (1996).

[10] J. Li, Y. Lin, Y. Su, T. Wu, M. Yokoyama, "Growth and Characterization of the Active Layers in Electroluminescent Display Devices," *Progress in Crystal Growth and Characterization of Materials*, vol. 25, n. 1-2, 103 (1993).

[11] T. Minami, S. Takata, Y. Kuroi, T. Maeno, "New High-Luminance Thin-Film Electroluminescent Devices Using $ZnGa_2O_4$ Phosphor Emitting Layers," *Journal of the Society for Information Display*, vol. 4, n. 2, 53 (1996).

[12] T. Minami, Y. Kuroi, H. Yamada, S. Takata, "Color Coordinate Control in TFEL Devices Using MJulticomponent Oxide Phosphors," *Second International Conference on Science and Technology of Display Phosphors, San Diego*, 99 (1996).

[13] B. , J. Brightwell, S. Mason, B. Ray, I. Viney, "Impact of Phase Concentrations on Structure and Electroluminescence of ZnS:Cu," *Journal of Crystal Growth, Proceedings of the 5th International Conference on II-VI Compounds*, vol. 117, n. 1-4, 1008 (1992).

[14] P. Soininen, M. Leskela, L. Niinistu, E. Nykanen, E. Rauhala, "SrS:Mn as Green electroluminescent Material," *Proceedings of the Sixth International Workshop on Electroluminescence*, edited by V. Singh and J. McClure, 217 (1992).

[15] W. Barrow, R. Coovert, C. King, "Strontium Sulfide: The Host for a New High Efficiency Thin - Film Electroluminescent Blue Phosphor," *SID 84 Digest*, 249 (1984).

[16] S. Tanaka, H. Yoshiyama, J. Nishiura, S. Ohshio, H. Kobayashi, "Bright White - Light EL Devices with New Phosphor Thin Films Based on SrS," *Proceedings of the Society for Information Display*, vol. 29, 305 (1988).

[17] W. Kong, J. Fogarty, R. Solanki, R. Tuenge, "Violet Light Emitting SrS/SrCl:Eu Thin-Film Electroluminescent Devices," *Applied Physics Letters*, vol. 67, n. 1, 419 (1995).

[18] W. Barrow, R. Coovert, E. Dickey, C. King, C. Laakso, S Sun, R. Tuenge, R. Wentross, J. Kane, "A New Class of Blue TFEL Phosphors with Applications to VGA Full-Color Display," *SID 93 Digest*, 761 (1993).

[19] Y. Abe, K. Onisawa, K. Tamura, T. Nakayama, M. Hanazono, Y. Ono, "White Light Emitting Thin Film Electroluminescent Cells with SrS:Pr,Ce Active Layer and Their Application to Multicolor Electroluminescent Devices," *Japanese Journal of Applied Physics, Part 1: Regular Papers & Short Notes*, vol. 28, n. 8, 1373 (1989).

[20] K. Ohmi, S. Tanaka, Y. Yamano, "White Light Emitting Electroluminescent Devices with $(SrS:Ce/ZnS:Mn)_n$ Multilayer Thin Films," *Japan Display*, 725 (1992).

[21] A. Matsuno, T. Nire, F. Wada, K. Fuchiwaki, "A 4.4 Inch Diagonal RGB Multicolor TFEL Display," *Japan Display*, 717 (1992).

[22] R. Mauch, K. Velthaus, H. Schock, "Novel ZnS/SrS:Ce Multilayer Phosphors for Efficient ACTFEL Devices," *SID 92 Digest*, 178 (1992).

[23] T. Suntola, "Performance of Atomic Layer Epitaxy Devices," *SID 81 Digest*, 20, (1981).

[24] T. Suntola, J. Antson, "Method for Producing Compound Thin Films." US Patent No. 4,058,430 (1977).

[25] W. Kong, S. Ahmed, J. Ferguson, R. Solanki, "Violet Light Emitting SrS/SrCl:Eu Thin-Film Electroluminescent Devices," *Applied Physics Letters*, vol. 67, n. 1, 7, (1995).

[26] T. Suntola, "Atomic Layer Epitaxy," *Conference on Solid State Devices and Materials 16th, Kobe, Extended Abstracts,* 647 (1984).

[27] W. Kong, *Growth and Characterization of Thin Film Electroluminescent Devices Fabricated Using Atomic Layer Epitaxy*, Thesis (PhD), Oregon Graduate Institute of Science and Technology (1996).

[28] M. Godlewski, M. Leskela, "Excitation and Recombination Processes During Electroluminescence of Rare Earth-Activated Materials," *Critical Reviews in Solid State & Materials Sciences*, vol. 19, n. 4, 199 (1994).

[29] E. Mager, US Patent 2,566,349, issued September 4, (1951).

[30] W. Piper, US Patent 2,698,915, issued Jan. 4, (1963).

[31] M. Kilburn, F. Hoffman, R. Hayes, *IEEE Papers*, 2441M, 136 (1957).

[32] Y. Chen, D. Krupka, "Limitation Imposed by Field Clamping on the Efficiency of High-Field AC Electroluminescence in Thin Films," *Journal of Applied Physics*, vol. 43, n. 1, 4089 (1972).

[33] W. Ruehle, V. Marrello, A. Onton, "AC Thin Film Electroluminescence, Filamentary Emission and Its Memory Effect," *Journal of Luminescence (Proceedings of the International Conference on Luminescence)*, vol. 18-19, n. 2, 729 (1978).

[34] G. Mueller, *Solid State Luminescence Theory, Materials and Devices*, edited by A. Kitai, Chapman & Hall, NY, 133 (1984).

[35] G. Mueller, R. Mach, "On the Mechanism of Electron Impact Excited Luminescence Devices," *Physica Status Solidi (A), Applied Research*, vol. 77, n. 2, k179 (1983).

[36] J. Davidson, J. Wager, R. Khormaei, C. King, R. Williams, "Electrical Characterization and Modeling of Alternating-Current Thin-Film Electroluminescent Devices," *IEEE Transactions on Electron Devices*, vol. 39, n. 5, 1122 (1992).

[37] H. Fitting, A. Von Czarnowski, G. Mueller, "Ballistic Transport in Alkaline Earth Sulfides," *Journal of Crystal Growth, (Proceedings of the 4th International Conference on II-VI Compounds)*, vol. 101, 876 (1990).

[38] D. Hommel, W. Busse, H. Gumlich, D. Suisky, J. Roeseler, "Energy Transfer Pro-

cesses in Rare Earth Doped ZnS Under Non-Linear Excitation," *Journal of Crystal Growth, (Proceedings of the 5th International Conference on II-VI Compounds)*, vol. 117, n. 1-4, 721 (1992).

[39] P. Keir, W. Ang, J. Wager, "Modeling Space Charge in ACTFEL Devices Using A Single-Sheet-Charge Model," *SID 95 Digest*, 476 (1995).

[40] R. Mach, G. Mueller, "Ballistic Transport and Electroluminescence in IIb-VI and IIA-VI Compounds," *Journal of Crystal Growth, (Proceedings of the 4th International Conference on II-VI Compounds)*, vol. 101, 967 (1990).

[41] R. Tornquist, M. Ylilammi, "The Decay and Saturation of the Emission in ac EL ZnS:Mn Thin Films," *Journal of Luminescence*, vol. 27, 285 (1982).

[42] P. Soininen, L. Ninisto, E. Nykanen, "The Effect of Gaseous $SiCl_4$ on the ALE Growth of CaS, SrS and SrS:Ce," *Applied Surface Science*, vol. 75, 99 (1994).

[43] D. Poelman, R. Van Meerhagh, W. Laflere, F. Carlson, "The Influence of Se Co-evaporation on the Electroluminescent Properties of SrS:Ce Thin Films," *Journal of Luminescence*, vol. 52, 259 (1992).

[44] P. Ghosh, B. Ray, "Luminescence in Alkaline Earth Sulfides," *Progress in Crystal Growth and Characterization of Materials*, vol. 25, n. 1-2, 1 (1993).

[45] G. Jacobs, *Comparative Color Vision*, Academic Press, NY 1981.

[46] R. Mauch, K. Velthaus, B. Huttl, U. Troppenz, R. Herrmann, "Improved SrS:Ce,Cl TFEL Devices by ZnS Co-Evaporation," *SID 95 Digest*, 729 (1995).

[47] H. Kobayashi, "SrS-ZnS Electroluminescence Materials," *Journal of Crystal Growth*, vol. 138, 1010 (1994).

[48] K. Velthaus, R. Mauch, H. Schock, S. Tanaka, K. Yamada, K. Ohmi, H. Kobayashi, "Efficient Electroluminescent Devices Based on ZnS/SrS:Ce Multilayered Phosphors", *Proceedings of the Sixth International Workshop on Electroluminescence*, edited by V. Singh and J. McClure, 187 (1992).

[49] T. Fukushida, S. Shionoya, "Luminescence of Bound Excitons in Tellurium-Doped Zinc Sulfide Crystals," *Japanese Journal of Applied Physics*, vol. 12, n. 4, 549 (1973).

[50] W. Heimbrodt, O. Goede, "Energy Transfer Processes between Te_n Centres in ZnS:Te and CdS:Te," *Physica Status Solidi (B), Basic Research,* vol. 135, 795 (1986).

[51] O. Goede, W. Heimbrodt, T. Lau, G. Matzkeit, B. Selle, "Optical and RBS Studies of ZnS:Te Thin Films," *Physica Status Solidi (A), Applied Research*, vol. 94, n. 1, 259 (1986).

[52] R. Mach, G. Mueller, "Physical Concepts of High-Field, Thin-Film Electroluminescence Devices," *Physica Status Soldi (A), Applied Research*, vol. 69, n. 1, 11 (1982).

[53] Y. Ono, *Electroluminescent Displays*, World Scientific, Singapore, 1995, Chap. 6.

[54] R. Engelmann, J. Ferguson, R. Solanki, "Quantum Well Activated Phosphors - A New Concept for Electroluminescent Displays," *Applied Physics Letters*, vol. 70, 411 (1997).

[55] D. Smith, "Modeling AC Thin-Film Electroluminescent Devices," *Journal of Luminescence*, vol. 23, n. 1-2, 209 (1981).

[56] C. Weisbuch, B. Vintner, *Quantum Semiconductor Structures*, Academic, San Diego, p. 13 (1996).

[57] H. Margenau, G. Murphy, *The Mathematics of Physics and Chemistry*, D. Van Nostrand Company, Inc, (1976).

[58] R. Eisberg, R. Resnick, *Quantum Physics of Atoms, Molecules, Solids, Nucleii, and Particles*, Second Ed., John Wiley & Sons, NY (1985).

[59] G. Lengyel, K. Jelley, R. Engelmann, "A Semi-Empirical Model for Electroabsorption in GaAs/AlGaAs Multiple Quantum Well Modulator Structures," *IEEE Journal of Quantum Electronics*, vol. 26, no. 2, 296 (1990).

[60] D. Endisch, K. Barth, J. Lau, G. Peterson, A. Kaloyeros, D. Tuenge, C. King, "MOCVD SrS:Ce for Applications in Electroluminescent Devices," *Materials Research Society Symposium Proceedings*, vol. 471, Flat Panel Display Materials, Proceedings of the 1997 MRS Spring Meeting, 269, (1997).

[61] O. Madelung, *Semiconductors: Other Than Group IV Elements and III-V Compounds*, Springer-Verlag, Berlin (1992).

[62] H. Fujiyasu, K. Hikida, T. Kiichi, K. Ishino, A. Ishida, T. Hiyoshi, I. Fujisawa, "LED Electroluminescent Devices with High Brightness Fabricated by Highly Strained layer Superlattices of Mn-Doped II-VI Compounds", *Proceedings of the International Symposium on Inorganic and Organic Electroluminescence, Technical Digest, Hamamatsu, Japan,* 64 (1994).

[63] T. Matsumoto, T. Iwashita, K. Sasamoto, T. Kato, "Atomic Layer Epitaxy of CdSe/ ZnSe Short Period Superlattices," *Journal of Crystal Growth*, vol. 138, 63 (1994).

[64] Z. Peng, J. Li, W. Yao, L. He, X. Cheng, S. Yuan, "Atomic Layer Epitaxy of ZnSe-$(CdSe)_m(ZnSe)_n$ Short-Period Superlattice Multiple Quantum Wells," *Japanese Journal of Applied Physics*, vol. 31, Pt. 2, n. 11B, L1583 (1992).

[65] N. Samarth, H. Luo, J. Furdyna, S. Qadri, Y. Lee, A. Ramdas, N. Otsuka, "Growth icsof Cubic (Zinc Blende) CdSe by Molecular Beam Epitaxy," *Applied Physics Letters*, vol. 54, n. 26, 2680 (1989).

[66] A. Hasagawa, A. Yanase, "Electronic Structure of Sr Monochalcogenides," *Journal of Physics C: Solid State Physics*, vol. 13, 1995 (1985).

[67] J. McKelvey, *Solid State and Semiconductor Physics*, Robert E. Krieger Publishing Company, 219 (1986).

[68] S. Sun, M. Bowen, J. Daniel, S. Moehnke, A. Hodges, R. Tuenge, S. Pearson, J. Phillips, L. Simonsen, C. King, "White Monochrome TFEL Displays with SrS:Cu,Ag/ ZnS:Mn Stack Phosphor," *SID 99 Digest*, 1146 (1999).

[69] S. Sun, E. Dickey, J. Kane, N. Yocom, "A Bright and Efficient New Blue TFEL Phosphor," *Proceedings of the 17th International Display Research Conference*, Toronto, Canada, 301 (1997).

[70] S. Yun, Y. Kim, J. Khang, S. Park, K. Cho, D. Ma, "High Luminescence Blue-Emitting CaS:Pb EL Devices Fabricated by ALE," *SID 99 Digest*, 1142 (1999).

[71] R. Mauch, K. Velthaus, G. Bilger, H. Schock, "High Efficiency SrS,SrSe:$CeCl_3$ Based Thin Film Electroluminescent Devices," *Journal of Crystal Growth*, 117, 964 (1992).

[72] S. Okimoto, F. Nakazawa, "Transient Emission Mechanisms in Thin-Film Electroluminescent Devices with Rare-Earth-Ion-Activated SrS Phosphor Layers," *Japanese Journal of Applied Physics*, vol. 34, 521 (1995).

[73] V. Balek, J. Fusek, O. Kriz, M. Leskela, L. Niinisto, E. Nykanen, J. Rautanen, P. Soininen, "Emanation Thermal Analysis in the Characterization of Zinc Sulfide Thin Films Prepared from Different Precursors," *Journal of Materials Research*, vol. 9, n. 1, 119 (1994).

[74] K. Hirabayashi, O. Kigure, "AC-Thin Film ZnS:Mn Electroluminescent Device Prepared by Metal Organic Chemical Vapor Deposition," *Japanese Journal of Applied*

Physics, vol. 24, n. 11, 1484 (1985).

[75] R. Tornquist, M. Ylilammi, "Decay and Saturation of the Emission in AC EL ZnS:Mn Thin Films," *Journal of Luminescence*, vol. 27, n. 3, 285 (1982).

[76] M. Leskela, L. Niinisto, E. Nykanen, P. Soinen, M. Tiitta, "Aluminium Oxide Thin Film Deposition from Aluminium Chloride and 2-Methyl-2-Propanol Using the Atomic Layer Epitaxy Process," *Acta Polytechnica Scandinavica, Chemical Technology and Metallurgy Series*, n. 95, *(First International Symposium on Atomic Layer Epitaxy)*, 193 (1990).

[77] S. Singh, K. Anand, "Conduction and Charge Storage in a Double-Dielectric MAOS Structure for Memory Applications," *Thin Solid Films*, vol. 48, 353 (1978).

[78] L. Hiltunen, H. Kattelus, M. Leskela, M. Maekela, L. Niinistoe, E. Nykaenen, P. Soininen, M. tiita, "Growth and Characterization of Aluminium Oxide Thin Films Deposited from Various Source Materials by Atomic Layer Epitaxy and Chemical Vapor Deposition Processes," *Materials Chemistry and Physics*, vol. 28, n. 4, 379 (1991).

John G. Ferguson was born to Duncan and Gail Ferguson of Canton, MA on 12/31/68 in Quincy, MA. He received his bachelor's degree in physics from McGill University, Montreal, PQ in 6/91. He received a master's degree in applied physics from the University of Massachusetts, Dorchester, MA in 6/93. Publications include:

W. Kong, S. Ahmed, J. Ferguson, and R. Solanki, "Violet light emitting SrS/SrCl:Eu thin-film electroluminescent devices", Appl. Phys. Lett., 67, 7 (1995).

R. Engelmann, J. Ferguson & R. Solanki, "Quantum-well Activated Phosphors: A New Concept for Electroluminescent Displays", Appl. Phys. Lett, 70, 411 (1997).

John is currently employed by Mentor Graphics Corporation of Wilsonville, OR as a technical marketing engineer.